UNIVERSITY OF TWENTE.

**Faculty of Engineering Technology,
Chair of Engineering Fluid Dynamics**

3D simulation of a wind turbine rotor in axial inflow conditions

Daniëlle Maat
Master Thesis
August 2023

Document number:
EFD-430
Exam Committee:
prof. dr. ir. C.H. Venner (chair)
dr. H. Ozdemir (internal member)
dr. I. Ostanin (external member)
dr. A. Koodly Ravishankara (supervisor TNO)

Faculty of Engineering Technology,
Chair of Engineering Fluid Dynamics
University of Twente
P.O. Box 217
7500 AE Enschede
The Netherlands

Abstract

During the last two decades, there has been a significant increase in global installed wind energy capacity. The costs of wind energy are reducing while wind turbines are growing in size. Future developments in the wind energy industry may follow from a better understanding of aerodynamics. Wind turbine aerodynamics and rotor modelling are associated with several uncertainties. Computational Fluid Dynamics (CFD) is a tool to provide a more accurate analysis and reduce uncertainties. A pressure-based solver was recently implemented in SU2. In this study, the ability of the pressure-based solver to simulate the flow over a wind turbine rotor is investigated. The simulation results are compared against experimental data and numerical results from other studies.

Two-dimensional (2D) flow problems are simulated to validate the pressure-based solver's ability to predict external aerodynamic phenomena. The turbulent flow over a flat plate, the turbulent flow over a backward facing step and the turbulent flow over the NACA0012 airfoil are considered. Based on comparison against analytical results, experimental data and numerical results from other works, it is found that the pressure-based solver captures the turbulent boundary layer, flow reversal and reattachment after separation from a fixed point and the flow over an airfoil.

The MEXICO and DanAero rotor are modelled in axial inflow conditions. The flow over the MEXICO rotor operating under design conditions was simulated. The DanAero rotor is simulated for operation under a pitch angle of 0.17° and 3.0°. The predicted blade pressures and normal forces are compared against experimental data and numerical results from other studies as well as the velocity around the MEXICO rotor and in its near-wake. Experimental data of the MEXICO rotor was made available and based on wind tunnel measurements and experimental data of the DanAero rotor was based on field measurements. Numerical issues are observed while modelling the MEXICO rotor in the turbulent wake state and the DanAero rotor on a rectangular mesh.

It is found that the pressure-based solver predicts the pressure on the blades, normal and tangential forces and the velocity around the rotor and in the near-wake in good agreement with other numerical methods. Observed differences between the experimental data and numerical results obtained using the pressure-based solver are generally similar to differences between the experimental data and other studies numerical results. Pressure levels are somewhat overpredicted on the suction side. The pressure-based solver predicts unphysical wiggles in the skin friction coefficient. In agreement with literature and based on the study of the MEXICO rotor, the velocity field in the vicinity of the tip and root vortices is found difficult to predict.

Preface

This master thesis is the result of my graduation assignment, which is the final part of the master program Mechanical Engineering at the University of Twente (UT). In the period from September 2022 to July 2023, the research activity was conducted at TNO.

The thesis contributes to a part of Task 47 of International Energy Agency (IEA) Wind Technology Collaboration Programme (TCP). The IEA Wind TCP is an international cooperation of multiple countries and sponsor members that share information and research activities to further develop the wind energy industry. In Task 47 measurements on a full-size MW wind turbine (the Danish DanAero experiments) are compared with numerical results.

I would like to thank Akshay Koodly Ravishankara as my daily supervisor from TNO and Huseyin Ozdemir as my supervisor from the UT. I am thankful for the opportunity to conduct the assignment at TNO.

I've found that the graduation assignment was a mentally challenging exercise. I would like to thank my family and friends for their patience and for their continued support and trust. I would not have been able to finish this work without the infinite support of Kevin.

I hope you enjoy the reading!

Daniëlle Maat

Contents

Chapter 1

Introduction

Wind energy is a renewable energy source which has been developing fast over the last two decades. The development is driven by the need to reduce the fossil fuel energy consumption and meet climate goals. From 2000 to the present, there has been a significant increase in the global installed wind energy capacity, both onshore and offshore, as shown in Figure 1.1. The International Energy Agency (IEA) expects that the onshore wind energy capacity increases to 1350 GW and the offshore wind energy capacity to 190 GW by 2027 [1]. Taking advantage of the stronger winds at sea, especially offshore wind is expected to grow rapidly in the coming years.

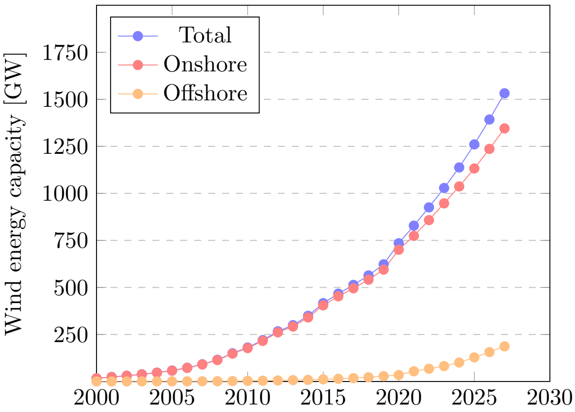

Figure 1.1: Installed onshore and offshore wind energy capacity [1]

In the beginning of the 1980s, early modern wind turbines with a rated power of 20-50 kW were developed. Nowadays, wind turbines with a capacity ranging between 3 MW and 5 MW are being installed onshore and between 8 MW and 12 MW offshore. Figure 1.2 gives an overview of the increase in wind turbine size from the 1980s to the 2020s as well as an outlook into the near future. The main development in the design of wind turbines that led to an increased capacity was an increase in wind turbine size. Throughout the years, the size of wind turbines increased from a rotor diameter of 15 m up to today's largest wind turbine with a rotor diameter of more than 200 m [2]. Along with an increase in rotor diameter, the hub height increased. The larger the rotor diameter, the larger the area from which energy can be extracted. Simultaneously, the wind reaches higher velocities at greater heights. Thus, the larger the rotor diameter and the higher the hub, the more energy is available for extraction from the wind. Next to having an increased capacity, a larger wind turbine is associated with a lower relative contribution of investment costs. The costs of wind energy reduce as wind turbines grow in size.

Increasing the size of a wind turbine further and further is a challenging task. For onshore wind turbines, this is mainly related to noise whereas for offshore wind turbines, structural limits play an important role. Additionally, the uncertainty of the aerodynamic design has increased as modern wind turbines grow in size. Uncertainties in wind turbine aerodynamics are related to off-design conditions as well as to more pronounced aero-elastic behaviour in modern wind turbines. A better understanding of wind turbine aerodynamics is a promising opportunity to further optimisations of wind turbine design.

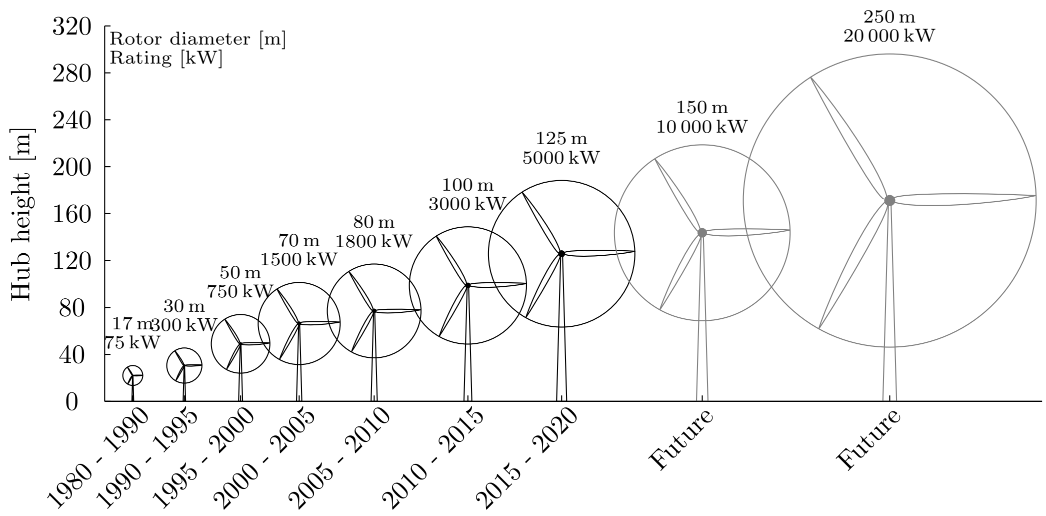

Figure 1.2: Development of hub height, rotor diameter and rating of wind turbines [3]

1.1 Wind turbine aerodynamics

A wind turbine extracts kinetic energy from the wind and produces electricity. The extraction of kinetic energy from the wind and the power production of a wind turbine are based on the aerodynamic performance of the rotor blades and driven by the aerodynamic force called lift. The cross-sections of the rotor blades have the shape of an airfoil. Due to the cross-sectional shape of the rotor blades and the interaction with the wind, a suction force away from the airfoil is generated on its upper side and a pressure force towards the airfoil is generated on its lower side. The combination of these forces in the direction normal to the incoming wind is called lift. It causes the blade to move towards the low-pressure side, leads to a torque on the shaft of the wind turbine and produces mechanical power. Finally, a generator converts the mechanical power into electricity.

The interaction of the rotor and the wind affects the flow field. The flow expands around the rotor and the extraction of energy slows down the wind in the wake. The wake rotates in opposite direction of the rotor as a reaction to torque. Just downstream of the rotor, in the so-called near-wake, the flow field is dependent on the rotor characteristics. Tip and root vortices are created due to pressure differences at the upper and lower surface of the blade. They are convected downstream and far downstream, the wake recovers to the original flow field.

Wind turbine aerodynamics is associated with several complexities. Wind turbines are located in the outside environment in which the wind is unsteady and turbulent. As a result, a wind turbine can be subject to a wide range of different and rapidly changing inflow conditions. Complicated flow fields mainly occur when wind turbines operate in non-uniform inflow conditions such as sheared or yawed flow but can also occur in axial inflow conditions. The inflow is further complicated if a wind turbine is installed in the wake of another turbine. Next to complicated inflow conditions, unsteady effects such as stall and transition of the boundary layer make the flow field hard to solve. Most common flow conditions and rotor configurations can be accurately modelled and designed for. Complexities and uncertainties in the flow field are mostly introduced by off-design conditions.

1.2 Rotor modelling

The design of a wind turbine is greatly influenced by the accuracy with which an aerodynamic model of the rotor can be made. Several strategies for rotor modelling have been developed throughout the years. The different numerical approaches differ in the accuracy with which they predict the performance, the physics they reveal, the operating conditions they can deal with and the computational costs. The most general categories are shortly discussed below. A more elaborate overview on wind turbine aerodynamics and aeroelasticity is provided by Hansen et al. [4], on wind turbine aerodynamics by Snel [5] and Sørensen [6] and on Computational Fluid Dynamics (CFD) in wind energy by Sumner [7] and Daniele [8].

Blade Element Momentum theory

The Blade Element Momentum (BEM) theory, proposed by Glauert [9], is a popular method and often used in the initial design stages of a wind turbine. BEM combines 1D momentum theory and blade element theory to predict the performance of a rotor. In its basic form, BEM models the rotor as an actuator disc subjected to a steady and axisymmetric inflow. The simplicity of BEM follows from its assumptions and introduces several limitations. Several engineering models and empirical relations have been developed to improve and extend the capabilities of BEM [10]. Accurate results are obtained for most common flow conditions and rotor configurations if reliable 2D lift and drag coefficients are provided.

Vortex methods

Vortex methods model the rotor blades and system of vortices by a lifting line or lifting surface. Bound vortices are located along the span. Trailing vortices are formed due to variation in bound vorticity at the blade and convected downwards. The strength of the vortices follows from local inflow conditions and 2D airfoil data. Finally, the flow field can be resolved using the Biot-Savart law. Vortex models solve for potential flows, which are irrotational and inviscid. While vortex models provide more information on the flow field than BEM, vortex models are still dependent on 2D airfoil data [6].

Vortex panel methods can be used to solve for the velocity field of inviscid lifting flows. A vortex sheet with varying strength is wrapped over the body such that it becomes a streamline of the flow. The vortex sheet is approximated by a number of panels. Each panel has a different vortex panel strength [11]. Vortex panel methods yield better accuracy than lifting lines or lifting surfaces as they have a more advanced representation of the geometry. In order to make vortex models more applicable to viscous flows, the inviscid vortex models need a ‘coupling’ with viscous methods. An example of the application of inviscid-viscous ‘coupling’ is the aerodynamic design tool XFOIL [12] which combines modelling the inviscid flow using a vortex panel method and the viscous flow using boundary layer equations. For better applicability in the wind energy industry, XFOIL was extended to RFOIL [13].

CFD

CFD predicts the fluid flow by numerically solving the conservation laws of mass, momentum and energy. With increasing availability of computational resources, CFD has become a tool for the evaluation of the viscous, incompressible and turbulent flow around a wind turbine rotor. Although CFD is too expensive to be commonly applied in the design process due to its high computational costs, it provides much more information about the physics of the flow than BEM and vortex models. The first simulations were performed in the late 1990s by Duque et al. [14], Sørensen and Hansen [15] and Varela and Bercebal [16]. Since then, several CFD simulations in application to wind turbine rotors have been performed [7, 6, 8]. CFD simulations have contributed to improvements of engineering models as well as obtaining a better understanding of aerodynamics. Next to being applied for rotor modelling, applications of CFD are also in 2D airfoil aerodynamics and the modelling of wind farms. As an alternative to 3D full rotor studies, simplified approaches in which the wind turbine is modelled by, for example, an actuator disc may be used.

The flow around a wind turbine rotor is often modelled by incompressible flow equations. Incompressible flow equations are challenging to solve [17, 18]. In contrast to the set of compressible flow equations, the incompressible flow equations have no direct equation for the pressure. This can be overcome using either density-based or pressure-based methods. Density-based methods alter the continuity equation such that it is no longer a restriction of the velocity field. It is altered to provide information on another variable and to allow for the application compressible flow solvers. However, solving the altered incompressible flow equations using a compressible flow solver requires to deal with two very distinct propagation speeds. The propagation speed of the fluid flow is much smaller than the speed of sound. This can be overcome using pre-conditioning. Pressure-based methods combine the continuity equation and momentum equations to recover a Poisson equation for the pressure. Using an iterative procedure, the momentum equations are solved for the velocities and the Poisson equation for the pressure. Stanford University Unstructured (SU2) [19], an open-source software package for computational analysis and design optimisation, has a density- and pressure-based solver implemented [20, 21]. The pressure-based solver was recently implemented in SU2 to enhance the applicability of SU2 in the wind energy industry.

Validation of CFD methods

To work with CFD methods for various applications, it is important that the CFD methods are validated. Validation studies consider the ability of a numerical method to predict the physics of a flow. This is often done based on experimental data. The data from three main measurement campaigns, i) Phase VI of the NREL Unsteady Aerodynamic Experiment program [22]; ii) the MEXICO and New MEXICO project [23, 24]; and iii) the DanAero experiment [25, 26]; are used by several authors to validate their numerical methods and improve rotor modelling. The NREL Phase VI and MEXICO experiments were conducted in a wind tunnel where the inflow and operation conditions could be controlled. A 10 m-diameter wind turbine rotor was tested in the NASA Ames wind tunnel in the NREL Phase VI experiment and a 4.5 m-diameter rotor was tested in the Large Low speed Facility (LLF) of the German Dutch Wind tunnel (DNW) in the MEXICO projects. Both experiments measured blade pressures at several radial sections for a wide range of conditions. Additionally, PIV measurements were performed to capture the velocity around the rotor and in the near-wake in the MEXICO experiments. The DanAero experiments are a series a field measurements conducted at full-size modern wind turbines. Inflow conditions as well as pressures were measured at several blade sections. Furthermore, a series of wind tunnel measurements on airfoil sections of the corresponding blades were carried out. The MEXICO projects are very suitable for validation of CFD methods as they provide both blade pressure and PIV measurement data. The DanAero project generated a database consisting of data related to more real and more complex flows in the unsteady and turbulent atmospheric environment. The databases generated during the experimental projects are widely studied and considered in so-called IEA Tasks. Among other things, the ability of different numerical methods to be applied in aerodynamic rotor modelling are investigated in IEA Tasks. Multiple participants from different countries compared their CFD method against experimental data for validation [27, 28, 29, 30, 31, 32]. The pressure-based solver that was recently implemented in SU2 is not widely validated yet.

1.3 Motivation and goal

The goal of this MSc thesis is to study the ability of the pressure-based solver as implemented in SU2 [19, 21] to simulate the flow over a wind turbine rotor in axial inflow conditions. In this work, the pressure-based solver is applied to the MEXICO rotor operating in its design conditions and the DanAero rotor operating under two different pitch angles. Through the use of experimental and numerical data from other studies, the ability of the pressure-based solver to predict the loads on the wind turbine rotor blades and to predict the velocity field around the rotor and in the near-wake is investigated. Additionally, numerical issues may be identified to obtain a better understanding of what part of the pressure-based solver's implementation requires further study. The results of the simulation of the DanAero rotor serve as a contribution to IEA Task 47. Thereby, the results from this study also contribute to a large comparison exercise.

1.4 Outline

The structure of this thesis is given here.

- Chapter 2 - *Numerical background*
  The numerical background in relation to modelling incompressible and turbulent flow is explained. The main principles necessary to understand the general ideas of the implementation of the pressure-based solver in SU2 are explained.

- Chapter 3 - *Validation for 2D flow problems*
  The pressure-based solver is validated for 2D external aerodynamic phenomena. The turbulent flow over a flat plate, turbulent flow over a backward facing step and turbulent flow over the NACA0012 airfoil are considered.

- Chapter 4 - *Rotor simulation*
  The pressure-based solver is applied to the MEXICO rotor and DanAero rotor in axial inflow conditions. Its ability to predict the loads on the blade of a wind turbine rotor as well as its ability to predict the flow field in the near-wake are studied. A study on the turbulent wake state is included.

- Chapter 5 - *Conclusions*
  This chapter presents the conclusions of the thesis.
- Chapter 6 - *Recommendations & future work*
  Recommendations and suggestions for future work are given in this chapter.

Chapter 2

Numerical background

Wind turbines are located in the outside environment and they experience atmospheric wind conditions. The wind around a wind turbine rotor is generally assumed incompressible and turbulent. Therefore, the reader is firstly introduced to the modelling of turbulent, incompressible flow. Subsequently, the general principles of the pressure-based solver are explained. Several configuration options such as the boundary conditions and rotating reference frame are discussed. For a more comprehensive overview on the implementation, the interested reader is referred to [21, 19].

2.1 Incompressible flow

Wind turbines are mostly considered to operate in incompressible and turbulent flow although compressibility effects may occur locally. Incompressible flows are flows in which a change in pressure does not result in a change in density. Since there are no other sources that cause a density change, the density in the flow around a wind turbine is assumed constant. Incompressible flows in which viscous effects are important are governed by the incompressible Navier-Stokes equations. The incompressible Navier-Stokes equations for a flow with constant density and constant viscosity are given by:

$$\frac{\partial(\rho u_i)}{\partial x_i} = 0, \tag{2.1}$$

$$\frac{\partial(\rho u_i)}{\partial t} + \frac{\partial(\rho u_i u_j)}{\partial x_j} = -\frac{\partial p}{\partial x_i} + \mu\left(\frac{\partial^2 u_i}{\partial x_j \partial x_j}\right). \tag{2.2}$$

Here, $u_i = (u, v, w)^T$ is the flow velocity, $x_i = (x, y, z)^T$ is the spatial coordinate, p is the pressure, ρ is the density and μ is the dynamic viscosity. The Navier-Stokes equations are written using the Einstein summation convention, i.e. repeated indices represent a summation over the repeated index. The incompressible Navier-Stokes equations are non-dimensionalized using a characteristic velocity U and a characteristic length L. The non-dimensional variables are defined by:

$$u_i^* = \frac{u_i}{U}, \qquad x_i^* = \frac{x_i}{L}, \qquad t^* = \frac{t}{L/U}, \qquad p^* = \frac{p}{\rho U^2}, \tag{2.3}$$

in which the asterisk * indicates non-dimensionality. Substitution of the non-dimensional variables in equations (2.1) and (2.2) gives the non-dimensional incompressible Navier-Stokes equations:

$$\frac{\partial u_i^*}{\partial x_i^*} = 0, \tag{2.4}$$

$$\frac{\partial u_i^*}{\partial t^*} + \frac{\partial(u_i^* u_j^*)}{\partial x_j^*} = -\frac{\partial p^*}{\partial x_i^*} + \frac{1}{Re}\left(\frac{\partial^2 u_i^*}{\partial x_j^* \partial x_j^*}\right), \tag{2.5}$$

with the Re the Reynolds number:

$$Re = \frac{\rho U L}{\mu}. \tag{2.6}$$

For readability, the asterisks are dropped in the remainder of this chapter. Unless mentioned otherwise, the variables in this chapter represent non-dimensional variables.

Equations (2.5) describe the conservation of momentum in the x-, y- and z-direction and can be considered as equations for the velocities u, v and w. The continuity equation, equation (2.4), constrains the velocity field instead of providing a direct equation for another variable. The incompressible Navier-Stokes equations have no direct equation for the pressure. The coupling between velocity and pressure, which shows here through the absence of a direct equation for the pressure, is a main challenge in solving the incompressible Navier-Stokes equations [17]. The solution strategies to overcome the aforementioned issue are generally divided into density-based and pressure-based approaches.

Density-based approach

Density-based approaches recognize the applicability of compressible flow algorithms to incompressible flows. Since incompressible flow is only an approximation to compressible flow, the compressible Navier-Stokes equations govern compressible as well as incompressible flow. To solve the compressible Navier-Stokes equations, the velocities are computed from the momentum equations, the density from the continuity equation, the temperature from the energy equation and the pressure from a thermodynamic equation of state. The treatment of incompressible flow as a limiting case of compressible flow introduces an additional challenge as it couples acoustics to the problem. In incompresssible flow, the pressure disturbances associated with acoustics propagate much faster and with a different mathematical character than the flow velocity. These propagation differences make it difficult to obtain a converging solution.

One of the earliest density-based approaches is the artificial compressibility method developed by Chorin [33]. Chorin altered the incompressible continuity equation via the introduction of a time-derivative for the pressure. The artificial continuity equation mimics the mathematical character of the compressible continuity equation. The time derivative is multiplied (or: pre-conditioned) by an artificial speed of sound $1/\beta$ to deal with the difference in propagation between the pressure disturbances and the flow velocity. The artificial continuity equation is given by:

$$\frac{1}{\beta}\frac{\partial p}{\partial t} + \frac{\partial u_i}{\partial x_i} = 0. \tag{2.7}$$

For a steady flow, the time-derivative goes to zero at convergence and the incompressible continuity equation recovers. Convergence properties and accuracy of the solution strongly depend on the value chosen for β. A generalization of the artificial compressibility method in which all equations are pre-conditioned is implemented in SU2 by Economon for incompressible flows with density variations and heat transfer [20].

Pressure-based approach

Pressure-based approaches solve the incompressible Navier-Stokes equations using a Poisson equation for the pressure. The derivation of a Poisson equation is based on combining the continuity equation and momentum equations. Following the form of the continuity equation, the divergence is taken of the momentum equations. The unsteady term and the viscous term are cancelled out because the velocity field is required to be divergence free. A Poisson equation for the pressure is obtained [18]:

$$\frac{\partial}{\partial x_i}\left(\frac{\partial p}{\partial x_i}\right) = -\frac{\partial}{\partial x_i}\left[\frac{\partial (u_i u_j)}{\partial x_j}\right]. \tag{2.8}$$

Several different algorithms have been developed to solve the incompressible Navier-Stokes equations using a pressure-based method. The Semi-IMplicit Pressure Linked Equations (SIMPLE) algorithm [34] and Pressure Implicit with Splitting of Operators (PISO) algorithm [35] are implemented in SU2 by Koodly Ravishankara [21]. Both algorithms estimate a velocity field using the momentum equations based on a guessed pressure field. The estimated pressure and velocity fields are thereafter corrected to satisfy the continuity and momentum equations. The correction is performed using one correction step in the SIMPLE algorithm and using two correction steps in the PISO algorithm. The SIMPLE algorithm is used in this study and further elaborated on in Section 2.3.3.

2.2 Turbulent flow

Wind turbines operate in turbulent flow with high Reynolds numbers. Turbulent flows are very unsteady, irregular, chaotic and seem random. A fundamental property of turbulent flow is the rapid fluctuation of the velocity field in all spatial directions around a mean value. The modelling of turbulence is difficult as turbulence is composed of turbulent motions called 'eddies' in a wide range of scales. The motion of eddies is also associated with the process called energy cascade: large eddies transfer some of their kinetic energy to smaller eddies which transfer some of their kinetic energy to even smaller eddies. The process continues until the kinetic energy of the smallest eddies dissipates through viscosity [36].

The modelling of turbulent flow can be categorized into three approaches. Direct Numerical Simulation (DNS) solves the Navier-Stokes equations for all different turbulent length and time scales. The range of scales is very large, especially for flows with high Reynolds numbers, due to which DNS is too computational expensive for practical applications. Large Eddy Simulation (LES) solves the larger turbulent scales and models the effect of the smaller turbulent scales. It can be considered as an intermediate form of turbulence modelling. The Reynolds-Averaged Navier-Stokes (RANS) equations solve the time-averaged mean flow and model the effect of turbulent fluctuations on the mean flow. RANS is most widely applied for industrial application and considered in this study.

Reynolds-Averaged Navier-Stokes (RANS) equations

Turbulent flow is characterised by rapid fluctuations of its flow variables around a mean value. The fluctuation of a general flow variable ϕ around a steady mean is depicted in Figure 2.1. Reynolds decomposition defines the flow variables as the sum of the mean $\overline{\phi}$ and a fluctuating part ϕ' with a zero mean. The time-average or mean of the flow property and the time-average of the fluctuations are defined as:

$$\text{Time-average of the flow property:} \quad \overline{\phi} = \frac{1}{\Delta t}\int_0^{\Delta t} \phi(t)\, dt, \tag{2.9}$$

$$\text{Time-average of the fluctuations:} \quad \overline{\phi'} = \frac{1}{\Delta t}\int_0^{\Delta t} \phi'(t)\, dt \equiv 0. \tag{2.10}$$

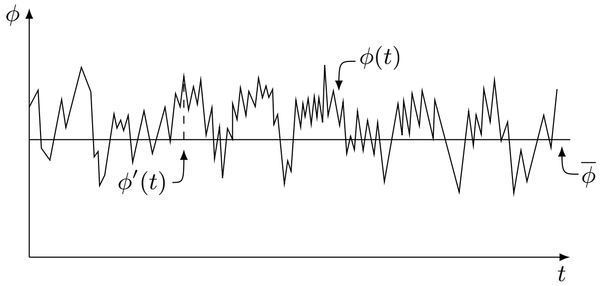

Figure 2.1: Mean $\overline{\phi}$ and fluctuating component $\phi'(t)$ of a flow variable $\phi(t)$ [37]

Application of the Reynolds decomposition to the velocities and the pressures gives:

$$u_i(t) = \overline{u_i} + u_i'(t), \tag{2.11}$$

$$p(t) = \overline{p} + p'(t). \tag{2.12}$$

The decomposed velocities and pressure are substituted in the incompressible Navier-Stokes equations, equations (2.4) and (2.5). Taking the time-average yields:

$$\frac{\partial \overline{u_i}}{\partial x_i} = 0, \tag{2.13}$$

$$\frac{\partial \overline{u_i}}{\partial t} + \frac{\partial(\overline{u_i}\,\overline{u_j})}{\partial x_j} = -\frac{\partial \overline{p}}{\partial x_i} + \frac{1}{Re}\left(\frac{\partial^2 \overline{u}_i}{\partial x_j \partial x_j}\right) - \frac{\partial(\overline{u_i' u_j'})}{\partial x_j}. \tag{2.14}$$

The resulting set of equations (2.13) and (2.14) are called the Reynolds-Averaged Navier-Stokes (RANS) equations. They are very similar to the Navier-Stokes equations aside from the additional terms in the momentum equations which originate from non-linearity in the convective term. The additional terms, called Reynolds stresses, account for the effect of the fluctuations on the mean flow. They are turbulent stresses and arise due to convective momentum transfer by the turbulent eddies. The Reynolds shear stresses define three additional normal stresses and three additional shear stresses. As the normal stresses contain squared velocity fluctuations, they are always non-zero. The shear stress are usually non-zero because the fluctuating velocity components are correlated due to the structure of the eddies. Turbulent stresses can be very large compared with viscous stresses in a turbulent flow.

Reynolds-averaging the Navier-Stokes equations introduced six additional unknowns: the Reynolds stresses. They are often modelled using a turbulence eddy viscosity model. Turbulent eddy viscosity models are based on Boussinesq's turbulent-viscosity hypothesis. It supposes that Reynolds stresses have a similar effect on the mean flow as the viscous stresses and assumes that Reynolds stresses are mathematically similar to viscous stresses:

$$\text{Viscous stresses: } \tau_{ij} = \mu_{dyn}\left[\left(\frac{\partial u_i}{\partial x_j} + \frac{\partial u_j}{\partial x_i}\right) - \frac{2}{3}\delta_{ij}\frac{\partial u_l}{\partial x_l}\right], \tag{2.15}$$

$$\text{Reynolds stresses: } \tau_{ij} = \mu_{turb}\left(\frac{\partial u_i}{\partial x_j} + \frac{\partial u_j}{\partial x_i}\right) - \frac{2}{3}\delta_{ij}\left(\rho k + \mu_{turb}\frac{\partial u_l}{\partial x_l}\right), \tag{2.16}$$

with μ_{turb} the turbulent eddy viscosity and k the turbulent kinetic energy:

$$k = \frac{1}{2}\overline{u_i' u_i'}. \tag{2.17}$$

The set of equations for an incompressible turbulent flow can be thought of as similar to the incompressible Navier-Stokes equations in which the velocity field is replaced by the mean velocity field and the viscosity by the effective viscosity $\mu_{eff} = \mu_{dyn} + \mu_{turb}$. Additional equations for the turbulent eddy viscosity are modelled in turbulent eddy viscosity models. Examples of often used turbulent eddy viscosity models are the one-equation Spalart-Allmaras (SA) model [38] and the two-equation $k - \omega$ SST model by Menter [39].

2.3 Pressure-based solver in SU2

SU2 is a software package developed for computational analysis and design optimisation of problems governed by partial differential equations. The software package is open-source and freely available. SU2 was designed with such a software architecture that the applications available in SU2 can be extended and integrated via contribution of a wide range of users [19]. SU2 is under active development and generally well-maintained. To make SU2 wider available for the wind energy industry, a pressure-based solver was recently implemented [21]. Its general principles are discussed in this section.

2.3.1 Governing equations

SU2 solves partial differential equations formulated in the general form [19]:

$$\frac{\partial U}{\partial t} + \frac{\partial F^c}{\partial x_i} - \frac{\partial F^v}{\partial x_i} = Q, \tag{2.18}$$

with U the state vector, F^c the convective flux, F^v the viscous flux and Q the source term. For the incompressible Reynolds-Averaged Navier-Stokes equations, the state vector, convective flux, viscous and source term are given by:

$$U = \begin{Bmatrix} 0 \\ \rho u_i \end{Bmatrix}, \quad F^c = \begin{Bmatrix} \rho u_i \\ \rho u_i u_j \end{Bmatrix}, \quad F^v = \begin{Bmatrix} 0 \\ \tau_{ij} \end{Bmatrix}, \quad Q = \begin{Bmatrix} 0 \\ -\frac{\partial p}{\partial x_i} \end{Bmatrix}. \tag{2.19}$$

Here, τ_{ij} is the viscous stress tensor:

$$\tau_{ij} = \mu_{eff}\left(\frac{\partial u_i}{\partial x_j} + \frac{\partial u_j}{\partial x_i}\right), \qquad \text{with } \mu_{eff} = \mu_{dyn} + \mu_{turb}. \tag{2.20}$$

μ_{eff} is the effective viscosity, μ_{dyn} the dynamic viscosity and μ_{turb} the turbulent eddy viscosity. The user can select the SA or SST turbulent eddy viscosity model to solve for μ_{turb}.

2.3.2 Discretization

The governing equations are discretized using the Finite Volume Method (FVM). FVM divides the computational domain into smaller control volumes. In SU2, FVM is applied using an edge-based data structure on a median-dual vertex-based scheme. In a vertex-based scheme, control volume are centered around the vertices of the grid cells. Here, control volumes are non-overlapping. Figure 2.2 shows an example of a two-dimensional unstructured vertex-based grid in which the cell vertices are denoted by yellow circles, cell centroids by red circles, edge midpoints by black bullets and the control volume by a blue polygon. The control volume is constructed around a vertex by connecting the centers of adjacent grid cells sharing a vertex to the midpoints of the faces of the shared grid cells. The velocities and pressure are stored at the vertices, i.e. the grid arrangement is collocated, and fluxes are evaluated at the edge midpoints.

FVM integrates the governing (conservation) equations over the control volumes,

$$\int_{\Omega} \frac{\partial U}{\partial t}\, d\Omega + \int_{S} (F_i^c - F_i^v) \cdot n_i \, dS = -\int_{\Omega} \frac{\partial p}{\partial x_i}\, d\Omega, \tag{2.21}$$

in which the convective and viscous flux functions are integrated over the surface of the boundary of a control volume S. Ω is the volume of a control volume and n_i the unit normal outward vector.

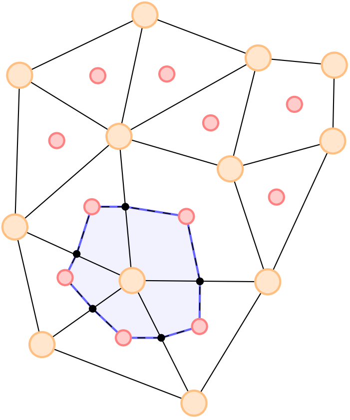

Figure 2.2: Unstructured vertex-based grid [37]

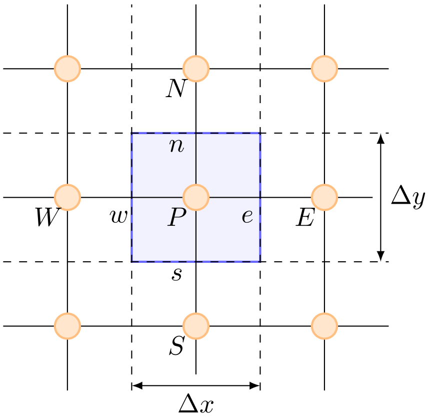

Figure 2.3: Control volume around node P

Spatial discretization

The integrals in equation (2.21) need to be approximated. The integrals over the entire surface are written as sum of the integrals over the surface of the separate faces of a control volume. These are evaluated using the midpoint integration rule which requires an approximation to the flux functions at the midpoint of an edge. The viscous flux is approximated by a central difference scheme in which a correction is applied for mesh non-orthogonality. Spatial gradients can be computed using Green-Gauss or Least-Squares [40]. The convective flux is approximated using an upwinding scheme which selects the upwinding direction corresponding to the direction of positive mass flux. The upwinding scheme is a first-order accurate spatial discretization and may introduce unphysical oscillations. A second-order accurate monotonic spatial discretization is accomplished via the Monotonic Upstream-centered Scheme for Conservation Laws (MUSCL) approach [41]. The MUSCL approach is available with several slope limiters, e.g. Venkatakrishnan [42] and van Albada [43]. The volume integral containing the pressure gradient is approximated by direct application of the midpoint integration rule.

Consider the 2D control volume around node P bounded by the faces e (east), s (south), w (west) and n (north) as shown in Figure 2.3. For the control volume around the node P, the semi-discretization of equation (2.21) is written as:

$$\int_{\Omega} \left(\frac{\partial U}{\partial t}\right)_P d\Omega + a_P^u u_P + \sum_{nb} a_{nb}^u u_{nb} = b_P. \tag{2.22}$$

Here, u_P are the velocities in node P, u_{nb} the velocities in the neighbouring nodes, a_P^u contains viscous and convective coefficients for the node P and a_{nb}^u contains the viscous and convective coefficients for the neighbouring nodes nb of node P. The superscript u denotes that a_P^u and a_{nb}^u are a function of the velocity field. The derivation of a_P^u and a_{nb}^u is given in [21]. b_P is the discretized source term. For the control volume around the node P in Figure 2.3, the neighbouring nodes are E (East), S (South), W (West) and N (North).

Time integration

For steady flows, the equations are integrated in time from t^n to t^{n+1} using implicit Euler:

$$\frac{U_P^{n+1} - U_P^n}{\Delta t}|\Omega|_P - a_P^u u_P^{n+1} + \sum_{nb} a_{nb}^u u_{nb}^{n+1} = b_P^n. \tag{2.23}$$

The time integration for steady flows is performed using local time stepping. The timestep should not be larger that the time it takes for the flow to propagate through a control volume. The local timestep is thus selected based on stability requirements for the viscous and convective flux.

$$\Delta t = \min(\Delta t^c, \Delta t^v) \tag{2.24}$$

in which

$$\Delta t^c = \text{CFL}\frac{|\Omega|}{\lambda^c}, \qquad \text{with } \lambda^c = \sum_f |(u_f + u_{ref}) \cdot \vec{n}_f|\,\Delta S, \tag{2.25}$$

$$\Delta t^v = \text{CFL}\frac{|\Omega|^2}{\lambda^v}, \qquad \text{with } \lambda^v = \sum_f C\frac{\mu_{eff}}{\rho}\,\Delta S^2. \tag{2.26}$$

λ^c denotes the convective spectral radius, λ_v denotes the viscous spectral radius and CFL is the Courant-Friedrichs-Lewy number. u_f is the velocity at a face f, ΔS the surface of face f and n_f is the vector normal to face f. For the control volume around the node P in Figure 2.3, a summation over the faces f is a summation over the faces e, s, w and n. The surface of the faces s and n is given by Δx and the surface of the faces e and w is given by Δy. u_{ref} is a reference velocity and C is a constant set at 0.25. The CFL number is a user-defined value. To obtain fastest convergence, the largest possible CFL that does not cause divergence should be chosen. This is allowed as steady flows do not require an accurate time history.

System of linear algebraic equations

The discretized equations can be written as a system of linear algebraic equations. The system of linear algebraic equations can be solved using linear solvers. Linear solvers available to solve the system are Flexible Generalized Minimal Residual (FGMRES) [44] and Biconjugate Gradient Stabilized (BicGSTAB) [45]. Additionally, pre-conditioning methods are available.

2.3.3 Velocity-pressure coupling

SIMPLE algorithm

The SIMPLE algorithm was proposed by Patankar and Spalding to compute the velocities and pressure using a pressure-based approach on a staggered grid [34]. The momentum equations are advanced in time from t^n to t^{n+1} using implicit Euler and an estimated pressure field p^*. The momentum equations,

$$a_P^{u_i} u_{i,P}^* + \sum_{nb} a_{nb}^{u_i} u_{i,nb}^* = -\left(\frac{\partial p^*}{\partial x_i}\right)_P |\Omega|_P, \tag{2.27}$$

are solved for the estimated velocity field u_i^*. Using the continuity equation, an estimated mass flux $\dot{m}_f^*$ is found at each face of the control volume. A correction u_i' and p' is applied to the estimated velocities and pressure:

$$u_i = u_i^* + u_i', \tag{2.28}$$

$$p = p^* + p'. \tag{2.29}$$

Substitution of equations (2.28) and (2.29) in the momentum equations yields an expression for the velocity corrector

$$u'_{i,P} = -\frac{\sum_{nb} a^{u_i}_{nb} u^*_{i,nb}}{a^{u_i}_P} - \frac{1}{a^{u_i}_P}\left(\frac{\partial p'}{\partial x_i}\right)_P = \cancel{\tilde{u}'_{i,P}} - \frac{1}{a^{u_i}_P}\left(\frac{\partial p'}{\partial x_i}\right)_P . \tag{2.30}$$

Typical for the SIMPLE algorithm, the unknown $\tilde{u}'_{i,P}$ is neglected. Combining equation (2.28), the obtained expression for the velocity corrector and the continuity equation gives a Poisson equation for the pressure. It is referred to as the pressure-correction equation and given by:

$$\frac{\partial}{\partial x_i}\left[\frac{\rho}{a^{u_i}_P}\left(\frac{\partial p'}{\partial x_i}\right)\right]_P = \sum_f \dot{m}^*_f . \tag{2.31}$$

in which f is the face of a control volume.

The pressure-correction equation is solved for the pressure correction p' and equation (2.30) is solved for the velocity correction u'_i. The estimated pressure and velocity estimations are updated where the pressure correction is relaxed by an under-relaxation factor α_p. The application of the under-relaxation factor recovers the convergence properties which are reduced due to neglecting $\tilde{u}'$. Thus, the pressure-based solver in SU2 solves the momentum equations and continuity equation sequentially.

Rhie-Chow interpolation

The SIMPLE algorithm was developed for application on a staggered grid in which velocities are stored at the cell faces and pressure at the cell centers. It cannot be applied directly on a collocated grid because of the so-called checkerboard problem, i.e. nonphysical pressure oscillations may arise for a uniform pressure field. The checkerboard problem arises on a collocated grid because the approximation of the pressure gradient, using linear interpolation, only takes alternating nodes into account. It can be considered as a $2\Delta x$ approximation as shown in Figure 2.4. On a staggered grid, linear interpolation of the pressure gradient includes consecutive nodes and can be considered as Δx approximation. As a result, the checkerboard problem does not show.

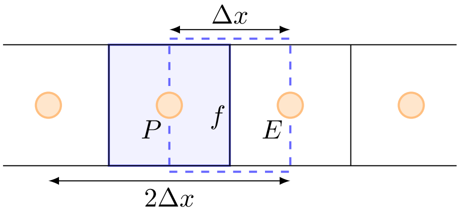

Figure 2.4: Two grid cells with a shared face f

Rhie and Chow [46] developed an interpolation technique to allow the application of the SIMPLE algorithm on a collocated grid. Consider a collocated grid in which the grid cell around the node P and the grid cell around the node E share a face f. A dashed rectangle is drawn around face f to indicate the suggestion of a staggered grid cell. Rhie and Chow derived an expression for the velocity at the cell face using an interpolation technique that imitates the staggered grid approach on a collocated grid:

$$u_f = \overline{u_f} - \overline{d_f}\left[\left(\frac{\partial p}{\partial x}\right)_f + \overline{\left(\frac{\partial p}{\partial x}\right)_f}\right] . \tag{2.32}$$

Here, the overline indicates a linear interpolation and $d_f = \rho(\Omega_f / a_f)$. Rhie-Chow interpolation damps checkerboard oscillations by including adjacent and consecutive nodes in the approximation. Using Rhie-Chow interpolation for the velocities, the SIMPLE algorithm can be applied on a collocated grid. The pressure-based solver in SU2 applies Rhie-Chow interpolation to the estimated face velocities u^*_f. It contains an additional term $(u^n_f - \overline{u^n_f})$ which arises as a consequence of its time-stepping scheme:

$$u^*_f = \overline{u^*_f} - \overline{\frac{|\Omega|}{\mathrm{RC}\, a^{t,n}_{f,u_i} + a^{jac,n}_{f,u_i}}}\left[\left(\frac{\partial p^n}{\partial x}\right)_f + \overline{\left(\frac{\partial p^n}{\partial x}\right)_f}\right] + (u^n_f - \overline{u^n_f}). \tag{2.33}$$

The term $\overline{d_f}$ is expanded to account for spatial and time dependencies in the viscous and convective coefficients. The time-dependent coefficients $a_{f,u_i}^{t,n}$ are relaxed by the relaxation factor RC. The solution becomes independent of the timestep, and thereby independent of the user-defined CFL number, by setting RC to zero. The relaxation factor RC should be chosen differently depending on convergence behaviour.

2.3.4 Boundary conditions

The Finite Volume Method approximation to the incompressible Navier-Stokes equations is computed on a bounded computational domain. A well-posed numerical problem requires boundary conditions which represent physics correctly. The control volume around a boundary node B with a boundary face b, Figure 2.5, requires a different treatment than the control volume around an interior node, Figure 2.3. Boundary conditions can be a direct description of an unknown boundary value (Dirichlet) or a description of an unknown boundary flux (Neumann). A combination of a direct value and a flux is also possible. Seven boundary conditions are implemented in the pressure-based solver in SU2. Considering the momentum equations and the mass flux, the no-slip wall boundary condition and specified velocity inlet are strong boundary conditions in which a value is directly described and the slip wall boundary condition, specified pressure outlet and symmetry boundary condition are weak boundary conditions in which a gradient is described. With regard to the pressure-correction equation, the pressure is treated using a Neumann boundary condition for the no-slip wall, slip wall, specified velocity inlet and symmetry boundary condition and using a Dirichlet boundary condition for the specified pressure outlet. The pressure is updated based on the pressure-correction equation. In the remainder of this section, the treatment of the boundary conditions concerning the momentum equations and mass flux are discussed.

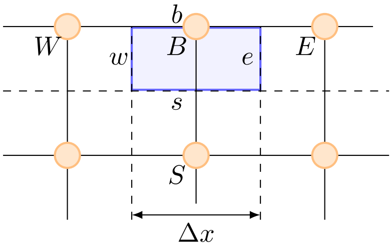

Figure 2.5: Control volume around a boundary node B with boundary face b

No-slip wall

The no-slip condition guarantees that the relative velocity between a wall and the air flow is zero and there is no flow through the wall. The wall boundary condition should be applied to surfaces where viscous effects are important. For example at an airfoil surface in an external flow. The zero relative velocity and zero flux are ensured by setting the boundary velocity u_b equal to the wall velocity u_{wall} and the mass flux at the boundary $\dot{m}_b$ at zero:

$$u_b = u_{wall}, \qquad \dot{m}_b = 0. \tag{2.34}$$

The pressure is treated using a Neumann boundary condition. Its value is updated based on the pressure-correction.

Slip wall

Alternatively, the slip wall boundary condition can be applied at a wall. The slip wall boundary condition allows for slip, i.e. relative movement between the boundary and the air flow and zero normal flux across the boundary. The mass flux across the boundary is equal to zero:

$$\dot{m}_b = 0. \tag{2.35}$$

The slip wall models frictionless surfaces. It is to be applied when viscous effects are not important such as a wall very far away or for boundaries in inviscid flows.

Specified velocity inlet

The specified velocity inlet boundary condition allows the user to prescribe a specific velocity u_{in} to the inlet boundary of the domain. A specific uniform velocity can be prescribed to an entire boundary as well as a non-uniform velocity profile. Using the specified velocity, the mass flux can easily be obtained:

$$\dot{m}_b = \rho u_{i,in} n_i \Delta S_b, \qquad u_b = u_{in}. \tag{2.36}$$

with ΔS_b the surface of the boundary face.

Specified pressure outlet

The specified outlet pressure boundary condition allows the user to prescribe a specific (gauge) pressure in Pascal at the outlet boundary of the domain. Its implementation assumes that the flow is fully developed when it reaches the outlet. Therefore, it is required that the domain is sufficiently long for the flow to become fully developed in order to obtain a correctly converged solution. The mass flux at the boundary is computed based on the velocity just upstream of the boundary $u_{i,b}$:

$$\dot{m}_b = \rho u_{i,b} n_i \Delta S_b. \tag{2.37}$$

Symmetry

The symmetry boundary condition mirrors the solution across the domain boundary and has zero normal flux due to which it does not allow for swirl. A symmetry boundary condition can be applied to problems that can be described with a plane of symmetry such that the mesh size can be reduced. In this manner, the computational time requirements can be reduced. When applied to a wall, the symmetry boundary condition is equivalent to the slip wall.

Far-field boundary condition

The far-field boundary condition is commonly applied in simulations concerning external flows. The boundary condition is used to denote free-stream properties. The far-field boundary condition allows the solver to switch between a specified velocity inlet when it experiences a negative mass flux and a specified pressure outlet when it experiences a positive mass flux in which the mass flux is computed as

$$\dot{m}_b = \rho u_{i,b} n_i \Delta S_b. \tag{2.38}$$

Periodic boundary condition

The periodic boundary condition exchanges a flux from a selected donor boundary to a selected receiver boundary as if the donor and receiver boundary were an internal element. The periodic boundary condition can be applied when a fluid problem is periodically repeating to reduce the mesh size and to reduce computational time. The periodic boundary allows for normal flow so can allow swirl.

2.3.5 Rotating frame of reference

It is computationally favorable to solve a flow over a rotating object, such as the flow over a rotor, using a rotating frame of reference. SU2 transforms the governing equations from a stationary frame of reference to a moving frame of reference using the Arbitrary Lagrangian Eulerian (ALE) formulation [47]. In the Lagrangian formulation, a fluid flow is described by following the fluid elements that move around. In the Eulerian formulation, a fluid flow is described as a function of time and space in a fixed location. The ALE formulation combines the Lagrangian and Eulerian formulation and allows for motion of the mesh in a Eulerian space. The ALE formulated is implemented by modification of the convective flux for the momentum equations and by modification of the Rhie-Chow interpolation:

$$F_i^c = \rho (u_i - u_{g,i}) u_j, \tag{2.39}$$

$$u^*_{rel,f} = \overline{u^*_f} - \overline{u_{g,f}} - \overline{D_f^{n,u}} \left[\left(\frac{\partial p'}{\partial x} \right)_f - \overline{\left(\frac{\partial p'}{\partial x} \right)_f} \right] + (u_e^n - \overline{u_e^n}). \tag{2.40}$$

The velocity u_i is the absolute velocity, i.e. the velocity in the stationary frame, $u_{g,i}$ is the grid velocity and $\overline{u_{g,f}}$ the linearly interpolated grid velocity at the face f.

The grid velocity for a steady rotating reference frame is given by the vector cross product of the angular velocity $\Omega_i = (\Omega_1, \Omega_2, \Omega_3)$ and the position vector r_j:

$$u_{g,i} = \epsilon_{ijk}\Omega_i r_j \hat{e}_k. \tag{2.41}$$

Here, ϵ_{ijk} is the Levi-Civita tensor, $\hat{e}_k$ a unit coordinate vector and the position vector $r = ((x-x_0),(y-y_0),(z-z_0))$ with (x,y,z) a point in the flow domain and (x_0,y_0,z_0) a specified rotation center.

A new source term is introduced for the momentum equations to account for apparent forces (Coriolis force and centrifugal force). The source term is given by the vector cross product of the angular velocity Ω and the velocity u:

$$Q = -\rho\epsilon_{ijk}\Omega_i u_j \hat{e}_k. \tag{2.42}$$

Chapter 3

Validation for 2D flow problems

In this chapter, the pressure-based solver that is implemented in SU2 is validated. The ability of the pressure-based solver to reproduce flow phenomena relevant in external aerodynamics is investigated. Three turbulent flow cases are considered: i) turbulent flow over a flat plate; ii) turbulent flow over a backward facing step; iii) turbulent flow over the NACA0012 airfoil. The numerical results are validated against analytical, experimental and numerical data from other studies. The three selected validation cases are included in the NASA Turbulence Modelling Resource which provides a resource with grids and additional information in relation to verification and validation of RANS models [48].

3.1 Turbulent flow over a flat plate

In this section, the capability of the pressure based solver to reproduce the turbulent boundary layer is investigated. The simplest case to study the turbulent boundary layer is the turbulent flow over a flat plate. It is a very suitable validation case as the turbulent boundary layer is the only external flow phenomena present. It is a case that is often used for the validation of turbulence models and available from the NASA Turbulence Modelling Resource [48].

3.1.1 Turbulent boundary layer

The turbulent boundary layer is a thin region of the turbulent flow next to the surface of the flat plate. It is made up of different layers. The turbulent boundary layer consists of an inner layer, formed by a viscous sublayer, buffer layer and log-layer, and an outer layer. The inner layer is dominated by viscous effects whereas the outer layer is dominated by turbulent effects. The different layers are schematically shown in Figure 3.1. The velocity profile $u(y)$, with y the distance from the wall, is also indicated. The velocity rapidly increases from zero at the surface of the flat plate to free-stream velocity at the boundary layer edge ($y = \delta$). In the viscous sublayer, the velocity increases linearly with the distance from the wall. The velocity increases logarithmically with the distance from the wall in the log-layer [36, 49]. The different layers have to be captured by the pressure based solver.

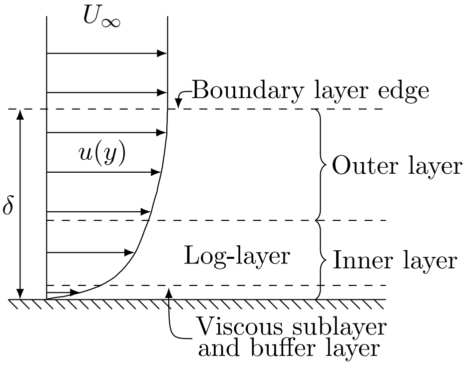

Figure 3.1: Schematic of the fully-developed turbulent boundary layer

The velocity profile within the viscous sublayer and the logarithmic region are typically described in terms of the non-dimensional distance from the wall in the direction normal to the wall y^+ and the non-dimensional velocity u^+:

$$\text{Viscous sub-layer: } u^+ = y^+, \qquad \text{for } y^+ \leq 5, \tag{3.1}$$

$$\text{Logarithmic region: } u^+ = \frac{1}{\kappa}\ln(y^+) + C, \qquad \text{for } y^+ > 30. \tag{3.2}$$

For a smooth plate, the von Kármán constant κ is 0.41 and the constant C is 0.5. The buffer layer is the layer in the region between $y^+ > 5$ and $y^+ < 30$.

The non-dimensional distance and velocity are defined by:

$$y^+ = \frac{y u_\tau}{\nu}, \tag{3.3}$$

$$u^+ = \frac{u}{u_\tau}, \tag{3.4}$$

in which y is the distance from the wall in direction normal to the wall, u_τ the wall friction velocity, ν the kinematic viscosity and u the local tangential velocity. The wall friction velocity is given by:

$$u_\tau = \sqrt{\frac{\tau_w}{\rho}}, \qquad \text{with } \tau_w = \frac{1}{2}\rho_\infty U_\infty^2 C_f. \tag{3.5}$$

Here, τ_w is the wall shear stress, ρ_∞ the free-stream density, U_∞ the free-stream velocity and C_f the skin friction coefficient.

3.1.2 Numerical method

The turbulent flow over a flat plate of 2 m was simulated with a Reynolds number of 5×10^6 based on a reference length of 1 m. The simulation was run using the SA and SST turbulence models. The convective flux was approximated using an Upwind-Difference Scheme (UDS) in combination with the MUSCL scheme and Venkatakrishnan limiter. The spatial gradients were evaluated using Green-Gauss and the linear system of algebraic equations was solved using FGMRES in combination with ILU preconditioning.

Three grids were considered with 57, 113 and 273 grid points on the surface of the plate [48]. The coarsest grid is depicted in Figure 3.2. It has 69 grid points in tangential direction, 49 grid points in normal direction and $y^+ \approx 0.71$. The finest grid has 273 grid points in tangential direction, 193 grid points in normal direction and $y^+ \approx 0.18$. The grid points are clustered near the wall to allow to resolve all layers of the turbulent boundary layer.

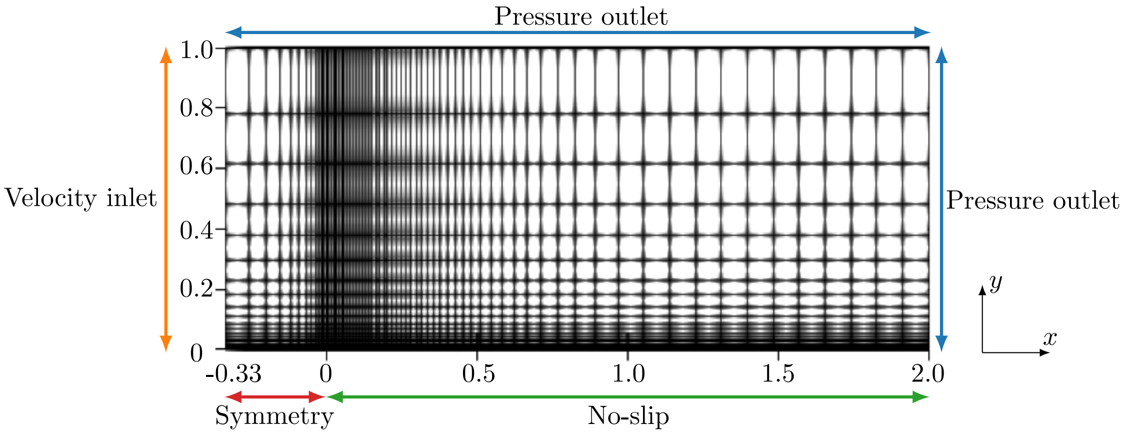

Figure 3.2: Coarse mesh, domain and boundary conditions

Along with the grid, the domain and boundary conditions are also shown in Figure 3.2. The domain ranges from $-0.33\,\mathrm{m}$ to $2\,\mathrm{m}$ in the x-direction and from $0\,\mathrm{m}$ to $1\,\mathrm{m}$ in the y-direction. The height of the domain is such that the farfield has no interaction with the boundary layer. The flat plate has a length of $2\,\mathrm{m}$ and starts at $x = 0\,\mathrm{m}$. It was modelled using a no-slip boundary condition. A uniform velocity is prescribed at the inlet. Before the plate, a symmetry boundary condition was adopted. The symmetry boundary condition prevents a mismatch in the boundary condition at the direct inlet and allows the flow to fully develop before reaching the plate. At both the farfield and the outlet, a pressure outlet with zero back pressure was prescribed.

3.1.3 Results

Grid convergence

The grid convergence was studied by extracting the skin friction coefficient at $x = 0.97\,\mathrm{m}$ for all simulations. The obtained values are listed in Table 3.1 in which 'lvl1' refers to the coarsest grid and 'lvl3' to the finest grid. The results in Table 3.1 indicate a convergence of the skin friction coefficient and a grid independent solution. The numerical solution corresponding to grid 'lvl3' are further analysed.

	SA	SST
lvl1	0.00271	0.00266
lvl2	0.00272	0.00269
lvl3	0.00273	0.00271

Table 3.1: Skin friction coefficient at $x = 0.97\,\mathrm{m}$

Skin friction coefficient

Figure 3.3 shows the skin friction coefficient as predicted along the surface of the flat plate. The skin friction coefficient decreases as the boundary layer develops. The SA and SST turbulence models predict comparable values for the skin friction. The numerical results of the pressure based solver are in good agreement with the results from CFL3D which is a compressibele RANS solver [48].

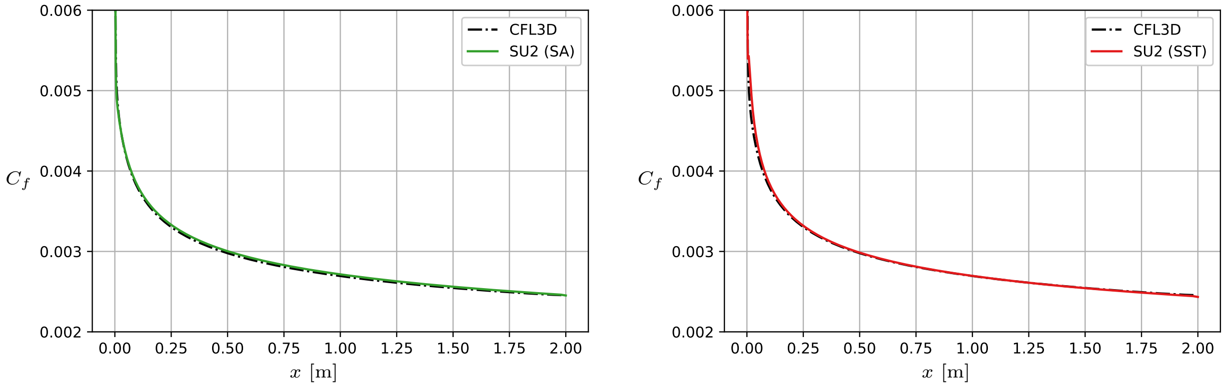

(a) SA turbulence model

(b) SST turbulence model

Figure 3.3: Comparison of the skin friction coefficient numerical results from SU2 and CFL3D [48]

Velocity profile

The numerical velocity profile in the viscous sublayer, the buffer layer and the log-law region is compared analytical description given in equations (3.1) and (3.2) at four different locations along the surface of the flat plate: $x = 0.10,\ 0.25$ and 0.97 and $1.98\,\mathrm{m}$. The comparison is graphically shown in Figure 3.4 for the SA and SST turbulence model.

Figure 3.4 shows that the ability of the the pressure-based solver to predict the viscous sublayer and log-law layer with both the SA and SST turbulence model. The numerical results are in good agreement

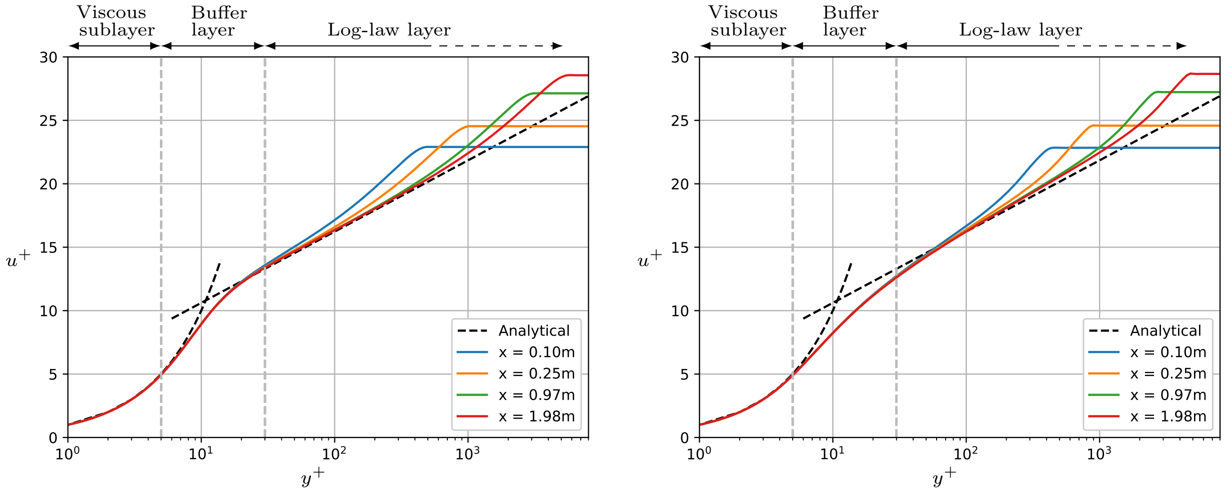

(a) SA turbulence model

(b) SST turbulence model

Figure 3.4: Comparison of the numerical and analytical velocity profile at four different locations

with the analytical results. The different locations demonstrate how the boundary layer develops along the plate. Close to the leading edge at $x = 0.10\,\mathrm{m}$, the flow is not fully developed yet and the characteristic velocity profile does not appear in the log-law layer. The characteristic profile starts to appear at $x = 0.25\,\mathrm{m}$ and becomes more pronounced at $x = 0.97\,\mathrm{m}$ and $1.98\,\mathrm{m}$. This shows that the thickness of the log-law layer increases with the development of the turbulent boundary layer. The SA turbulence model predicts a slightly faster velocity increase in the buffer layer and the log-law layer appears slightly closer to the wall.

The comparison of the numerical skin friction coefficient as predicted by the pressure-based solver and FUN3D as well as the comparison of the numerical and analytical velocity profiles show that the pressure-based solver is able to capture the turbulent boundary layer in combination with both the SA and SST turbulence model.

3.2 Turbulent flow over a backward facing step

The turbulent flow over a backward facing step with height H is schematically given in Figure 3.5. A fully-developed flow experiences an adverse pressure gradient due to the step and separates immediately. A thin shear layer, a recirculation zone with two dominant separation bubbles and a reattachment zone form. While propagating downstream, the shear layer extracts energy from the recirculation zone and growths in thickness. The shear layer is drawn down and reattaches at a downstream surface where a new boundary layer forms. In this section, the described case is simulated to validate the ability of the pressure-based solver in capturing the flow phenomena after flow separation.

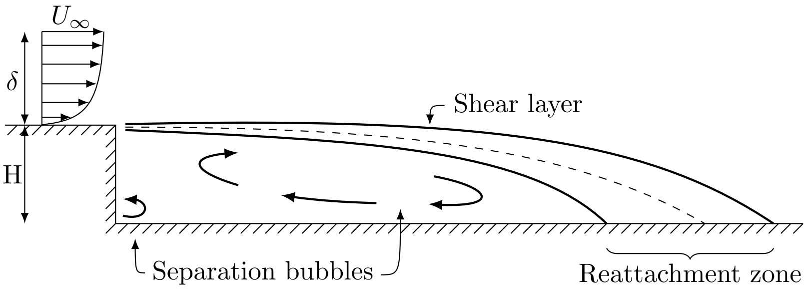

Figure 3.5: Schematic view of a turbulent flow over a backward facing step

3.2.1 Numerical method

A turbulent flow with a Reynolds number of 36 000 based on a step height $H = 1\,\mathrm{m}$ was simulated. The simulation was run using the SA and SST turbulence models. The convective flux was approximated using an Upwind-Difference Scheme (UDS). The MUSCL scheme was applied using the Venkatakrishnan limiter. The spatial gradients were evaluated using Green-Gauss and the linear system of algebraic equations was solved using FGMRES in combination with ILU preconditioning.

The simulation was run on a series of three grids [48]. The coarsest grid is shown in Figure 3.6 with a zoom in on the step in Figure 3.6b. The grid points were clustered near the step in both directions and stretched away from the step. The coarsest grid had approximately 5000 grid points and the finest grid had approximately 80 000 grid points.

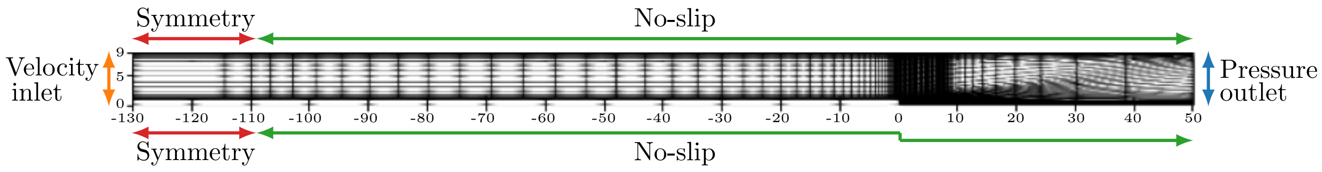

(a) Complete grid

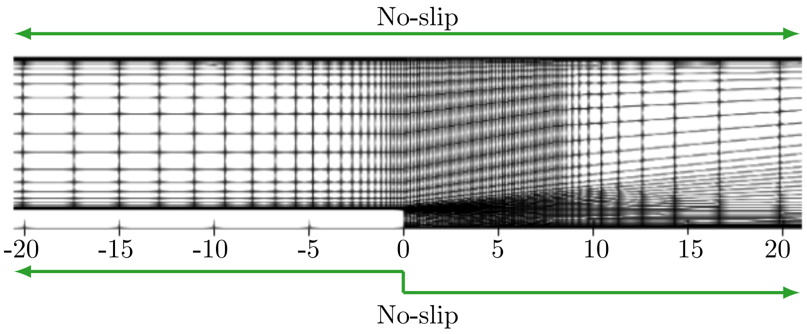

(b) Zoom in on the step

Figure 3.6: Coarse grid, domain and boundary conditions

The domain and boundary conditions are given in Figure 3.6. The domain ranged from $-130\,\mathrm{m}$ to $50\,\mathrm{m}$ in the x-direction and from $0\,\mathrm{m}$ to $9\,\mathrm{m}$ in the y-direction. The step had a height of $1\,\mathrm{m}$ and was located at $x = 0\,\mathrm{m}$. The start of the inlet channel was described by a symmetry condition and the bottom, top and step walls were modelled using a no-slip condition. A velocity was prescribed at the inlet and ambient pressure is prescribed at the outlet.

3.2.2 Results

Reattachment length

The reattachment length is the distance from the separation location to the time-averaged reattachment point. The reattachment point is the first point after separation where a velocity gradient with respect to the wall exists again and the skin friction coefficient is non-negative, i.e. $C_f \geq 0$. Table 3.2 lists the reattachment length obtained at the different grids in which ‘lvl1’ refers to the coarsest grid and ‘lvl3’ to the finest grid. The numerical solution corresponding to grid ‘lvl3’ is further analyzed.

The reattachment length predicted on grid ‘lvl3’ is $6.125\,\mathrm{m}$ using the SA turbulence model and $6.583\,\mathrm{m}$ using the SST turbulence model. The value found using the SA turbulence model is close to the value predicted by the compressible RANS solver CFL3D which predicts a reattachment length of $6.1\,\mathrm{m}$ [48]. Driver experimentally obtained a reattachment length of $6.26 \pm 0.01\,\mathrm{m}$ [50]. The numerical values lie around the experimental value.

	SA	SST
lvl1	6.167 m	6.667 m
lvl2	6.167 m	6.667 m
lvl3	6.125 m	6.583 m

(a) Convergence of the reattachment length

SU2 (SA)	6.125 m
SU2 (SST)	6.583 m
CFL3D (SA)	6.1 m
Experiment	6.26 ± 0.01 m

(b) Comparison of the reattachment length at grid 'lvl3'

Table 3.2: Reattachment length, with numerical results [48] and experimental data [50]

Skin friction coefficient

The skin friction coefficient at the lower wall is shown in Figure 3.7. It is compared against experimental data [50] and numerical results from the compressible RANS code CFL3D [48]. Generally, the numerical results obtained using the pressure-based solver and SA turbulence model are in good agreement with the numerical results from the compressible RANS code CFL3D and SA turbulence model. Upstream of the step, the numerical results are in good agreement with the experimental data. The negative skin friction coefficient downstream of the step indicates flow reversal within the recirculation zone. In the recirculation zone, a difference is observed between the numerical results and the experimental data as well as between the SA and SST turbulence models. The results obtained with the pressure-based solver predict a more negative skin friction value than the experiments. This is especially true for the SA turbulence model. The flow reattaches at $C_f = 0$ and a boundary layer recovers. The skin friction coefficient increases with downstream propagation and shows better agreement between the numerical results and experimental data.

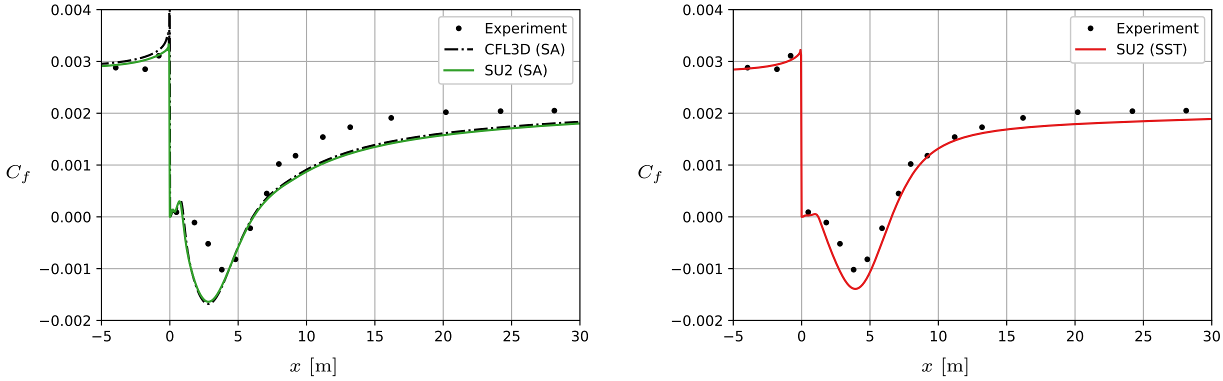

(a) SA turbulence model

(b) SST turbulence model

Figure 3.7: Comparison of the skin friction coefficient on the lower wall against experimental data [50] and numerical results from CFL3D with the SA turbulence model [48]

Velocity profile

The velocity profiles were extracted upstream of the step at $x = -4$ m and downstream of the step at $x = 1$, 4, 6 and 10 m. The velocity profiles, referenced against a reference velocity u_{ref} at $x = -4$ m and $y = 4.5$ m, are shown in Figure 3.8. Upstream of the step at $x = -4$ m, the numerical results and experimental data are in good agreement. The experimental velocity profiles in the recirculation zone, especially at $x = 1$ m, are best captured by the SST turbulence model. This is an indication that the SST turbulence model has a better ability to describe flow reversal than the SA turbulence model. However, near reattachment, at $x = 6$ m, the SA turbulence model is most corresponding to the experimental data which predict reattachment closer to the step than the SST turbulence model. Outside the recirculation zone, after reattachment at $x = 10$ m, all velocities are positive and close to the experimental value.

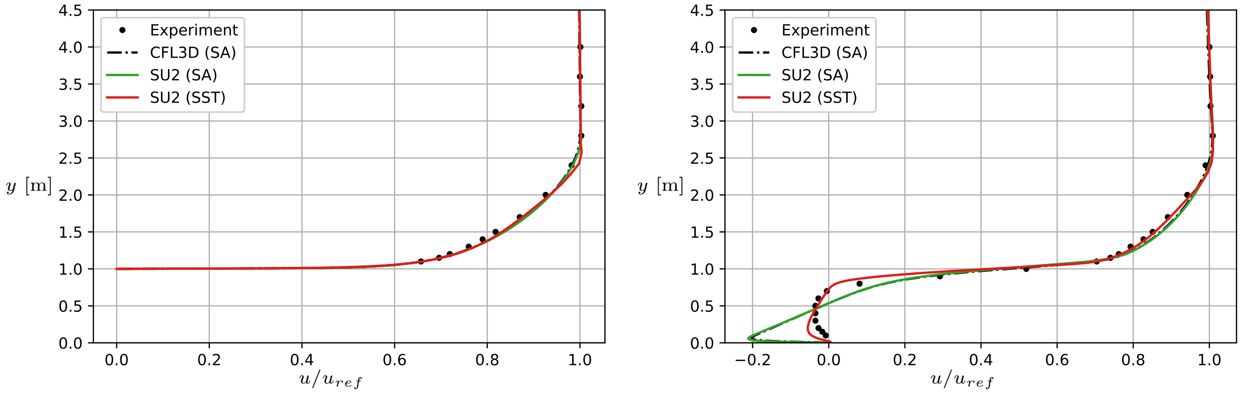

(a) $x = -4\,\mathrm{m}$ (b) $x = 1\,\mathrm{m}$

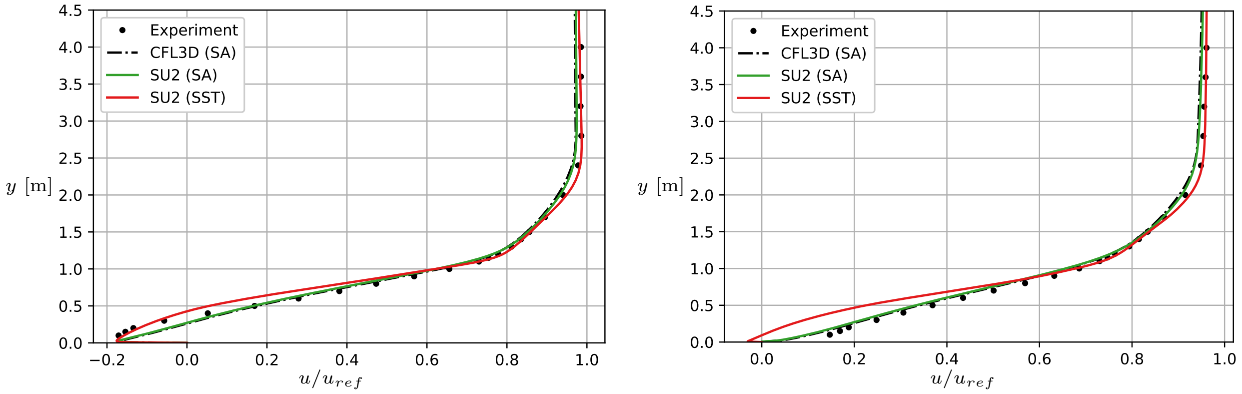

(c) $x = 4\,\mathrm{m}$ (d) $x = 6\,\mathrm{m}$

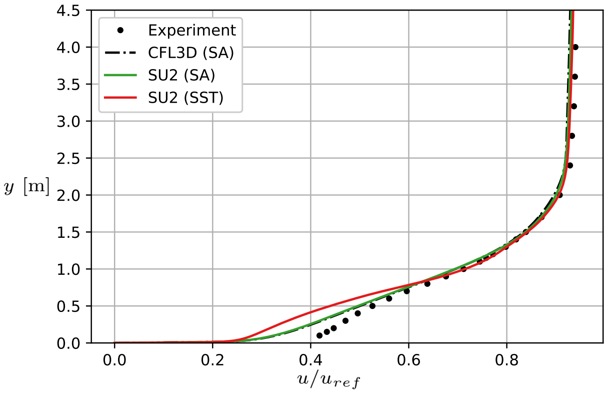

(e) $x = 10\,\mathrm{m}$

Figure 3.8: Comparison of the skin friction coefficient on the lower wall against experimental data [50] and numerical results from CFL3D with the SA turbulence model [48]

The comparison of the numerical reattachment length, skin friction coefficient and the velocity profiles as predicted by the pressure-based solver are in good comparison with numerical results from CFL3D. They are generally in fine agreement with experimental data. The SST model is found to follow the recirculation better. Flow separation and flow reversal is better captured by SST than by SA.

3.3 Turbulent flow over a NACA0012 airfoil

An airfoil is the cross-sectional shape of a wind turbine blade. This makes it very relevant that the pressure-based solver is capable of capturing the flow behaviour over an airfoil.

3.3.1 Flow over an airfoil - 2D aerodynamics

The flow over an airfoil - a cross-sectional shape of a wind turbine blade - is considered in the subject of two-dimensional (2D) aerodynamics. The flow over an airfoil becomes curved due to the shape of an airfoil. This is visualised by the streamlines in Figure 3.9a. The curvature of the streamlines affects the pressure distribution over the surface of the airfoil such that the pressure on the upper surface results in a suction away from the surface and the pressure on the lower surface results in a pressure into the surface. The interaction of the flow and the airfoil also yields a shear stress distribution. Integration of the pressure and shear stress distribution over the surface of the airfoil yields the resultant force R. The resultant force R is often decomposed into lift force L and drag force D.

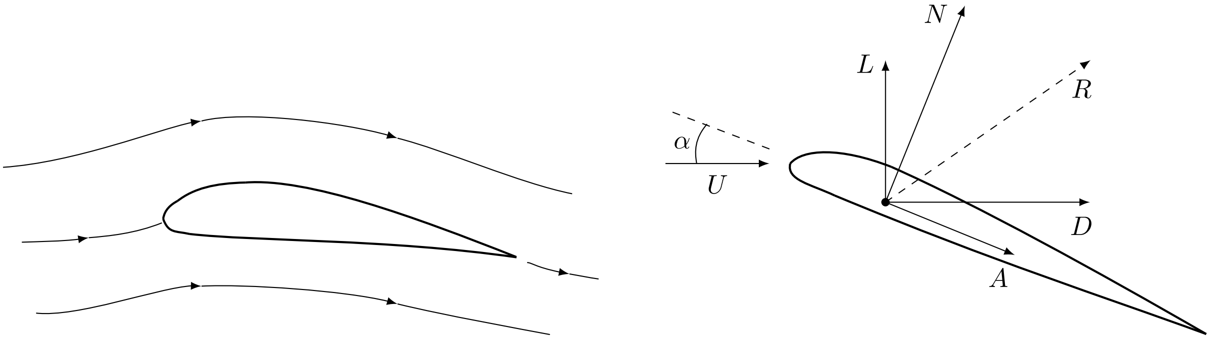

(a) Streamlines around an airfoil (b) Aerodynamic forces at an airfoil

Figure 3.9: Flow over an airfoil [51]

The pressure and shear stress as well as the lift and drag forces are often expressed in terms of non-dimensional coefficients:

$$C_p = \frac{p - p_\infty}{\frac{1}{2}\rho_\infty U_\infty^2}, \qquad C_f = \frac{\tau_w}{\frac{1}{2}\rho_\infty U_\infty^2}, \tag{3.6}$$

$$C_l = \frac{L}{\frac{1}{2}\rho_\infty U_\infty^2 c}, \qquad C_d = \frac{D}{\frac{1}{2}\rho_\infty U_\infty^2 c}. \tag{3.7}$$

Flow separation

The angle of attack is the angle between the free-stream velocity and the chord. The angle of attack α is included in Figure 3.9b. The streamlines over the airfoil become more curved with increasing angle of attack and more lift is generated. Consider the pressure distribution on the upper surface of the airfoil. The pressure is low and increases slowly towards the trailing edge. The adverse pressure gradient slows down the flow. The increase in pressure can lead to flow separation. At low or moderate angles of attack, the pressure increase is not strong and the flow remains attached. However, at large angles of attack, the adverse pressure gradient cannot be counteracted the flow separates and reverses. The airfoil is said to stall, lift generation is destroyed and drag becomes large. The flow after separation is very unsteady and difficult to predict.

3.3.2 Numerical method

The turbulent flow with a Reynolds number of 6×10^6 was simulated over the NACA0012 airfoil on a series of 4 grids [48]. A grid convergence study was performed for $\alpha = 10°$ and a grid was selected for further study. On the selected grid, the flow over the NACA0012 airfoil was simulated for a range of angles of attack: $\alpha = 0, 2, 4, 6, 8, 19, 12$ and $15°$.

The simulations were run using the pressure-based solver in combination with the SA and SST turbulence models. The convective flux was approximated using UDS. The MUSCL scheme was applied using the Venkatakrishnan limiter. The spatial gradients were evaluated using Green-Gauss and the linear system was solved using FGMRES in combination with ILU preconditioning.

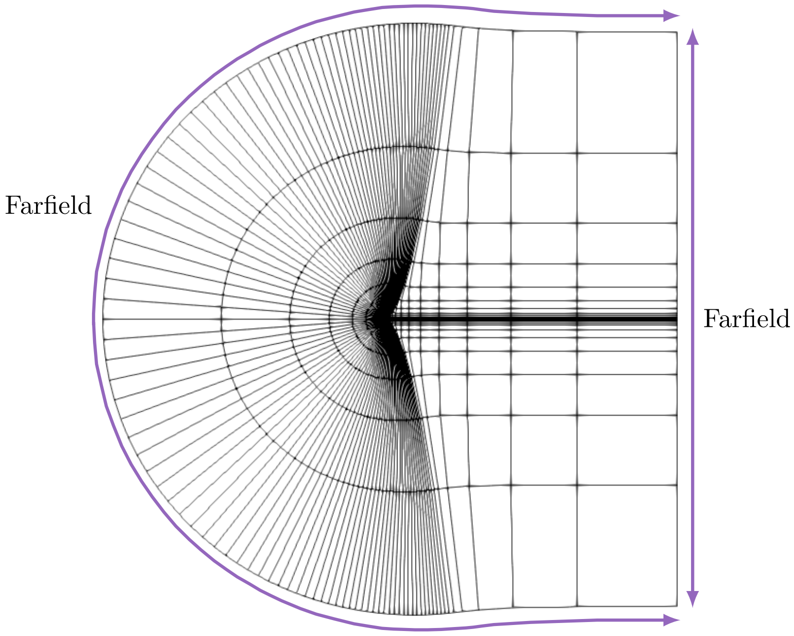

(a) C-type grid around the NACA0012 airfoil

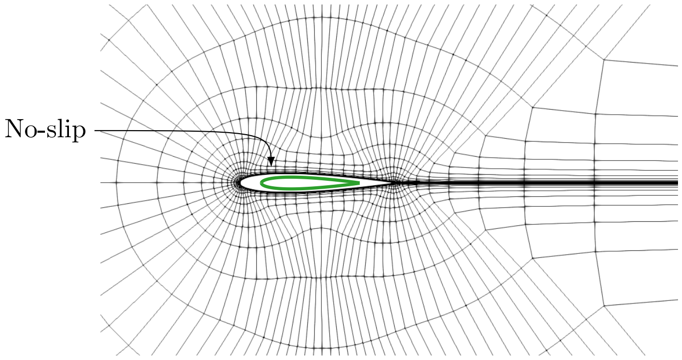

(b) Zoom in on NACA0012 airfoil indicating the no-slip boundary condition on the surface

Figure 3.10: Coarse grid and boundary conditions

The coarsest grid and boundary conditions are shown in Figure 3.10a. For more clarity, a zoom in on the airfoil is shows in Figure 3.10b. The grid is a C-type grid and the farfield is located 500 chords away from the airfoil. The coarsest grid has 128 grid points on the airfoil surface and the finest grid has 1024 grid points on the airfoil surface. The free-stream velocity is prescribed by:

$$u = U_{ref} \sin \alpha, \qquad v = U_{ref} \cos \alpha. \tag{3.8}$$

The airfoil is modelled by a no-slip condition and the outer boundaries by a farfield condition.

3.3.3 Results

Lift and drag coefficients

The lift and drag coefficient for $\alpha = 10°$ obtained using the different grids are given in Table 3.3. The compressible RANS solver CFL3D predicts, using the SST turbulence model, a lift coefficient of 1.078 and a drag coefficient of 0.0124 [48]. Grid 'lvl3' is selected for further analysis.

	SA	SST
lvl1	1.097	1.093
lvl2	1.089	1.081
lvl3	1.086	1.075
lvl4	1.085	1.073
CFL3D		1.078

(a) Lift coefficient

	SA	SST
lvl1	0.0130	0.0129
lvl2	0.0123	0.0122
lvl3	0.0123	0.0124
lvl4	0.0128	0.0125
CFL3D		0.0124

(b) Drag coefficient

Table 3.3: Convergence of the lift and drag coefficient for $\alpha = 10°$ compared against numerical values [48]

The lift coefficient as a function of the angle of attack is shown in Figures 3.11a and 3.11b and compared against experimental data. The experimental data is from an experiment of a flow over the NACA0012 airfoil at a Reynolds number of 6×10^6. The transition was fixed by tripping the flow at 0.05 % of the chord [52]. The numerical results and experimental data are in agreement, especially at low and moderate angles of attack. The SA turbulence model predicts slightly larger lift coefficients than the experiment and the experiment obtained slightly larger lift coefficients than the SST turbulence model. The drag coefficient as a function of the lift coefficient is compared against experimental data in Figures 3.12a and 3.12b [52]. The pressure-based solver predicts very similar values at low angles of attack and, especially for the SST turbulence model, slightly higher drag coefficient at higher angles of attack.

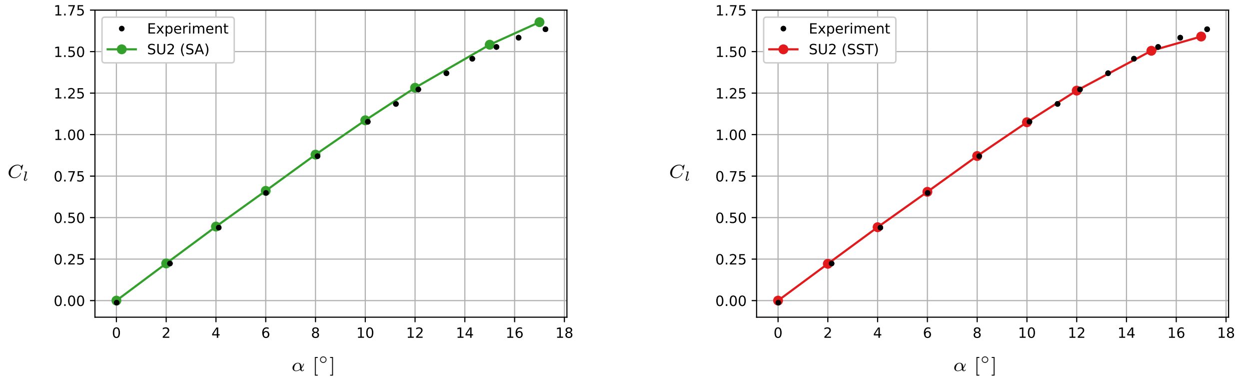

(a) SA turbulence model

(b) SST turbulence model

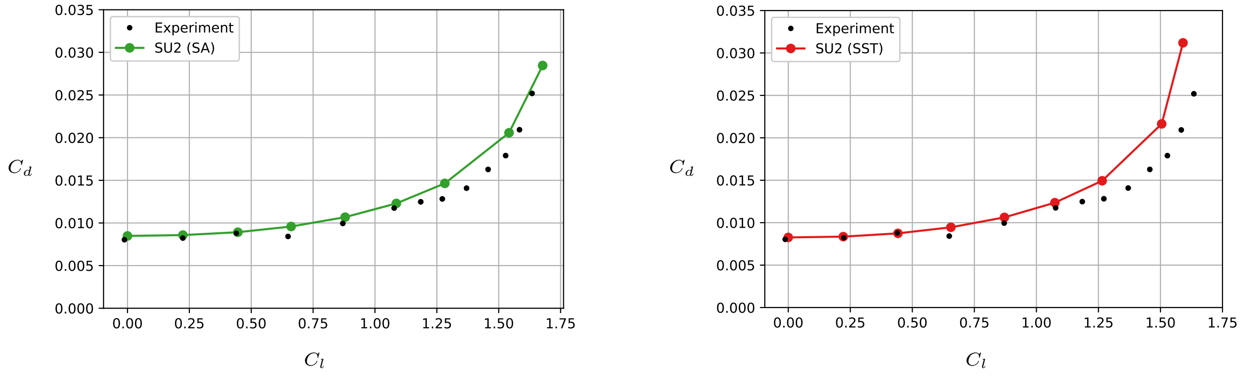

(a) SA turbulence model

(b) SST turbulence model

Figure 3.12: Comparison of the lift coefficient as function of the angle of attack and the drag coefficient as function of the lift coefficient against experimental data [52]

Pressure coefficient

The pressure coefficient for $\alpha = 0°$ and $\alpha = 15°$ are plotted in Figure 3.13. The results from the SST turbulence model are compared against results from the compressible RANS solver CFL3D in combination with the SST turbulence model [48]. The numerical results obtained with the pressure-based solver in SU2 are in good agreement with the numerical results based on CFL3D. For a zero angle of attack, the upper and lower surface have the same pressure distribution which is typical for symmetric airfoils. A greater suction peak is found at the upper surface for $\alpha = 15°$.

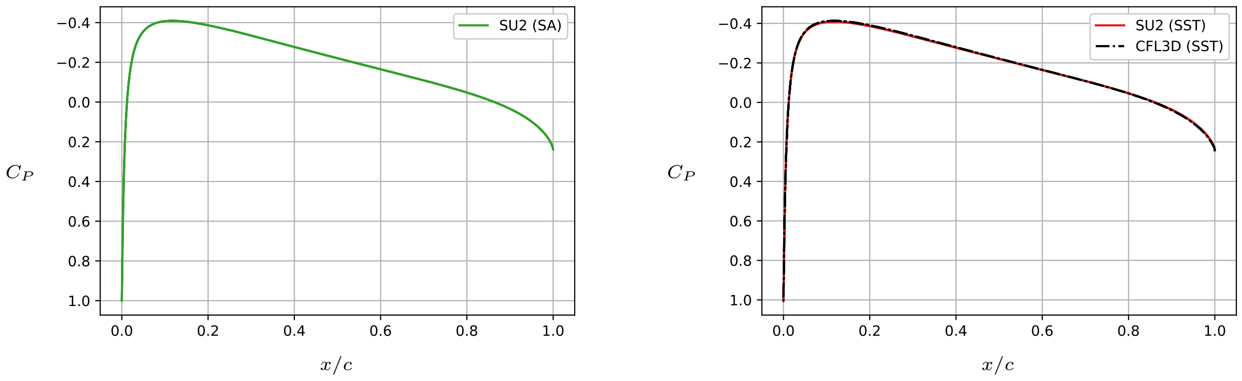

(a) SA turbulence model and $\alpha = 0°$ (b) SST turbulence model and $\alpha = 0°$

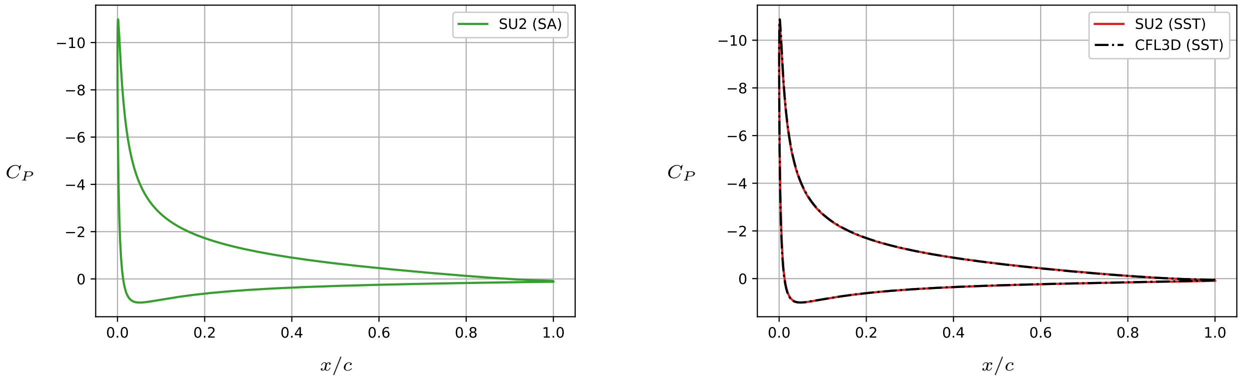

(c) SA turbulence model and $\alpha = 15°$ (d) SST turbulence model and $\alpha = 15°$

Figure 3.13: Comparison of the pressure coefficient on the surface of the NACA0012 airfoil against numerical results from CFL3D with the SST turbulence model [48]

Skin friction coefficient

The skin friction coefficient is plotted for $\alpha = 0°$ and $\alpha = 15°$ in Figure 3.14. The skin friction on the upper surface predicted using the SST turbulence model is compared against results from CFL3D in combination with the SST turbulence model. Figure 3.14a and 3.14b show that the upper surface and lower surface have the same skin friction distribution which is typical for symmetric airfoils at $\alpha = 0°$. Figure 3.14c and 3.14d depict the results for $\alpha = 15°$. The shear stress and skin friction decrease as the boundary layer develops and becomes thicker. The sign of the skin friction coefficient does not change which indicates that the flow remains attached over the airfoil surface.

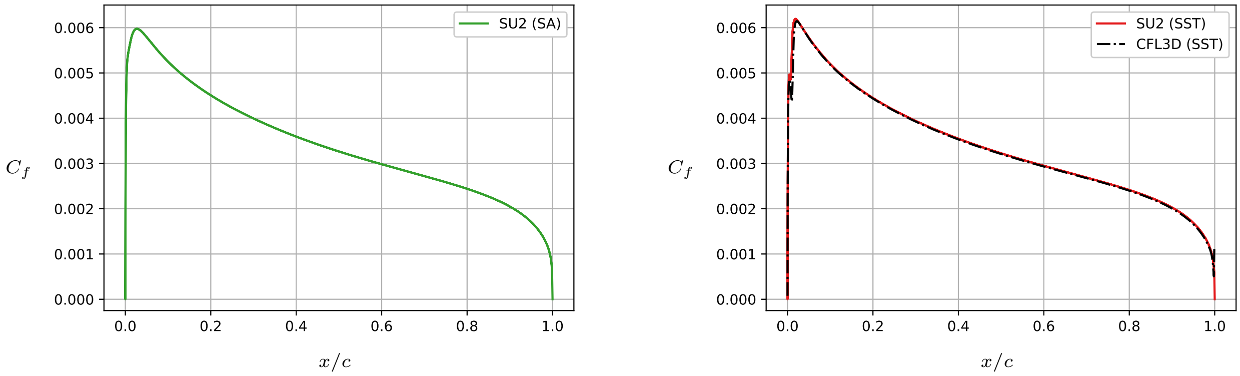

(a) SA turbulence model and $\alpha = 0°$ (b) SST turbulence model and $\alpha = 0°$

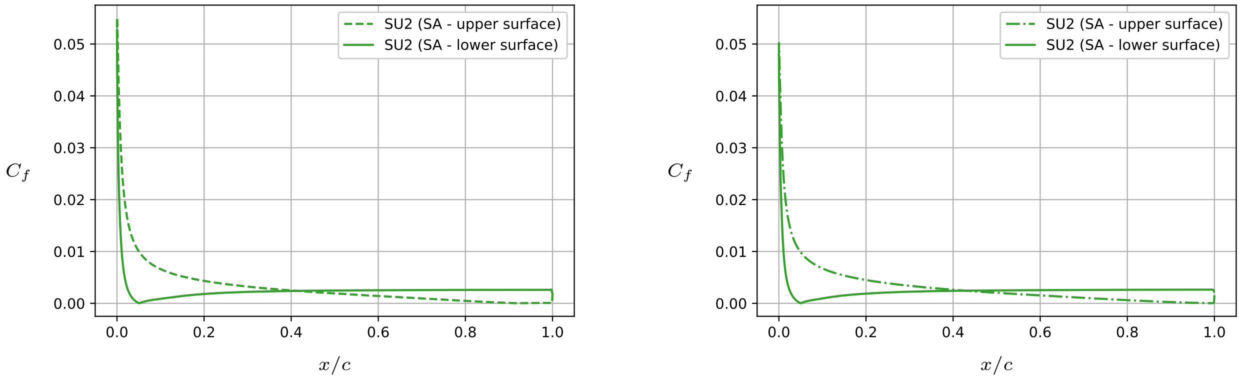

(c) SA turbulence model and $\alpha = 15°$ (d) SST turbulence model and $\alpha = 15°$

Figure 3.14: Comparison of the skin friction coefficient on the surface of the NACA0012 airfoil against numerical results from CFL3D with the SST turbulence model [48]

Flow field

The flow field around the NACA0012 airfoil under an angle of attack of 10° and 15° is visualised by streamlines and the pressure field in Figure 3.15. The streamlines split up at the leading edge of the airfoil, smoothly follow the curvature of the upper and lower surface of the airfoil and leave at the trailing edge. Increasing the angle of attack from 10° to 15° makes the streamlines more curved. Increasing the angle of attack also alters the pressure field. The pressure is low on the upper side of the airfoil and high on the lower side of the airfoil. For the greater angle of attack, lower pressures are observed and, as was already seen, the larger pressure difference between the two sides yields a higher lift coefficient.

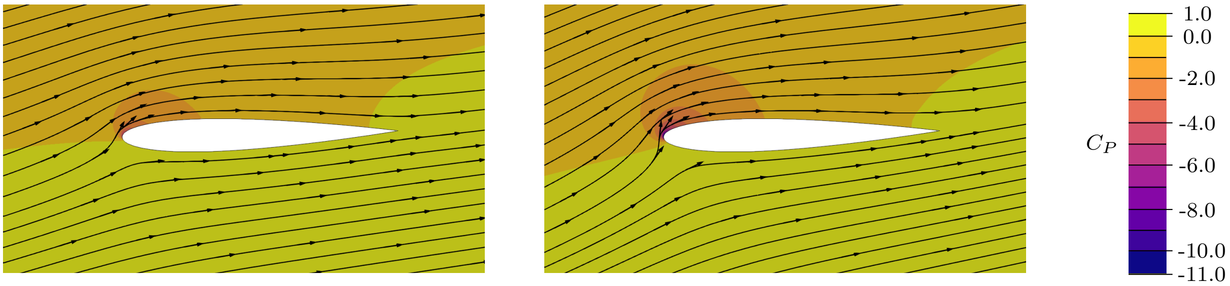

(a) $\alpha = 10°$ (b) $\alpha = 15°$

Figure 3.15: Flow field around the NACA0012 airfoil obtained using the SA turbulence model

Chapter 4

Rotor simulation

The pressure-based solver's ability to simulate a three-dimensional flow over a wind turbine rotor is considered in this chapter. Axial inflow conditions are studied for two different rotors related to two different experiment projects. The database generated by the Model EXperiments In Controlled cOnditions (MEXICO) and New MEXICO projects is very suitable for validation of Computational Fluid Dynamics (CFD) codes as pressure measurements at 5 blade sections and Particle Image Velocimetry (PIV) measurements of the flow around the rotor and the near wake were simultaneously performed. The database generated by the DanAero project contains blade pressures measured at four radial sections in the field on a full-size modern wind turbine. The MEXICO rotor is an extensively studied rotor and was the main topic of IEA Task 29 Phase III. The DanAero database is partially made available to participants of IEA Task 29 Phase IV and IEA Task 47 and is part of current simulation rounds.

4.1 Model EXperiments In Controlled cOnditions (MEXICO)

The pressure-based solver is validated against experimental data obtained in the MEXICO and New MEXICO projects [53, 24] and numerical studies applied to the MEXICO rotor [30, 54]. In the MEXICO and New MEXICO projects, a series of wind tunnel tests were performed. A three-bladed wind turbine rotor with a diameter of 4.5 m was placed in the Large Low-Speed Facility (LLF) of the German Dutch Wind tunnel (DNW). The experimental setup is shown in Figure 4.1. The blades of the MEXICO rotor consisted of three different airfoils: DU91-W2-250 in the root region ($0.20 < r/R < 0.456$), RISØ A1-21 in the middle ($0.544 < r/R < 0.655$) and NACA 64-418 near the tip ($0.744 < r/R < 1.00$). Pressure measurements were performed at 5 spanwise sections of the blade simultaneously with PIV measurements of the flow around the rotor and the near-wake. The measurements were performed under different operation conditions and different inflow velocities.

This study focuses on the MEXICO rotor operating under its design condition with axial inflow, i.e. zero yaw. The rotor speed was 425.1 rpm and the inflow velocity was $15\,\mathrm{m\,s^{-1}}$. The MEXICO rotor operated at a tip speed ratio of 6.7 and under a pitch angle of $-2.3°$. The properties of the MEXICO rotor and flow conditions together with the properties of the 5 spanwise sections at which the pressure measurements were performed are tabulated as an overview in Table 4.1.

Number of blades	3
Rotor diameter	4.5 m
Pitch angle	$-2.3°$
Rotor speed	425.1 rpm
Wind speed	$15.06\,\mathrm{m\,s^{-1}}$

(a) MEXICO rotor and flow conditions

r/R	Airfoil type	Chord	Twist angle
0.25	DU91-W2-250	0.22 m	14.25°
0.35	DU91-W2-250	0.19 m	10.20°
0.60	RISØ A1-21	0.14 m	4.80°
0.82	NACA 64-418	0.11 m	2.38°
0.92	NACA 61-418	0.10 m	1.24°

(b) Properties of the spanwise sections

Table 4.1: Description of the MEXICO rotor operating in its design condition

Figure 4.1: Set-up of the MEXICO experiment [23]

4.1.1 Numerical method

The flow over the MEXICO rotor was simulated on a coarse grid. Fine grid results are obtained from [21]. The pressure-based solver was run in combination with the SA turbulence model. Viscous fluxes were discretized on a central scheme and convective fluxes on an upwinding scheme. The MUSCL scheme was applied with the Van Albada Edge limiter. The spatial gradients were evaluated using Green-Gauss and the linear system of algebraic equations was solved using FGMRES in combination with ILU preconditioning. The simulation was considered converged when the flow and wake were fully developed and a steady state was reached.

The simulation was performed in a rotating frame of reference rotating with a constant angular velocity of 44.52 $\mathrm{rad\,s^{-1}}$ in the streamwise direction around the centre of the rotor. The simulation was initialised at smaller angular velocities following [21]. Simulations were run at several intermediate stages: $\Omega =$ 10, 25, 35 and 40 $\mathrm{rad\,s^{-1}}$ before reaching the final stage of 44.52 $\mathrm{rad\,s^{-1}}$. The hub was modelled without rotation by prescribing a rotation of $-\Omega$.

Figure 4.2 shows the dimensions of the computational domain. The computational domain ranged from -2.5D upstream of the rotor to 5.5D downstream of the rotor in the streamwise direction where D is the diameter of the rotor. The domain has a cylindrical shape with a radius of 1.5D around the centre of the rotor. Because of flow symmetry, the modelled domain consisted of one blade and one-third of the hub of the MEXICO rotor. The rotor was modelled by a no-slip condition. A free-stream flow was defined and a velocity inlet of 15 $\mathrm{m\,s^{-1}}$ was described. A free-stream boundary condition was prescribed to the outlet and top of the cylinder and a periodic boundary condition ‘coupled’ the faces on the sides.

The coarse mesh had 60 nodes along the chord and 305 nodes along the span of the rotor. The fine mesh had 160 nodes along the chord and 288 along the span. In both meshes, the height of the first cell was 4×10^{-6} m and the mesh had $y^+ < 1$ on the rotor surface. A bounding box of 1.75 m × 0.8 m × 2.5 m was created around the rotor with a hybrid meshing strategy. The boundary layer mesh consisted of 50 layers of hexahedral cells in the coarse mesh and 54 layers in the fine mesh. The bounding box was subsequently filled with tetrahedral and pyramid cells and its faces extruded to the extend of the domain with hexahedral cells. The coarse mesh contained 14.9×10^6 cells and the fine mesh 25.4×10^6 cells.

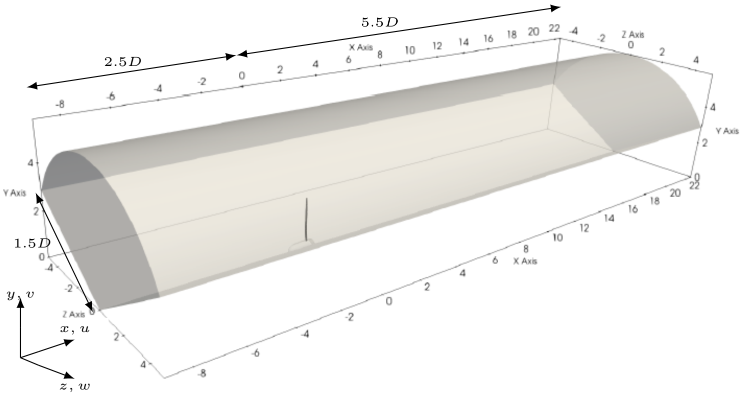

Figure 4.2: Computational domain around one-third of the MEXICO rotor

4.1.2 Results

The results from the simulation of the MEXICO rotor in axial inflow and operating under design conditions are studied in this section. The simulation on the coarse grid was performed in this study and the results from a simulation on the fine grid are adopted from [21]. Experimental values from the New MEXICO project are available for comparison as well as numerical results obtained using the CFD codes Ellipsys3D and OpenFoam [30, 54]. OpenFoam data is only available for the loads on the rotor. Ellipsys3D and OpenFoam approximated the RANS equations using the SIMPLE algorithm and $k-\omega$ SST turbulence model for the simulation of the MEXICO rotor. The meshes used in all numerical simulations were based on the same CAD-files containing the geometry of the MEXICO rotor. The sectional geometries of the 5 spanwise sections at which the pressure measurements were performed are compared firstly. Thereafter, the loads on the MEXICO rotor are investigated and finally the velocity field of the flow around the rotor and in the near-wake is studied.

Sectional geometry

The sectional geometries used in this study should be the same as the sectional geometries of the experimental MEXICO rotor and the same as the sectional geometries used in other numerical studies on the MEXICO rotor. Figure 4.3 shows the sectional geometries at $r/R = 0.25$, 0.35, 0.82 and 0.92. The sectional geometry at $r/R = 0.60$ is not shown because of confidentiality. The geometries at $r/R = 0.82$ and 0.92 as extracted from the coarse grid show a deviation in comparison against all other results. The sectional geometries comparison illustrates discrepancies in the rotor geometry in the coarse grid. For all radial positions, there is a small offset between the twist of Ellipsys3D and the other results. The geometry differences should be kept in mind while analyzing the loads on the rotor and the velocity field.

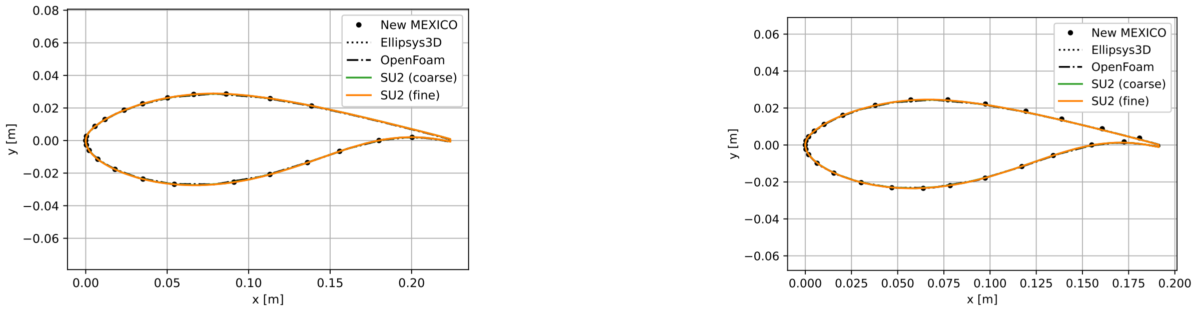

(a) $r/R = 0.25$

(b) $r/R = 0.35$

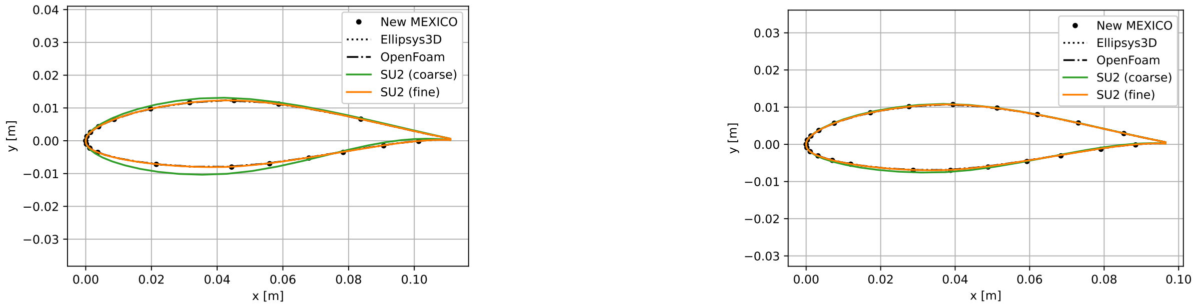

(c) $r/R = 0.82$

(d) $r/R = 0.92$

Figure 4.3: Comparison of sectional geometries

Loads

Pressure distribution The pressure contours on the surface of the suction side and pressure side extracted from the coarse mesh are shown in Figure 4.4. The pressure contours show a typical pressure distribution for a wind turbine blade. Pressure levels are low at the suction side. They are lowest at the trailing edge and increase towards the leading edge. At the pressure side, pressure levels are high and the pressure increases towards mid-chord of the blade and decreases towards the trailing edge.

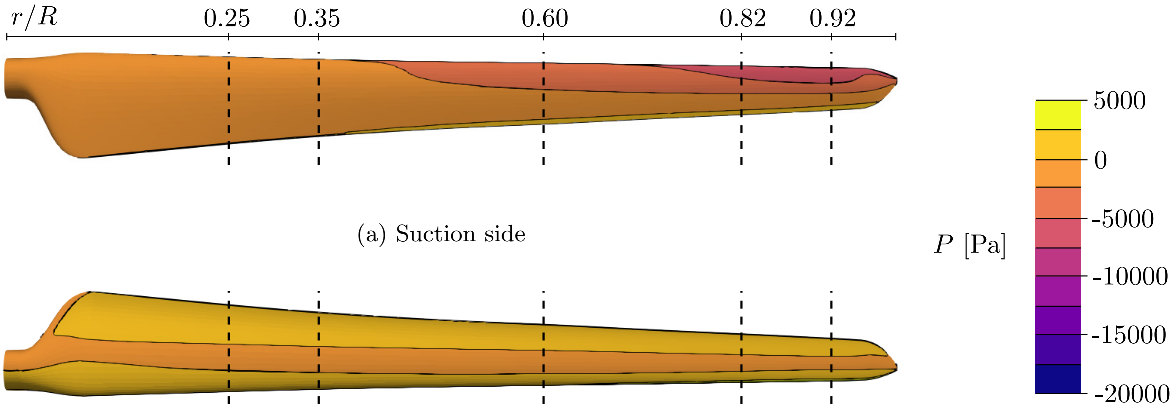

(a) Suction side

(b) Pressure side

Figure 4.4: Pressure distribution at the surface of the MEXICO rotor

The validity of the pressure distribution is evaluated by the comparison shown in Figure 4.5 at the five radial locations indicated by dashed lines in Figure 4.4. In Figure 4.5, the pressure distribution is expressed in terms of the pressure coefficient scaled with the local relative inflow velocity. The predicted pressure distribution is mostly in satisfactory agreement with the experimental values although its shape deviates at $r/R = 0.25$. A deviation in the predicted shape is also observed between the coarse and fine grid results at $r/R = 0.60$ and 0.82. This may be due to the discrepancy in the grid geometry. In general, the predicted pressure levels are somewhat higher than the measured pressures. The higher pressure levels are especially observed at the suction side of the blade.

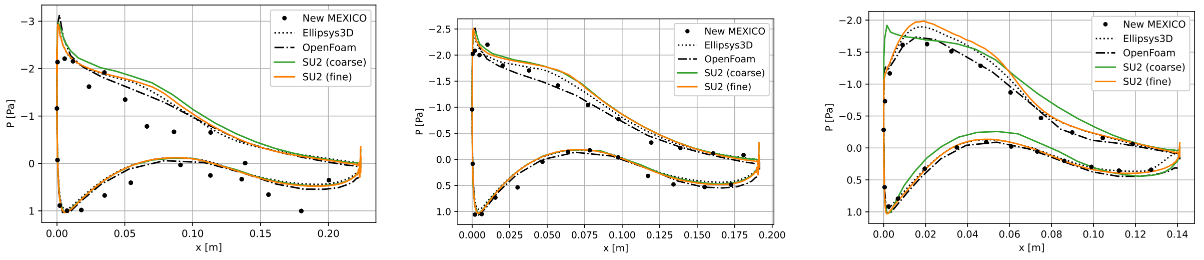

(a) $r/R = 0.25$ (b) $r/R = 0.35$ (c) $r/R = 0.60$

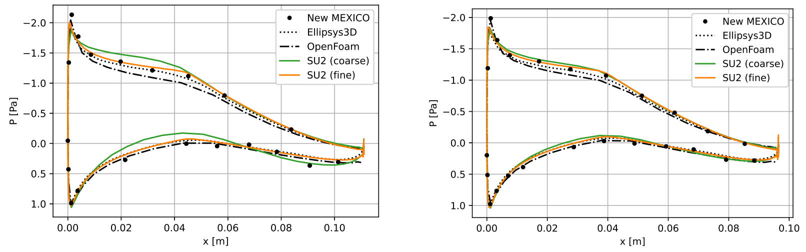

(d) $r/R = 0.82$ (e) $r/R = 0.92$

Figure 4.5: Pressure distributions at five radial locations comparing experimental data and numerical results

Shear stress distribution The shear stress distribution in terms of the normalized wall shear stress is shown in Figure 4.6 together with the streamlines from the coarse mesh. Again, the dashed lines indicate the pressure measurement locations. The streamlines were obtained with ParaView's Surface Line Integration Convolution (LIC) method. Flow separation is observed in the root region of the blade on the suction side near the trailing edge and flow attachment over most of the blade.

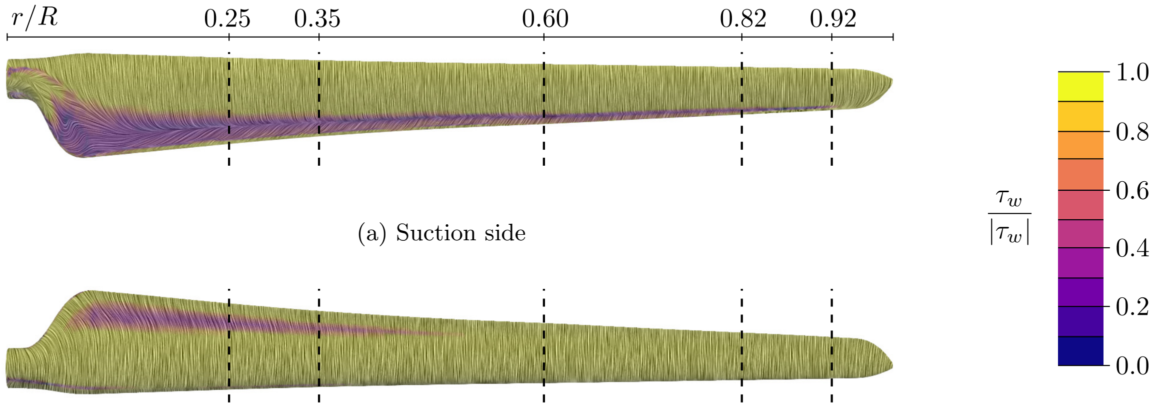

(a) Suction side

(b) Pressure side

Figure 4.6: Wall shear stress distribution and streamlines at the surface of the MEXICO rotor

The shear stress distribution is compared against results obtained using OpenFoam. The shear stress is given in terms of the magnitude of the skin friction coefficient which is scaled with the local relative inflow velocity. Figure 4.7 shows that the pressure-based solver in SU2 and OpenFoam generally compute similar skin friction coefficients. The skin friction coefficients predicted by the pressure-based solver are somewhat higher than the skin friction coefficients predicted by OpenFoam. The pressure-based solver in SU2 predicts unphysical wiggles.

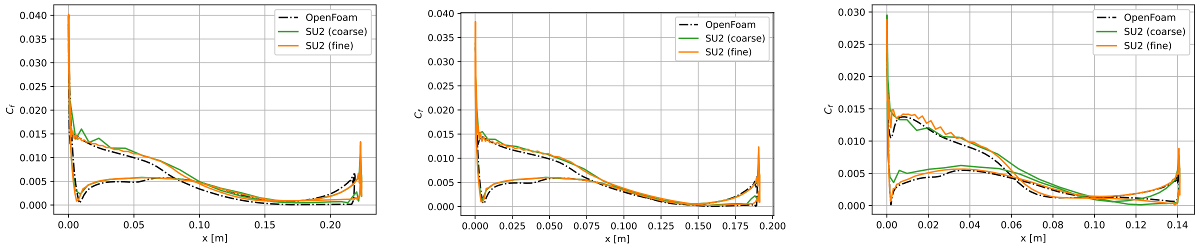

(a) $r/R = 0.25$ (b) $r/R = 0.35$ (c) $r/R = 0.60$

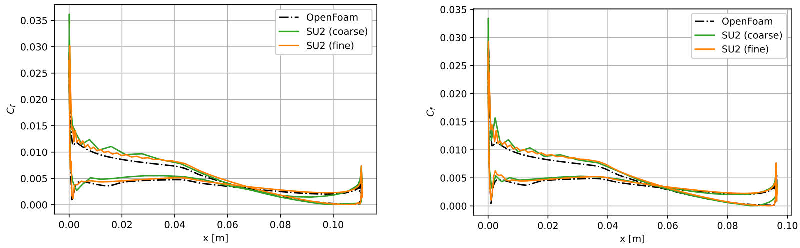

(d) $r/R = 0.82$ (e) $r/R = 0.92$

Figure 4.7: Shear stress distribution at five radial locations comparing results from OpenFoam to the pressure-based solvers results on the coarse and fine grid in terms of the magnitude of the skin friction coefficient

Normal and tangential force The normal and tangential force to the local chord are computed by integration of solely the pressure distribution as well as by integration of the pressure and shear stress distribution. The integrated forces are plot together with the other experimental and numerical values in Figure 4.8. The solid lines indicate the computed forces without shear stress and the dashed lines include shear stress. For comparison against experimental data and Ellipsys3D, the solid lines should be considered as only pressures were measured.

The normal and tangential forces should be consistent with the pressure distribution and the shear stress distribution. Pressures were generally little overpredicted, especially on the suction side of the blade. Overprediction on the suction sides cancels out the overpredicted on the pressure side and leads to underprediction of the normal force. This is observed in Figure 4.8a. The normal forces are in good agreement near the root and underpredicted near the tip in comparison against experimental data and in good agreement along the entire span with the results from Ellipsys3D. A discrepancy for the experimental value at $r/R = 0.60$ was consistently observed in [30]. Shear stress is excluded for the normal force as its influence is small. The contribution of shear stress on the tangential force is significant, Figure 4.8b. The different numerical codes and meshes are less closely together in the prediction of the tangential force. Including friction in the results reduces the tangential force by approximately 6.7 % on the coarse grid and 7.5 % on the fine grid.

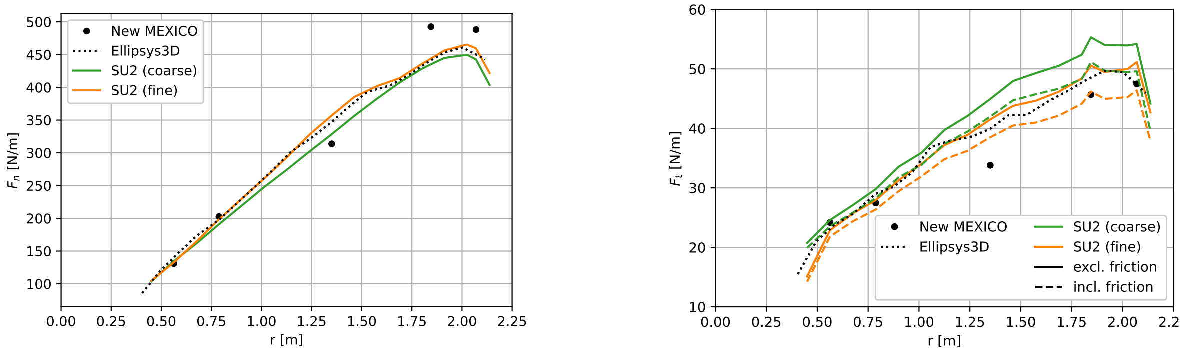

(a) Normal force (b) Tangential force

Figure 4.8: Normal and tangential force at the MEXICO rotor blade

Power and thrust coefficient The thrust and torque are computed from the normal and tangential force by spanwise integration. The spanwise integration is based on the normal and tangential force at the five measurement radial locations. A linear integration is performed with zero loading at the blade root and tip. Weighting factors are adopted from [30] and result in full rotor axial force and torque, i.e. for three blades. The contribution of friction is excluded for comparison against the measurement. The thrust and torque are used to calculate the power and thrust coefficient. The results are given in comparison against experimental data in Table 4.2. Similar as Ellipsys3D, the pressure-based solver in SU2 overpredicts the power coefficient but Ellipsys3D predicts the thrust coefficient more accurately. Although deviations were observed in the coarse grid geometry used in the simulation run using the pressure-based solver, this is consistent with the predicted normal and tangential forces.

	New MEXICO	Ellipsys3D	SU2 (coarse)	SU2 (fine)
C_P	0.438	0.49	0.495	0.469
C_T	0.775	0.77	0.723	0.756

Table 4.2: Power and thrust coefficient of the MEXICO rotor while operating under its design conditions

Velocity field

The ability of the pressure-based solver to predict the three-dimensional velocity field around the rotor and in the near-wake is validated by PIV data and numerical results from Ellipsys3D. PIV data was available from 4.5 m upstream of the rotor to 5.9 m downstream of the rotor in the format of axial, radial and azimuthal velocity traverses. The numerical results are also post-processed into axial, radial and azimuthal velocity traverses for which the cartesian velocities $u_i = (u, v, w)^T$ were transferred to cylindrical coordinates $u_i = (u, u_r, u_\theta)^T$. Here, u is the axial velocity component, u_r is the radial velocity component and u_θ is the tangential velocity component.

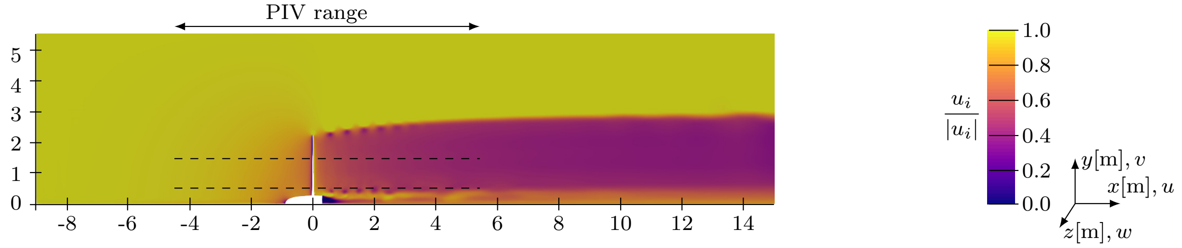

(a) u-component

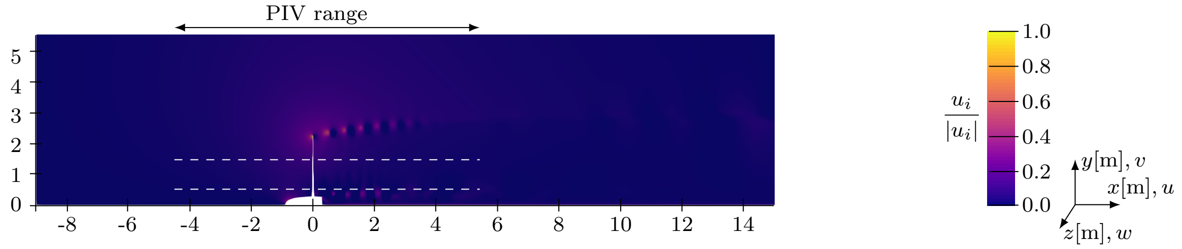

(b) v-component

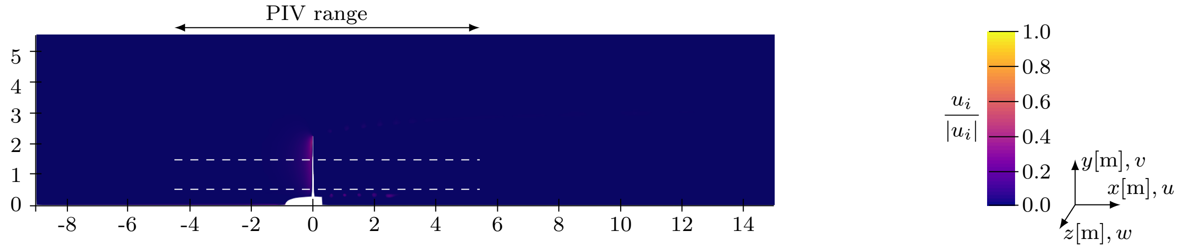

(c) w-component

Figure 4.9: Velocity field in the xy-plane

Figure 4.9 shows the velocity contours in the xy-plane for the u-, v- and w-components with dashed lines indicating the position of the axial velocity traverses, $r = y = 0.5\,\mathrm{m}$ and $r = y = 1.5\,\mathrm{m}$. The velocity contours are extracted from the coarse grid and show normalized velocities. The incoming flow is described by free-stream properties and propagates uniformly towards the rotor. Just upstream of the rotor, the flow slows down and a tangential and radial velocity component are induced. The interaction with the rotor slows down the wind and a wake develops downstream. The radial velocity component shows how the flow expands away from the blade. Upstream of the rotor the expansion indicates an expansion of the 'streamtube' and downstream of the rotor it shows wake expansion. A tangential velocity component is observed upstream as well as downstream of the rotor. Three-dimensional tip and root vortices are formed and convected downstream as the wake expands. Further downstream, the vortices reduce in strength and the wake recovers.

Axial velocity traverse The axial velocity traverses are compared against experimental data and numerical results at $r = 0.5\,\mathrm{m}$ in Figure 4.10 and at $r = 1.5\,\mathrm{m}$ in Figure 4.11. Upstream of the rotor, all velocity traverses are in good agreement and an increase of the u_r-component is observed due to modelling the hub. Differences are observed downstream. The large fluctuations in the axial velocity traverse at $r = 0.5\,\mathrm{m}$ are caused by the presence of the root vortex. The difference between the velocity fluctuations measured and predicted by the different methods is attributed to an offset in the prediction of the location of the root vortex. In the New MEXICO experiment, the axial velocity traverse at $r = 0.5\,\mathrm{m}$ slices through the root vortex whereas the pressure-based solver predicts the root vortex at slightly greater r. The axial velocity traverse at $r = 1.5\,\mathrm{m}$ slices through the wake convected from the blade. The tangential velocity component is most challenging to predict.

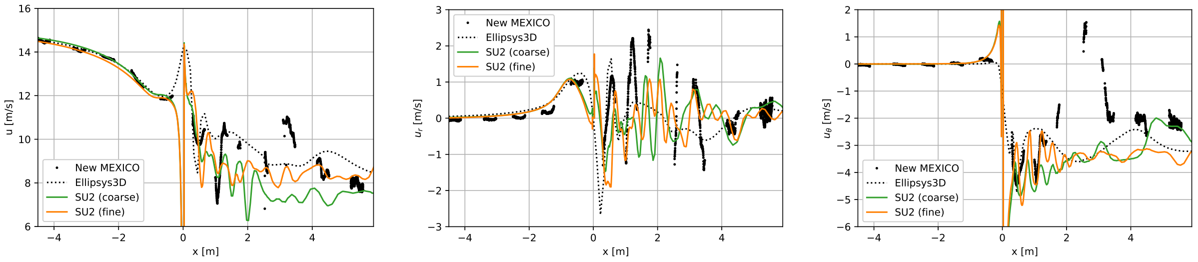

(a) Axial velocity component (b) Radial velocity component (c) Tangential velocity component

Figure 4.10: Axial velocity traverse at $r = 0.5\,\mathrm{m}$

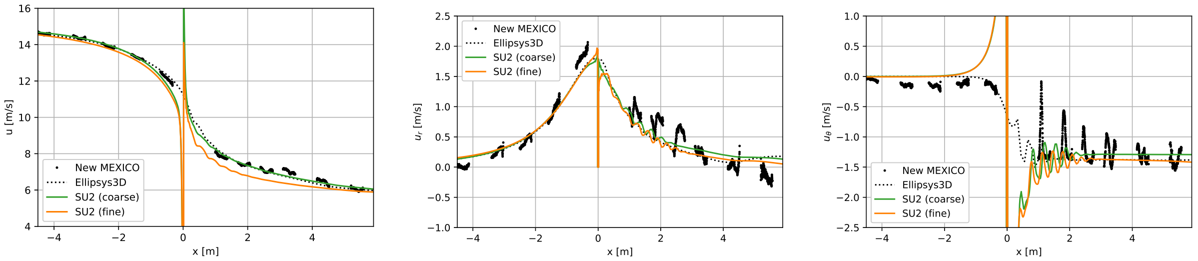

(a) Axial velocity component (b) Radial velocity component (c) Tangential velocity component

Figure 4.11: Axial velocity traverse at $r = 1.5\,\mathrm{m}$

Radial velocity traverse Radial velocity traverses are extracted from the yz-planes at 0.3 m upstream and 0.3 m downstream from the rotor. The velocities are extracted at several azimuthal locations and subsequently azimuthally averaged following the instructions in [30]. Figure 4.12 shows the upstream radial velocity traverses at $x = -0.3\,\mathrm{m}$ and Figure 4.13 shows the radial velocity traverses 0.3 m downstream of the rotor. Upstream of the rotor, the axial velocity component is slightly overpredicted and the radial velocity component is underpredicted. Both the axial and radial velocity component increase towards the tip of the blade. The fluctuation in the tangential velocity is not in agreement with either the experiment, which fluctuations are an indication of PIV uncertainty [30], or other codes used in the IEA

Task. The tangential velocity component upstream of the rotor was found to be mostly absent, but was predicted by some numerical codes. Downstream of the rotor, the axial velocity is reduced. Wake expansion is observed for the radial component. The predicted axial component is generally good agreement with the results from other studies and the radial velocity component is somewhat underpredicted. The tangential velocity component is more challenging to predict and a peak is observed downstream near the tip of the blade. This peak was not observed elsewhere [30]. The fine grid results show unphysical oscillations at radial locations greater than the blade radius.

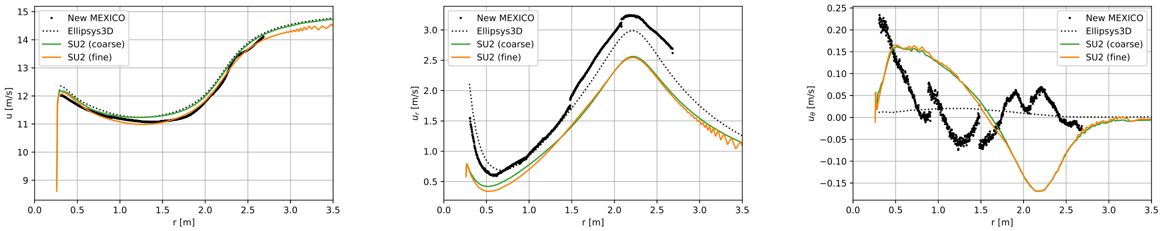

(a) Axial velocity component (b) Radial velocity component (c) Tangential velocity component

Figure 4.12: Radial velocity traverse upstream of the rotor at $x = -0.3\,\text{m}$

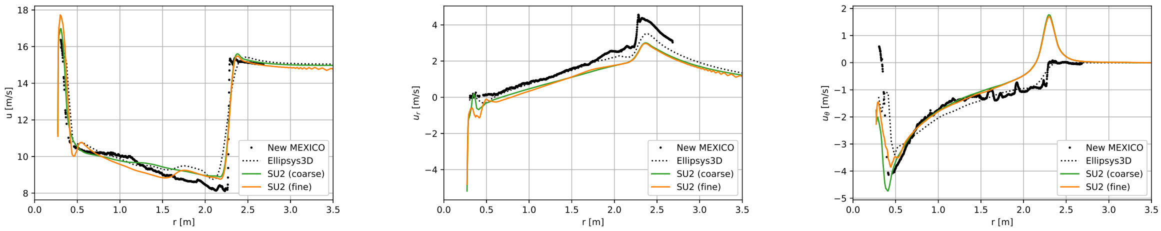

(a) Axial velocity component (b) Radial velocity component (c) Tangential velocity component

Figure 4.13: Radial velocity traverse downstream of the rotor at $x = 0.3\,\text{m}$

Azimuthal velocity traverse Azimuthal velocity traverses are computed based on velocities from the yz-planes at $x = -0.3\,\text{m}$ and $x = 0.3\,\text{m}$. The velocity traverses are computed for the radial locations corresponding to $r = 0.25$, 0.35, 0.60, 0.82 and 0.92 m. The periodic boundaries were located at 90° and the blade passage was at a rotor azimuth angle of 30°. The azimuthal velocity traverses corresponding to $r = 0.35\,\text{m}$ and $r = 0.92\,\text{m}$ are presented and discussed here. To give a complete overview, the azimuthal velocity traverses corresponding to $r = 0.25$, 0.35 0.60, 0.82 and 0.92 m are included in Appendix A.

Upstream of the rotor, the predicted azimuthal velocity traverses are mostly in good agreement with the results from the New MEXICO project and Ellipsys. They follow the same trend, but radial components are somewhat underpredicted. At azimuthal angles before the blade passage ($\phi = 30°$), the axial velocity increases (upwash), and at azimuthal angles after the blade passage it decreases (downwash). The blade passage induces a radial and tangential velocity component. Downstream of the rotor, the azimuthal velocity traverses are influenced by the vortices and the wake convected from the blade. Therefore, these velocity traverses are more difficult to predict. This is seen at $r = 0.25\,\text{m}$. The trend is more difficult to follow. Nonetheless, the pressure-based solver generally captures them well. The velocity components are generally in good agreement with especially the numerical results obtained by Ellipsys and also in fine agreement with the experimental data. The experimental data is sometimes at a different velocity level and the trend deviates somewhat. It was observed in IEA Task 29 Phase III that the different CFD codes predicted similar trends, but deviations were observed in the predicted velocity levels. The variation in the prediction of radial and tangential components was attributed to the accuracy of the prediction of the location of the vortices.

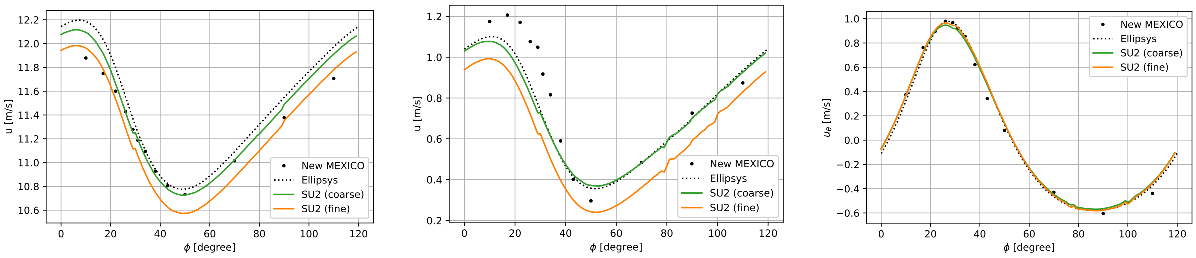

(a) Axial velocity component (b) Radial velocity component (c) Tangential velocity component

Figure 4.14: Comparison azimuthal velocity trace at $x = -0.3\,\text{m}$ and $r = 0.35\,\text{m}$

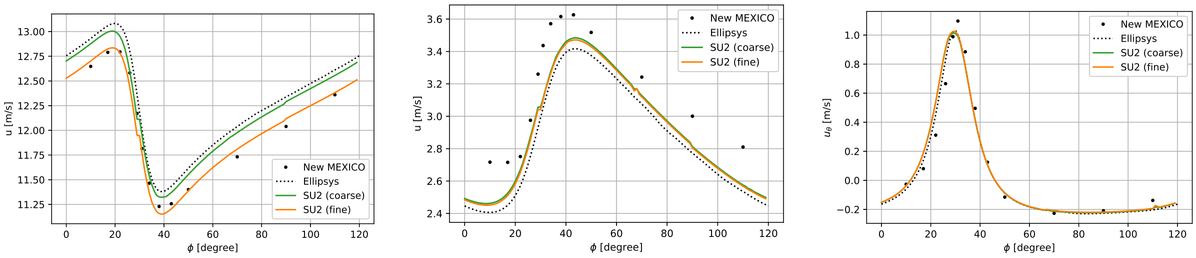

(a) Axial velocity component (b) Radial velocity component (c) Tangential velocity component

Figure 4.15: Comparison azimuthal velocity trace at $x = -0.3\,\text{m}$ and $r = 0.92\,\text{m}$

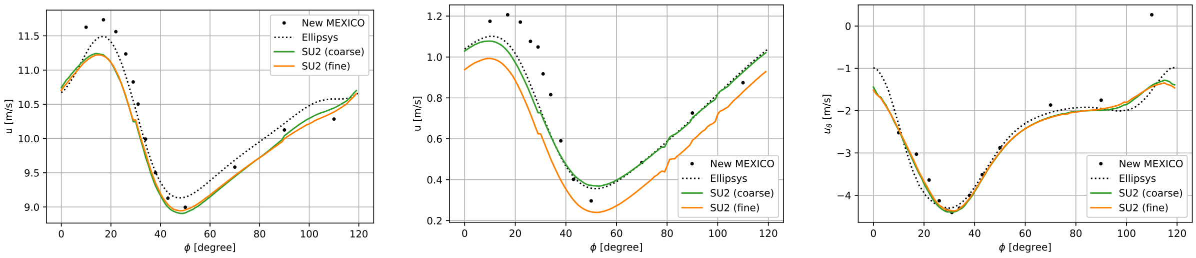

(a) Axial velocity component (b) Radial velocity component (c) Tangential velocity component

Figure 4.16: Comparison azimuthal velocity trace at $x = 0.3\,\text{m}$ and $r = 0.35\,\text{m}$

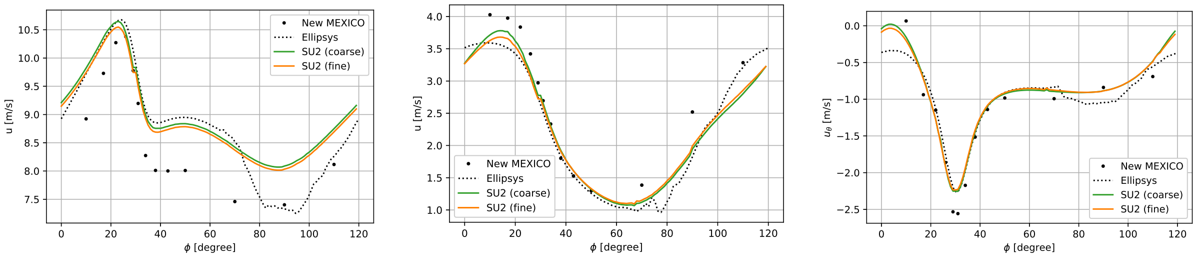

(a) Axial velocity component (b) Radial velocity component (c) Tangential velocity component

Figure 4.17: Comparison azimuthal velocity trace at $x = 0.3\,\text{m}$ and $r = 0.92\,\text{m}$

4.1.3 Numerical challenges

Simulation of the design condition on the fine mesh

The simulation of the MEXICO rotor was performed on a coarse as well as on a fine grid. Section 4.1.2 discussed the results for both grids. In the radial velocity traverses, Figures 4.12 and 4.13, unphysical wiggles were observed. The velocity field in Figure 4.18 also shows unexpected velocity variations and it is not correctly converged. The velocity field shows a wave-like variation of velocity contours. This suggests an undesired interaction between the flow and the outer boundary at the surface of the cylinder.

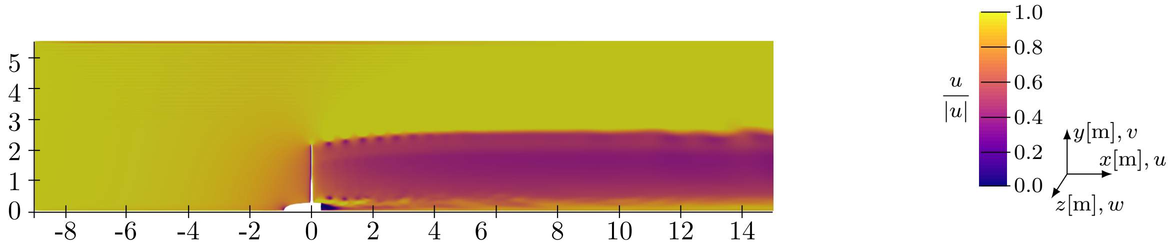

Figure 4.18: Velocity contours of the u-component extracted from the fine mesh

Turbulent wake state

The pressure distribution and PIV measurements were performed in the New MEXICO project in the previously discussed design condition as well as in the turbulent wake state ($a > 0.5$) where the inflow velocity was $U = 10\,\mathrm{m\,s^{-1}}$ [24]. A turbulent wake develops when the shear layer separating the flow in the wake and outside the wake becomes unstable. This occurs in conditions with high rotor thrusts. High rotor thrusts are associated with low wake velocities and high shear. For high rotor loads, a lot of the kinetic energy from the wind is converted into large scale turbulent motion. This leads to a turbulent wake state. Low velocity fluid in the wake mixes with high velocity fluid outside the wake in which way momentum is transferred into the wake. This leads to wake expansion and a reduction of the velocity deficit, but also to an unstable shear layer and turbulent wake [55]. The turbulent wake state is more difficult to model than the design condition. It was also found that the results scatter more around the experimental values [30].

In this study, the turbulent wake state of the MEXICO rotor is simulated. The rotor operated under the conditions given in Table 4.1a, but with a inflow velocity of $U = 10\,\mathrm{m\,s^{-1}}$. The coarse mesh was used. The simulation was restarted from the results for the design condition. No convergence was obtained using the MUSCL scheme, but only using a first-order scheme which has a lot of numerical dissipation. The presented results should therefore only be considered as a first indication. The challenge in obtaining convergence may relate to the complexity around the hub or the difficulty in predicting off-design conditions.

Pressure distribution The first-order predicted pressure distribution is presented in Figure 4.19. The predicted pressure distribution shows a comparable main trend to the other numerical results as well as to the experimental data at $r/R = 0.92$. However, pressure levels are incorrectly predicted due to numerical dissipation.

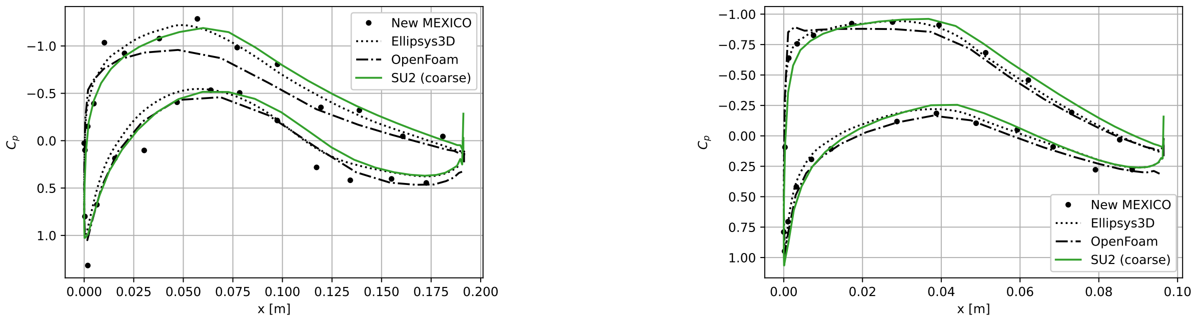

(a) $r/R = 0.35$

(b) $r/R = 0.92$

Figure 4.19: Pressure distributions at two radial locations comparing experimental data and numerical results

Velocity field The velocity field around the rotor in Figure 4.20 illustrates the limitation of a first-order scheme. A first-order scheme induces considerable numerical dissipation. In comparison against the velocity field predicted for the design condition, Figure 4.9, the first-order velocity field for the turbulent wake state is simpler and more uniform. Tip and root vortices are not predicted. Typical for a turbulent wake state, it is found however, that the velocities in the wake are lower, there is a larger difference between the velocities in the wake and outside the wake.

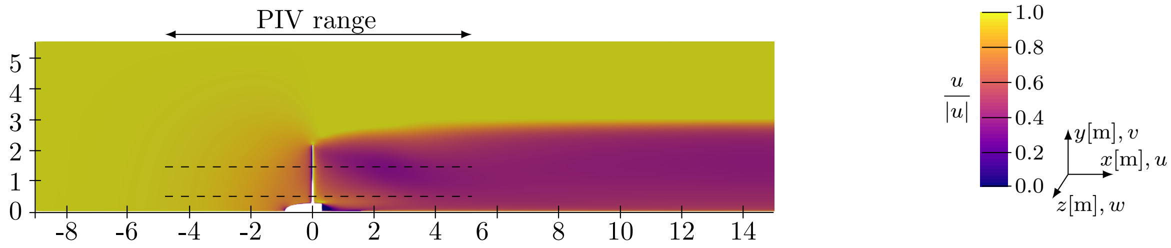

Figure 4.20: Axial velocity contour of the u-component

4.2 DanAero

A series of field measurements were performed at modern MW wind turbines in the DanAero project [56, 25]. The DanAero project, short for 'Experimental Rotor and Airfoil Aerodynamics on MW Wind Turbines', was performed by the Danish Technical University (DTU) and 4 industrial partners (LM Glassfiber, Siemens WindPower, Vestas and Dong Energy). During the DanAero measurement campaign, along with others, field measurements in different inflow and operation conditions were conducted at the NM80 2 MW wind turbine sited at the Tjæreborg wind farm. One of the blades was instrumented to measure the pressure distributions at four radial locations as well as the inflow at five radial locations. The measurement setup and a schematic of the instrumented blade are shown in Figure 4.21. The measurement data used in this study corresponds to the NM80 2 MW wind turbine rotor operating in more or less axial inflow and constant operating conditions.

The NM80 2 MW wind turbine is a three-bladed rotor with blades of the type LM38.8, a rotor diameter of 80 m and a hub height of 59.9 m. This study focuses on the NM80 2 MW wind turbine operating in a wind speed of 6.1 m s^{-1} and rotating with a rotational velocity of 12.3 rpm. This yields a tip speed ratio of 8.4. Two different pitch angles are considered: $\theta_p = 0.17°$ and $\theta_p = 3.0°$. The former case corresponds to the first simulation round in axial inflow of IEA Task 39 Phase IV [31]. The latter case serves as an initialisation for the study on sheared inflow. The chord and twist distribution at the measurement locations are tabulated in Table 4.3b. The properties of the NM80 rotor and flow conditions together with the properties of the instrumented sections of the LM38.8 blade are given in Table 4.3. Here, the radius r is the radius as seen from the rotor center.

Property	Value
Number of blades	3
Rotor diameter	80 m
Pitch angle	0.17° and 3.0°
Rotor speed	12.3 rpm
Wind speed	6.1 m s^{-1}

(a) Rotor and flow conditions

r	Chord	Twist angle
13.121 m	3.17 m	9.43°
19.064 m	2.60 m	4.44°
30.219 m	1.74 m	1.10°
36.775 m	1.23 m	0.08°

(b) Properties of the spanwise sections

Table 4.3: Description of the rotor of the NM80 2 MW wind turbine

4.2.1 Numerical method

The flow over the rotor of the NM80 turbine was simulated in combination with the SA turbulence model. Viscous fluxes were discretized on a central scheme and convective fluxes were discretized on an upwinding scheme. The MSUCL scheme was applied with the Van Albada Edge limiter. The spatial

(a) NM80 turbine with test blade (b) Sketch of the measurement setup at a LM38.8 blade

Figure 4.21: Measurement setup [56]

gradients were evaluated using Green-Gauss and the linear system of algebraic equations was solved using FGMRES in combination with ILU preconditioning. The flow was simulated in rotating reference frame with a constant angular velocity of $1.29\,\mathrm{rad\,s^{-1}}$ in the streamwise direction around the centre of the rotor without any intermediate stages. An initialisation run was performed using a first order scheme before the flow was approximated on a second order scheme. The CFL number was set at 0.5 and stepwise increased when allowed by stability. The simulation was run until convergence was obtained for the loads on the blades, i.e. the pressure and skin friction coefficient distribution reached a steady state.

The simulations were performed on a cylindrical domain. The computational domain around the DanAero rotor operating under a pitch angle of 0.17° is shown in Figure 4.22a. The domain ranges from $4D$ upstream to $6D$ downstream of the rotor and has a radius of $8D$. The cylindrical domain for $\theta_p = 3.0°$ is shown in Figure 4.22b. It ranges from $4.25D$ upstream of the rotor to $7.32D$ downstream of the rotor. The cylinder has a radius of $4.75D$. All three bended blades were modelled without the hub to allow the domain to be used in a future study on non-periodic flows. The blades were modelled by the no-slip wall boundary condition. At the inlet, a velocity of $6.1\,\mathrm{m\,s^{-1}}$ was prescribed in the streamwise direction. The outlet and sides were modelled using a pressure outlet boundary condition.

The surface mesh was provided by the Frauenhofer institute and the full mesh was thereafter generated using the commercial package PointWise. The surface mesh had 256 nodes along the chord and 144 nodes along the span of the rotor. The height of the first cell was $8 \times 10^{-7}\,\mathrm{m}$ such that $y^+ < 1$ was maintained on the surface. The surface mesh consisted of 110.592 quadrilateral cells. The mesh around the rotor operating under a pitch angle of 0.17° contained a total of 38×10^6 cells and the mesh around the rotor operating under a pitch angle of 3.0° contained a total number of 40.6×10^6 cells.

4.2.2 Results

The results obtained from the simulation of the NM80 rotor in axial inflow operating under a pitch angle of 3.0° and 0.17° are discussed in this section. Experimental values from the DanAero project are available to validate the 0.17° results. Boorsma et al. also presented numerical results [32] and the first round as a part of an IEA Task is documented [31]. The sectional geometries are compared first. Thereafter, the loads on the rotor are validated. The predicted velocity field is considered for a fidelity check.

Sectional geometry

The sectional geometries used in this study should be the same as the sectional geometries of the experimental NM80 rotor used in the DanAero project at Tjæreborg wind farm and the same as the sectional

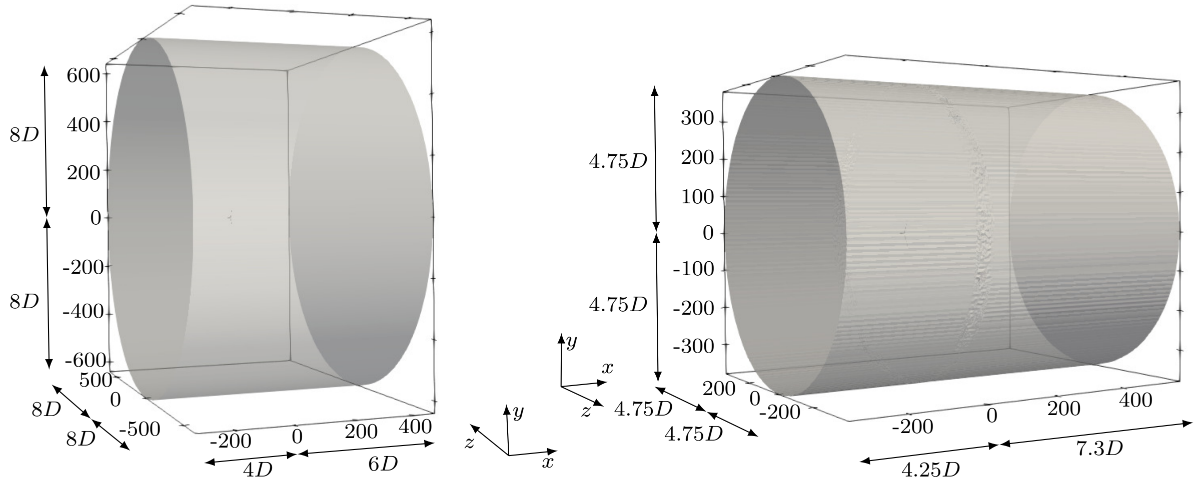

(a) Cylindrical domain for $\theta_p = 0.17°$ (b) Cylindrical domain for $\theta_p = 3.0°$

Figure 4.22: Computational domain

geometries used in other numerical studies. Figure 4.23 shows the sectional geometries at $r = 13.12\,\text{m}$ and at $r = 36.78\,\text{m}$ for the experimental LM38.8 blade and for the mesh used in this study. There is some deviation, but the deviation is generally similar to the deviation corresponding to the numerical results of other codes [32]. The geometry to which the numerical results corresponds is correct.

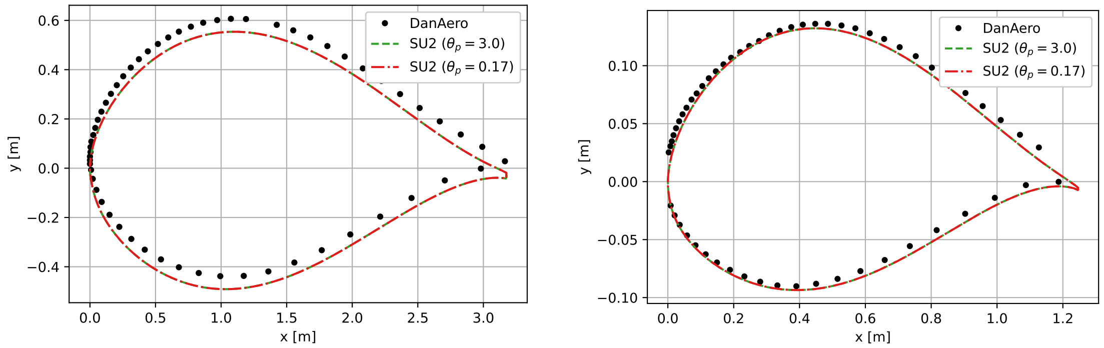

(a) $r = 13.12\,\text{m}$ (b) $r = 36.78\,\text{m}$

Figure 4.23: Comparison of sectional geometries

Loads

Pressure distribution The pressure contours on the surface of the suction side and pressure side for $\theta_p = 0.17°$ are shown in Figure 4.24 and for $\theta_p = 3.0°$ are shown in Figure 4.25. The pressure contours at the dashed locations are compared to experimental data from the DanAero project. The experimental data corresponds to the case 0.17°. The comparison is shown in Figure 4.26 for $r = 13.12\,\text{m}$, 19.06 m, 30.22 m and 36.78 m. Both Figures 4.24, 4.25 and 4.26 show that pressure levels are higher when the NM80 rotor operates under a pitch angle of 0.17° than under a pitch angle of 3.0°.

The pressure distribution corresponding to $\theta_p = 0.17°$ is validated against measurement data at $r = 13.12\,\text{m}$, 19.06 m, 30.22 m and 36.78 m. These are the locations at the dashed lines in the pressure contour figures. The comparison against measurement is given in Figure 4.26. The numerical pressure distribution and experimental pressure distribution generally have the same shape although its a bit deviating at the $r = 13.12\,\text{m}$ just before the trailing edge. The numerical suction pressure levels are somewhat higher than the experimental suction pressures. This is corresponding to the results obtained

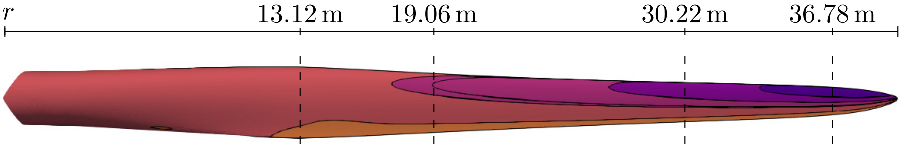

(a) Suction side

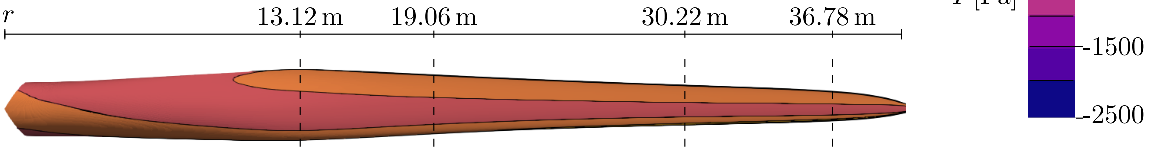

(b) Pressure side

Figure 4.24: Pressure distribution at the surface of the NM80 at $\theta_P = 0.17°$

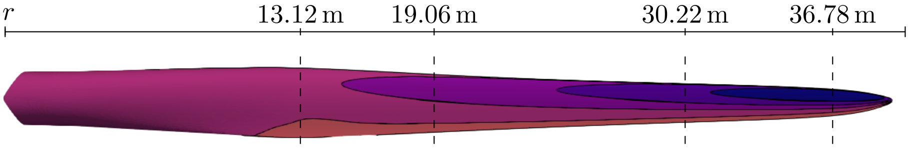

(a) Suction side

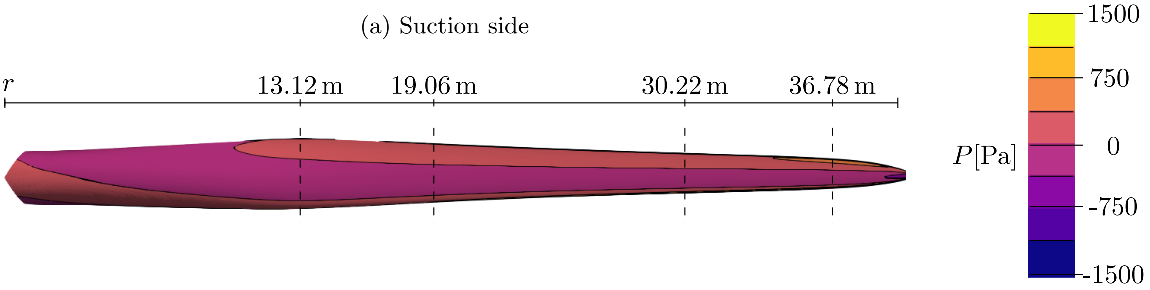

(b) Pressure side

Figure 4.25: Pressure distribution at the surface of the NM80 at $\theta_P = 3.0°$

in the comparison exercise part of IEA Task 39 Phase IV [31]. The shape of the numerical pressure distribution at $r = 36.78\,\mathrm{m}$ on the suction side near the leading edge misses the suction peak which is observed in the experimental pressure distribution. The pressure levels on the pressure side are slightly overpredicted between mid-chord and the trailing edge of the blade. The general agreement between the experimental data and the IEA Task data is good.

Shear stress distribution The shear stress distribution in terms of the normalized skin friction coefficient referenced against free-stream velocity is shown in Figure 4.27 and 4.28. Again, the dashed lines indicate the pressure measurement locations. The streamlines were obtained with ParaView's Surface Line Integration Convolution (LIC) method. The flow separates from the suction side of the blade between $r = 0$ and 16 m. The flow remains attached for radial locations further towards the tip.

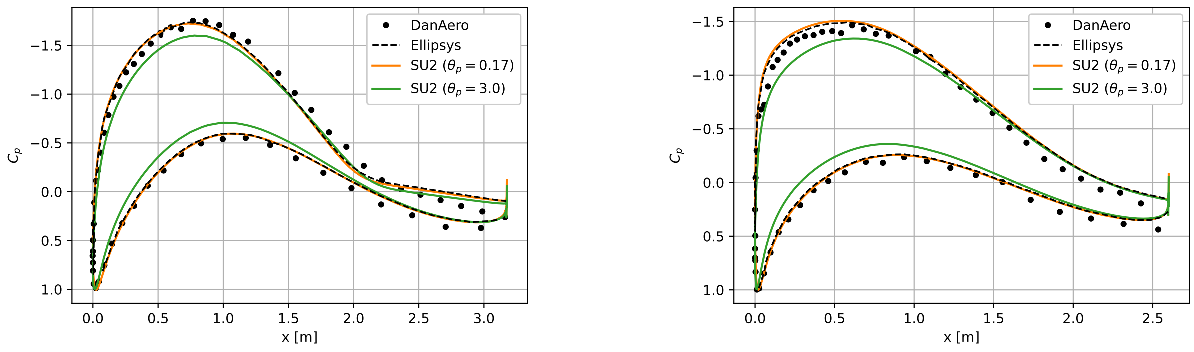

(a) $r = 13.12\,\mathrm{m}$ (b) $r = 19.06\,\mathrm{m}$

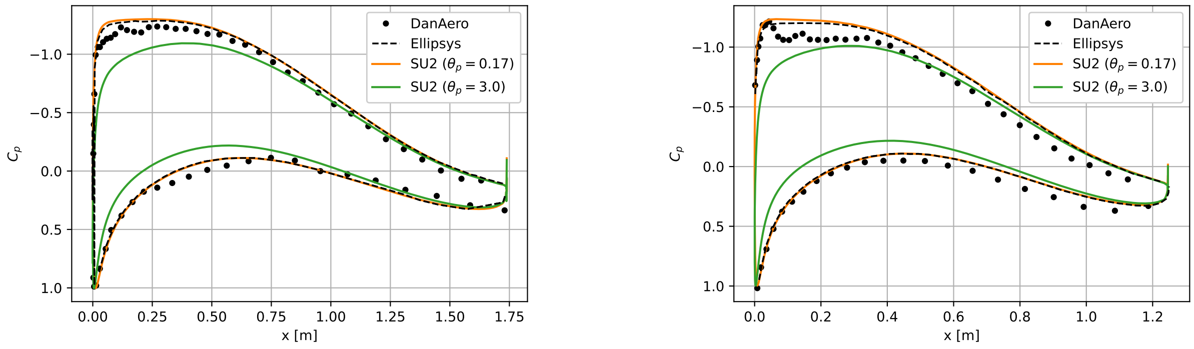

(c) $r = 30.20\,\mathrm{m}$ (d) $r = 36.78\,\mathrm{m}$

Figure 4.26: Pressure distributions at five radial locations comparing experimental data to the pressure-based solvers results for a pitch angle of 0.17° and 3.0°

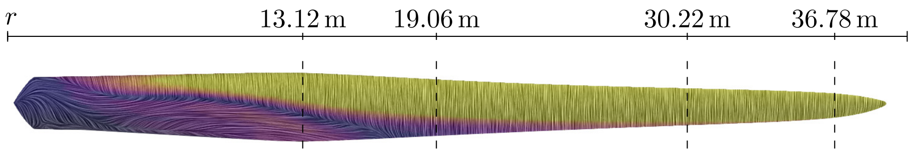

(a) Suction side

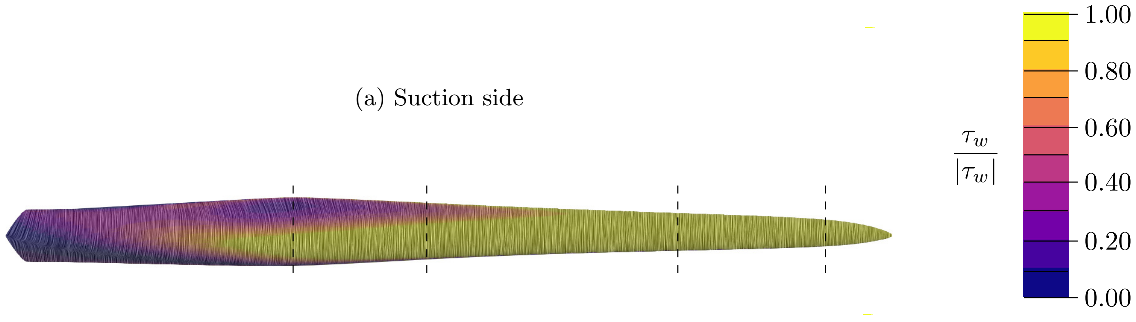

(b) Pressure side

Figure 4.27: Shear stress distribution and streamlines at the surface of the NM80 at $\theta_P = 0.17°$

The magnitude of the skin friction coefficient which is scaled with the local relative inflow velocity is plot in Figure 4.29. The streamlines in Figures 4.27 and 4.28 showed flow separation up to $r = 16\,\mathrm{m}$. The plot corresponding to $r = 13.12\,\mathrm{m}$ also shows flow separation on the suction side between $x = 2\,\mathrm{m}$ and towards the trailing edge of the blade. Flow separation is indicated by the change in sign. The skin friction has a round shape at $r = 13.12\,\mathrm{m}$ but somewhat a peak at the others, especially for $\theta_p = 0.17°$.

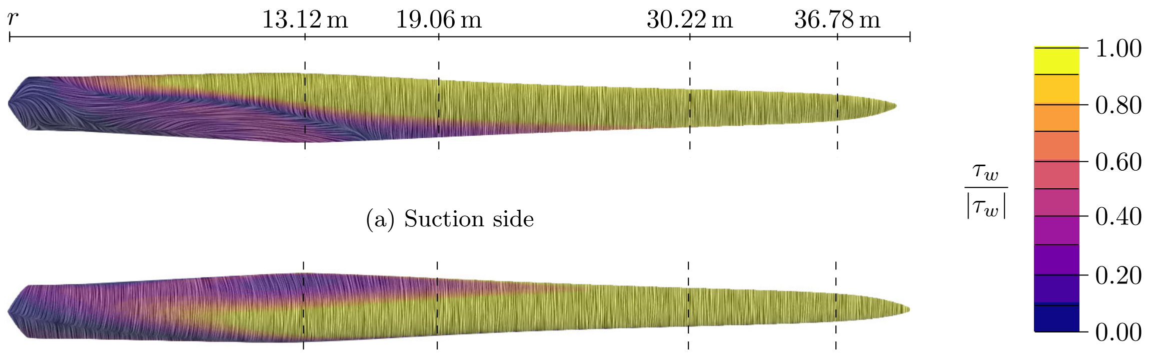

(a) Suction side

(b) Pressure side

Figure 4.28: Shear stress distribution and streamlines at the surface of the NM80 at $\theta_P = 3.0°$

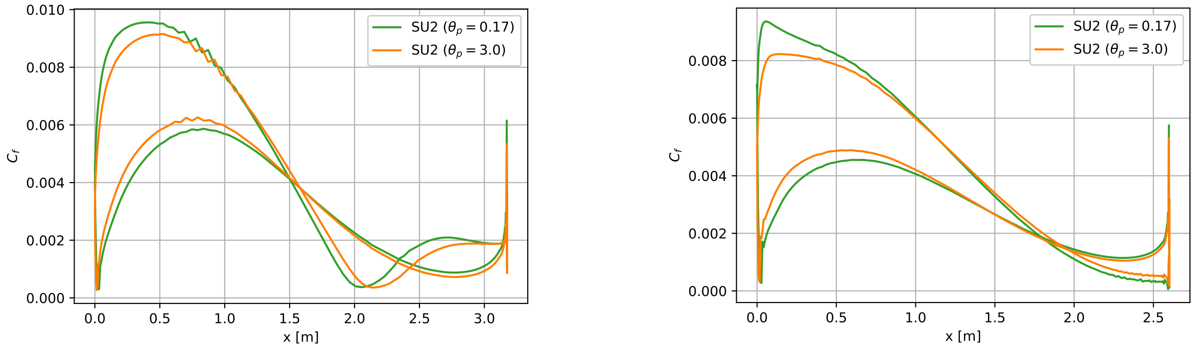

(a) $r = 13.12\,\text{m}$

(b) $r = 19.06\,\text{m}$

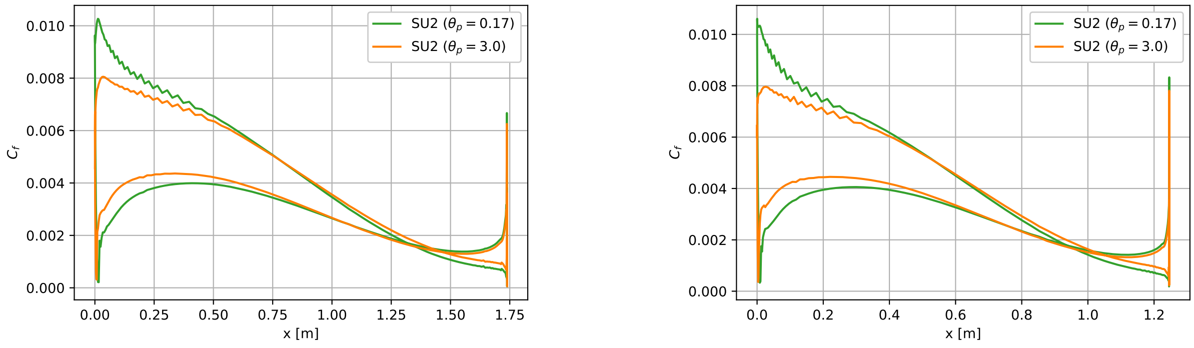

(c) $r = 30.20\,\text{m}$

(d) $r = 36.78\,\text{m}$

Figure 4.29: Skin friction coefficient distributions at four radial locations obtained using the pressure-based solver for a pitch angle of 0.17° and 3.0°

Normal and tangential force The normal and tangential force are computed with respect to the local chord. The experimental values are based on pressure measurements only. Therefore, the normal and tangential forces are computed based only on the pressure distribution as well. They are computed for 13 sections of the blade and shown in Figure 4.30. Here, the solid lines indicated the only-pressure computation and the dashed lines include friction. Differences in the pressure and friction distribution can be amplified in the integrated forces. Pressures were overpredicted and accordingly are the normal forces. The normal forces are overpredicted except at $r = 13\,\text{m}$, and tangential forces are almost constantly underpredicted. This is an unexpected contradiction. It is pointed out in [31] that the experimental tangential force values are very sensitive to the distribution of pressure taps. Friction reduces the tangential force with 22 % for $\theta_p = 3.0°$ and with 11 % for $\theta_p = 0.17°$ whereas the IEA Task participants found a reduction of 15 %. The rotor operating under a pitch angle of 0.17° yields higher normal forces and tangential forces than the operation under a pitch angle of 3.0°.

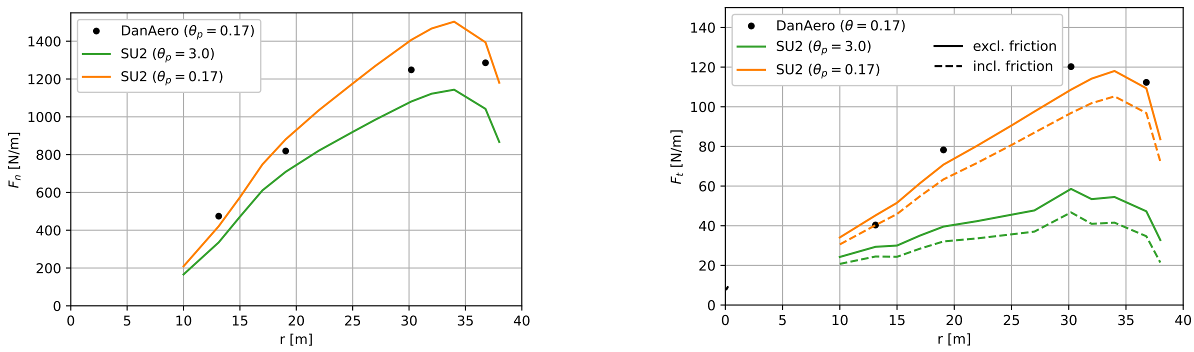

(a) Normal force (b) Tangential force

Figure 4.30: Normal and tangential force on the LM38.8 blade

Velocity field

The velocity field around the rotor and in the wake is considered in this section. The predicted flow is a pre-liminary result because the velocity field is not completely converged. Therefore, this section is limited to a focus on the fidelity of the velocity field. Normalized velocity contours in the predicted velocity field in the xy-plane are shown in Figure 4.31. The flow propagates towards the rotor at free-stream conditions. The streamwise component slows down just upstream of the rotor, where v- and w-component are induced. The interaction of the flow and the rotor creates a wake in which tip vortices and structures near the root form. These phenomena are observed more strongly for $\theta_p = 0.17°$ than for $3.0°$ which is in correspondence with the higher loads on the blade.

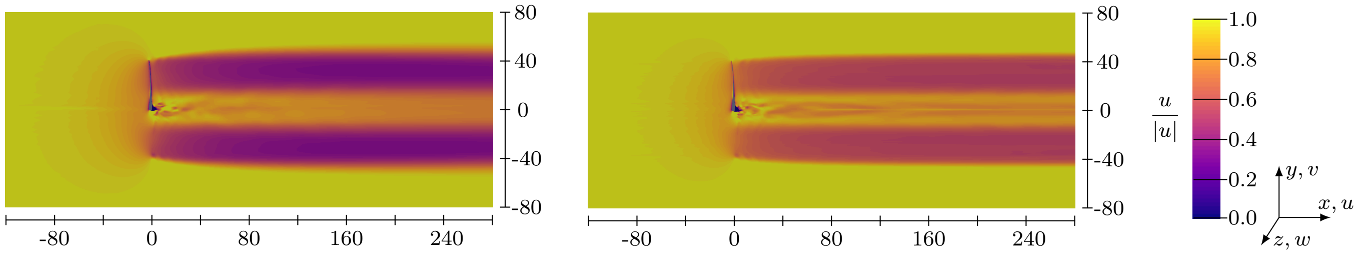

(a) u-component, $\theta_p = 0.17°$

(b) u-component, $\theta_p = 3.0°$

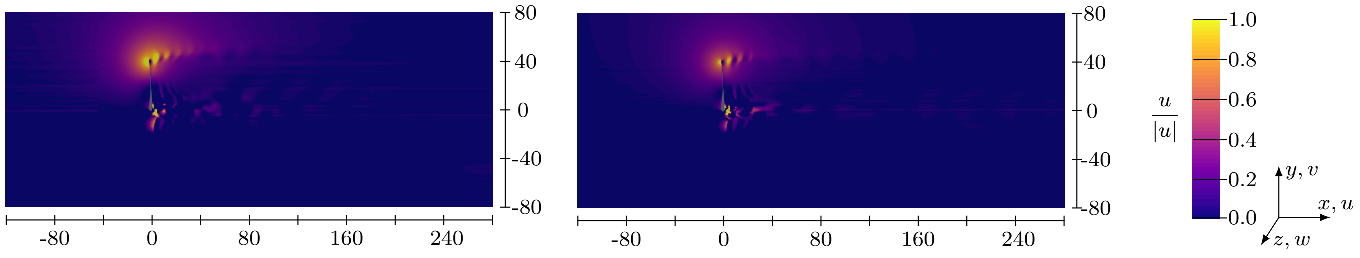

(c) v-component, $\theta_p = 0.17°$

(d) v-component, $\theta_p = 3.0°$

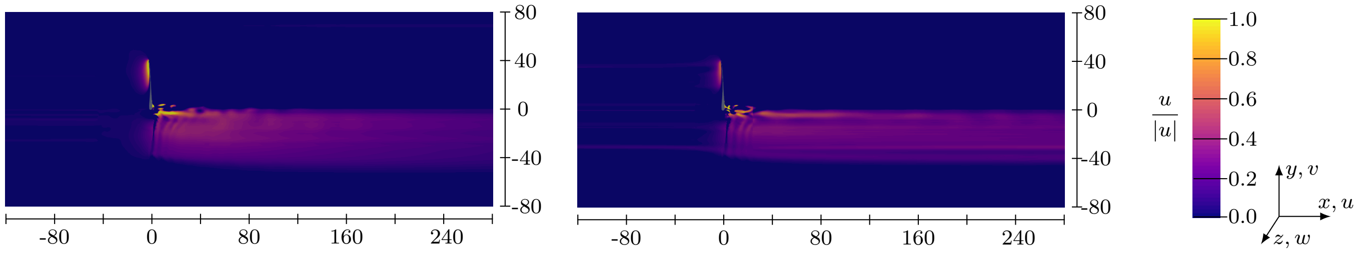

(e) w-component, $\theta_p = 0.17°$

(f) w-component, $\theta_p = 3.0°$

Figure 4.31: Velocity field in the plane normal to the z-axis

Axial velocity traverse The axial velocity traverses at $r = 13.12$, 19.06, 30.22 and 36.78 m are shown in Figure 4.32 for the DanAero rotor operating under a pitch angle of 0.17° and 3.0°. Upstream of the rotor, the velocity is very comparable to the prescribed velocity. The flow slows down and expands just before the rotor. A comparison of the axial velocity component downstream of the rotor shows that the rotor slows down the wind more when operating under a pitch angle of 0.17° than under a pitch angle of 3.0°. The fluctuations downstream might originate from root vortices, tip vortices or the wake convected from the blade as well as being due to the flow field not being fully converged.

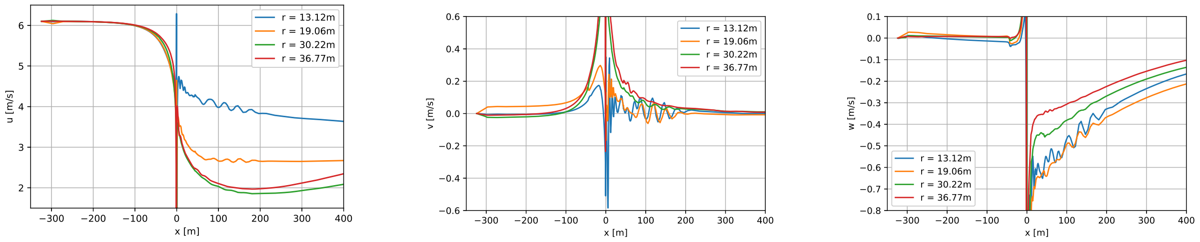

(a) u-component, $\theta_p = 0.17°$ (b) u_r-component, $\theta_p = 0.17°$ (c) u_θ-component, $\theta_p = 0.17°$

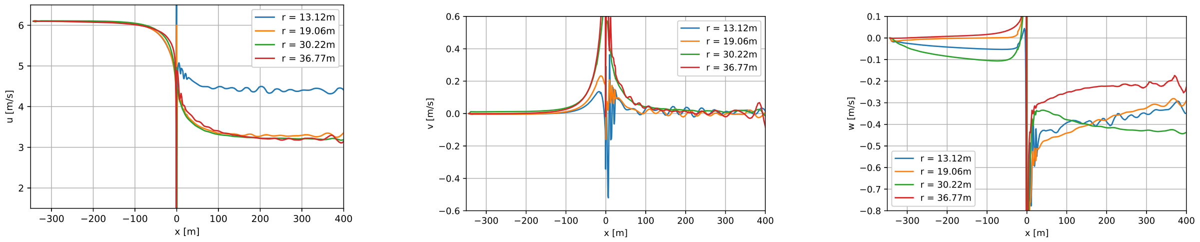

(d) u-component, $\theta_p = 3.0°$ (e) u_r-component, $\theta_p = 3.0°$ (f) u_θ-component, $\theta_p = 3.0°$

Figure 4.32: Axial velocity traverses obtained from the plane normal to z-axis

Radial velocity traverse The radial velocity traverses extracted from radial slices at 5 and 10 m upstream and downstream of the rotor and azimuthally averaged. In Figure 4.33, the radial velocity traverses are shown for the axial, radial and tangential velocity components. The axial velocity reduces as the approaches the rotor and is significantly decreased downstream of the rotor especially for $\theta_p = 0.17°$. Upstream of the rotor the radial velocity u_r shows the 'streamtube' expansion increases between 10 m and 5 m whereas almost no tangential velocity is predicted. This is contradicting to the predicted radial traverses around the MEXICO rotor where the pressure-based solver, in contrary to the measurement, predicted small tangential velocities. Downstream of the rotor, velocity fluctuations are observed especially near the root of the blade for all velocity components and both simulations. In this region, it was difficult to obtain convergence.

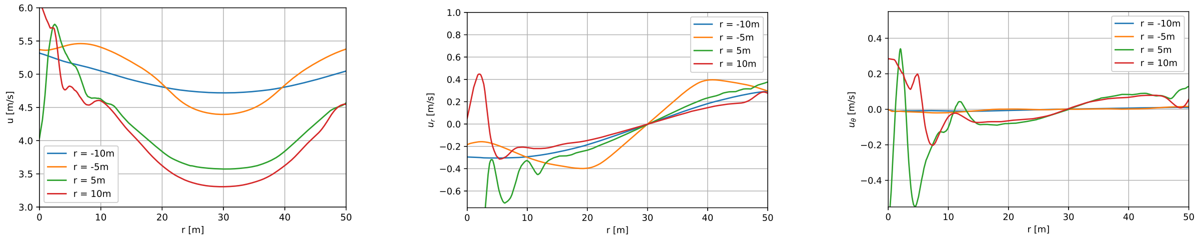

(a) u-component, $\theta = 0.17°$ (b) u_r-component, $\theta = 0.17°$ (c) u_θ-component, $\theta = 0.17°$

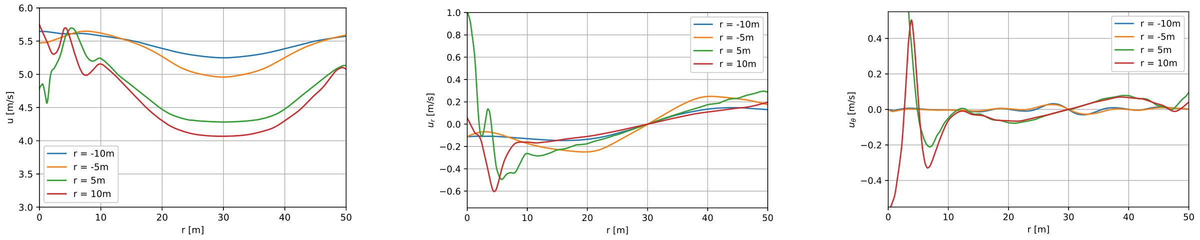

(d) u-component, $\theta = 3.0°$ (e) u_r-component, $\theta = 3.0°$ (f) u_θ-component, $\theta = 3.0°$

Figure 4.33: Radial velocity traverses

Azimuthal velocity traverse The azimuthal velocity traverses are shown in Figures 4.34 and 4.35 at 10 m upstream and downstream of the rotor. The blade passages are at $\phi = 0°$, $120°$ and $240°$. The upstream axial velocity components show an increase in velocity just before blade passage and a decrease behind the blade. This is most pronounced near the tip and the least near the root. The trend in the radial velocities are dependent on the radial location and velocity levels increase from the root towards the tip. At $r = 30\,\text{m}$ the radial velocity is most constant. The tangential velocity component are induced by the blade passage. Downstream of the rotor, the flow has slowed down and the velocity levels are reduced. They are lowest midchord and near the tip, especially at $\theta_p = 0.17°$. The downstream flow is affected by the convected wake. The negative tangential velocities indicates that the flow rotates in opposite motion as the rotor. Both upstream and downstream, the azimuthal traverses show periodic symmetry. This verifies the assumption to model axial flow conditions on one-third of the domain.

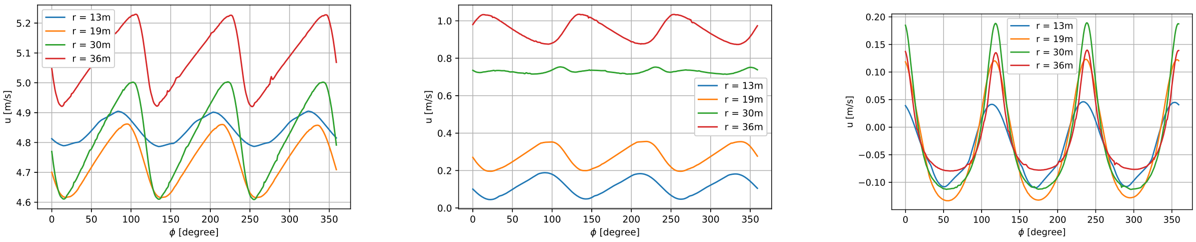

(a) u-component, $\theta_p = 0.17°$ (b) u_r-component, $\theta_p = 0.17°$ (c) u_θ-component, $\theta_p = 0.17°$

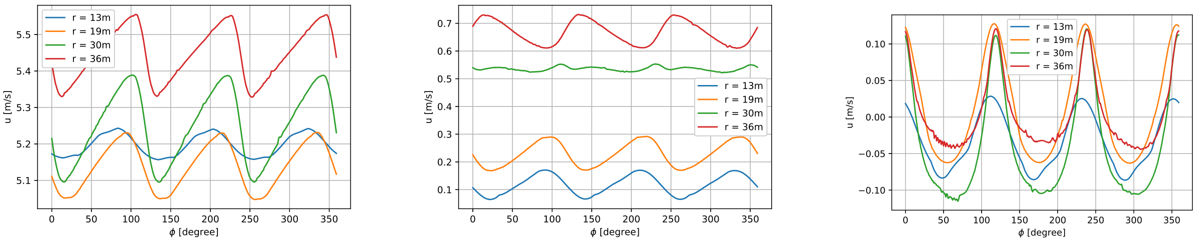

(d) u-component, $\theta_p = 3.0°$ (e) u_r-component, $\theta_p = 3.0°$ (f) u_θ-component, $\theta_p = 3.0°$

Figure 4.34: Azimuthal velocity traces upstream of the rotor at $x = -10\,\text{m}$

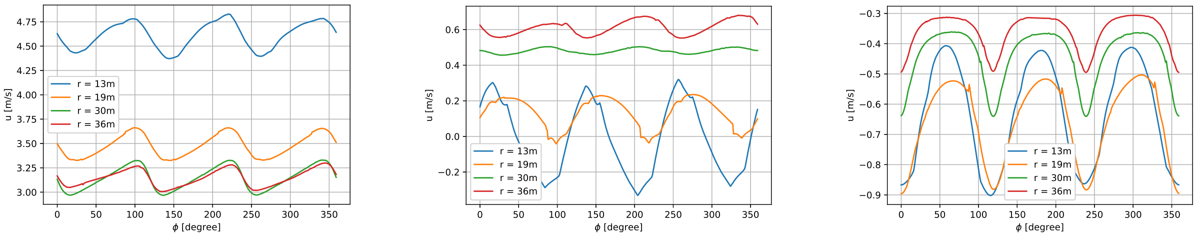

(a) u-component, $\theta_p = 0.17°$ (b) u_r-component, $\theta_p = 0.17°$ (c) u_θ-component, $\theta_p = 0.17°$

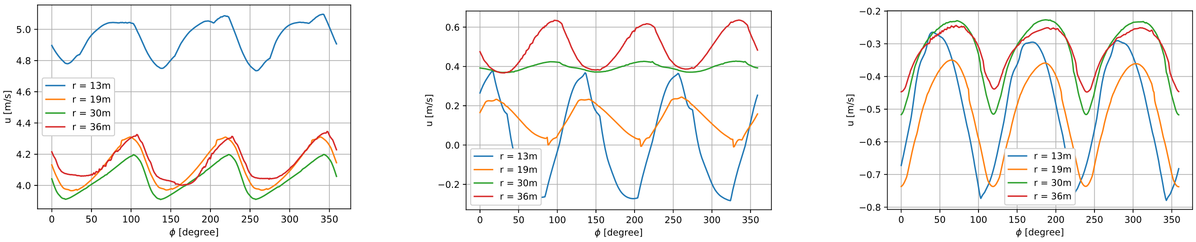

(d) u-component, $\theta_p = 3.0°$ (e) u_r-component, $\theta_p = 3.0°$ (f) u_θ-component, $\theta_p = 3.0°$

Figure 4.35: Azimuthal velocity traces downstream of the rotor at $x = 10\,\text{m}$

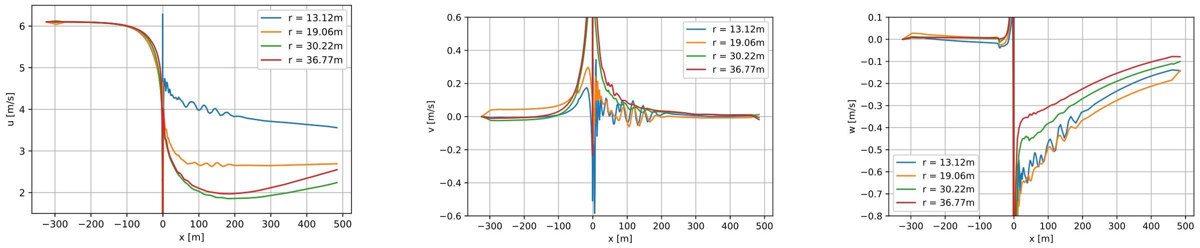

(a) u-component, $\theta_p = 0.17°$ (b) u_r-component, $\theta_p = 0.17°$ (c) u_θ-component, $\theta_p = 0.17°$

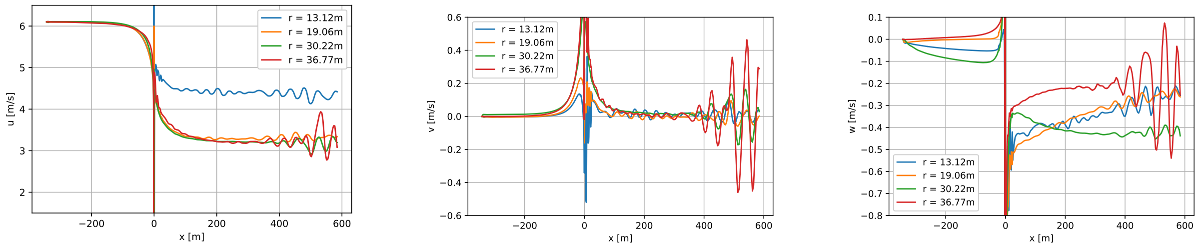

(d) u-component, $\theta_p = 3.0°$ (e) v-component, $\theta_p = 3.0°$ (f) w-component, $\theta_p = 3.0°$

Figure 4.36: Axial velocity traverses obtained from the plane normal to z-axis

4.2.3 Numerical challenges

Axial velocity traverse

The axial velocity traverses for the entire streamwise domain at four radial locations are shown in Figure 4.36. The outgoing flow is expected to be developed and without oscillations. The velocity field for the case $\theta_p = 3.0°$ shows unphysical oscillations at the outlet of the domain. This suggests for an interaction of the flow and the outlet boundary. The flow is not as developed as required for the underlying assumption in the boundary condition. These oscillations are not observed for the case $\theta_p = 0.17°$. The difference in velocity oscillations may partially be an effect of the size of the computational domain/mesh.

Rectangular mesh

The simulation of the DanAero rotor was additionally run on a rectangular mesh. The rectangular mesh was considered to take into account possible ground effects. The experimental data of the DanAero project is based on field measurements of the NM80 2 MW rotor with a hub height of 59.9 m but are modelled at a hub height of 100 m. The use of a cylindrical mesh yields velocities at spatial locations below ground levels. This problem might be overcome on a rectangular mesh. In this subsubsection, the results of simulations of the DanAero rotor operating under a pitch angle of 3.0° using a rectangular mesh are discussed.

Numerical method The computational domain of the rectangular mesh is shown in Figure 4.37. It extends from $5D$ upstream to $10D$ downstream in the streamwise direction. It ranges from the ground ($y = -100\,\mathrm{m}$) to $5D$ in height and has a width of $5D$. Three pre-bend blades are modelled and the hub is ignored. The blades are modelled by a no-slip wall boundary condition and the ground by a slip wall boundary condition. The top and outlet are specified pressure outlets. Two different inflow conditions are considered at the inlet: i) farfield boundary condition; ii) prescribed velocity inlet; and four different boundary conditions are considered at the sides of the rectangular domain: i) translational periodic boundary condition; ii) specified pressure outlet; iii) farfield boundary condition; iv) symmetry boundary conditions. The surface mesh is the same surface mesh as was used in the cylindrical domain. The minimum cell height is m and the mesh contained 1.5×10^5 'tris' and 1.5×10^6 'quads'. For each simulation, 25 000 iterations were performed at an angular velocity of $0.03\,\mathrm{rad\,s^{-1}}$ and a CFL of 0.01.

Results The two inlet boundary conditions give a different inflow velocity profile. The farfield boundary condition and specified velocity inlet are compared upstream of the rotor in Figure 4.38. This figure shows the axial traverse of the normalized axial velocity component. It is seen that prescribing a velocity using the farfield boundary condition results in an oscillation in the velocity field. This is unphysical and

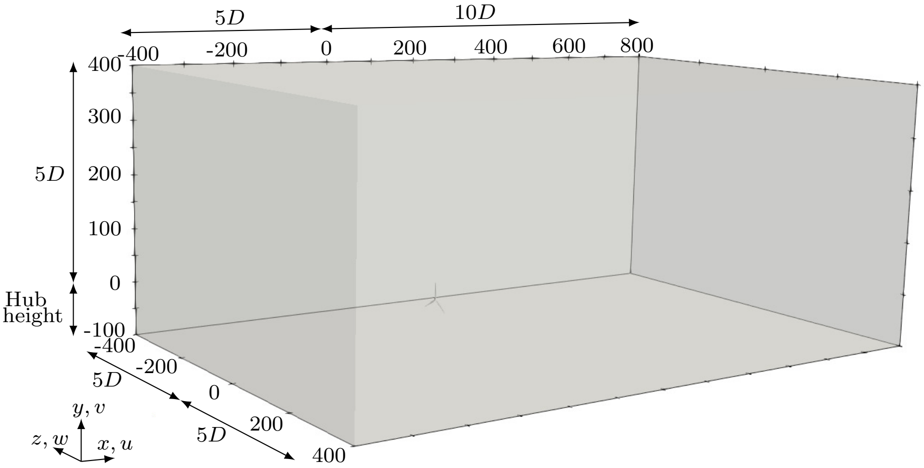

Figure 4.37: Computational domain of the rectangular mesh

undesired, and caused by the farfield boundary condition prescribing a gradient. The specified velocity inlet prescribes a direct value (Dirichlet) and the velocity remains constantly equal to its prescribed value. The specified velocity inlet yields a physical result. It is therefore the preferred velocity boundary condition in the subsequent study on the rectangular mesh.

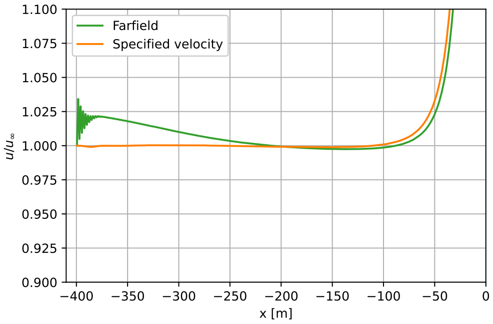

Figure 4.38: Axial velocity upstream of the rotor

The normalized velocity field on the outside surface of the rectangle is shown in Figure 4.39 for four different simulations in which each used a different boundary condition on both sides. The velocity field on the outside surface is expected to show free-stream velocity conditions as the boundaries are far away from the rotor. However, for all simulations, there are several non-yellow spots on the sides, top and outlet surface. The non-yellow regions indicate a different velocity field than the expected velocity field. The boundary conditions that were applied on the sides did not develop towards the expected velocity field. The implementation of the boundary conditions requires further study.

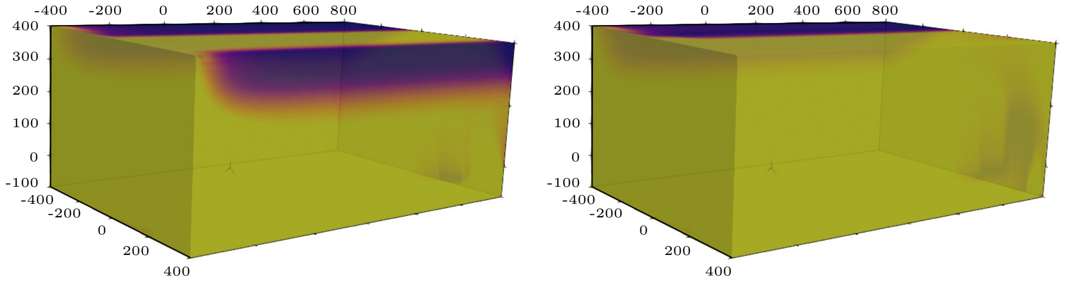

(a) Periodic boundary condition (b) Specified pressure

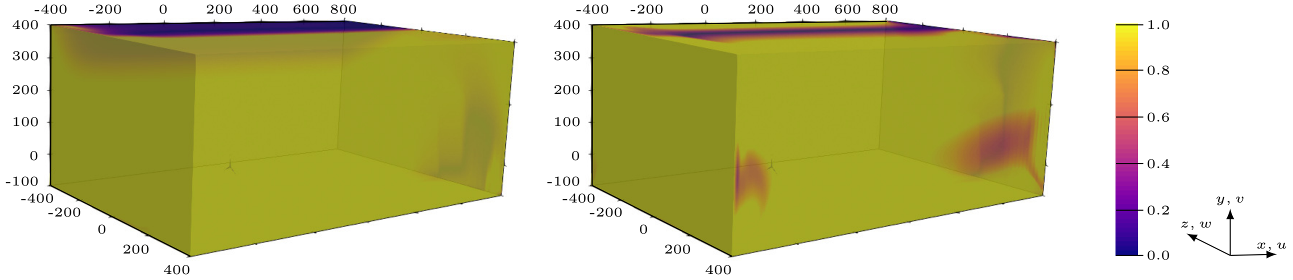

(c) Farfield (d) Symmetry

Figure 4.39: Velocity field using different boundary conditions at the sides

Chapter 5

Conclusions

Contributing to the field of wind turbine aerodynamics and rotor modeling, this study focused on the application of the pressure-based solver in SU2 to simulate the flow over a wind turbine rotor. The pressure-based solver was firstly validated for 2D external flow phenomena. Based on simulation results of the flow over the MEXICO and DanAero rotor in axial inflow conditions and comparison against experimental data and numerical results from other studies, this work showed how well the pressure-based solver captures the 3D flow.

By simulation of a turbulent flow over a flat plate, the pressure-based solver's ability to capture the turbulent boundary layer was demonstrated. From the comparison of the predicted turbulent flow over a backward facing step against experimental and numerical data, it was observed that the pressure-based solver is able to predict the reattachment length and flow reversal after a flow separates at a fixed separation point. The flow reversal was captured better by the SST model. Based on a comparison of lift and drag coefficients as well as the pressure and skin friction distribution, it was found that the pressure-based solver predicts the flow over a NACA0012 airfoil in sufficiently good agreement with experimental data and numerical data for different angles of attack lower than the stall angle. This allows the conclusion that the pressure-based solver is capable of modeling several 2D phenomena that are relevant for external aerodynamics.

The simulation results of the MEXICO rotor operating under design conditions and the DanAero rotor show that the pressure-based solver generally predicts similar pressure trends and levels as other numerical studies. Especially for the DanAero rotor, in comparison against experiment, the pressure levels were somewhat overpredicted on the suction side. While the pressure predictions showed physical results, unphysical wiggles were found in the skin friction coefficients. Although the pressure levels on the suction side were somewhat overpredicted and unphysical wiggles were observed in the skin friction coefficient and despite the deviation in the geometry of the coarse mesh, in general the predicted integrated forces were in agreement with literature. It was found that the DanAero operating under a smaller pitch angle predicted higher loads on the blade.

It was found from the comparison between experimental data of the MEXICO rotor and the velocity traverses that the pressure-based solver is broadly able to predict the velocity field around the rotor and in the near-wake. Where wake expansion was well-predicted, it was found most difficult to predict the velocity field in the vicinity of the root vortex. These findings are consistent with literature. Although the velocity field seemed physical, it is difficult to arrive at any conclusions with regard to the DanAero simulation as the velocity field was not entirely converged. The influence of the dimensions of the computational domain were illustrated by comparison of axial velocity traverses. It was found by comparison of axial velocity traverses that the dimensions of the computational domain influence the presence of oscillations in the velocity field at the outlet of the domain. Based on the azimuthal velocity traverses, the axisymmetry of the flow was confirmed. Consistent with the higher loads on the blade, a larger velocity deficit was predicted for the simulation of the DanAero rotor under a smaller pitch angle.

Additional to the validation of the loads and the velocity field, it was found that the pressure-based solver faces numerical challenges. Despite the validated results, the pressure-based solver's stability requires further work as obtaining convergence required small CFL numbers and intermediate steps for the rotating frame of reference. It was difficult to obtain convergence for the MEXICO rotor operating in the turbulent wake state. The results on the simulation of the MEXICO rotor on the fine mesh and the simulations of the DanAero rotor on the rectangular mesh indicate that the boundary conditions provide a different solution than expected. These problems remain a challenge for further work.

Chapter 6

Recommendations and future work

The current study presents the pressure-based solver's abilities to predict the flow over a wind turbine rotor. While promising results are obtained, the pressure-based solver can profit from some improvements. Additionally, it is interesting to extend the validation study to off-design and non-uniform inflow conditions.

Suggestions for future work are:

- Improve implementation of the boundary conditions - The simulation of the MEXICO rotor on the fine mesh and the DanAero rotor on the rectangular mesh revealed that the boundary conditions may result in an unexpected and unphysical flow field. To obtain a good solution and for ease of application, the implementation of the boundary conditions should be investigated and improved.
- Improve the stability / robustness - The simulation of the MEXICO rotor required to be initialised on intermediate stages with smaller angular velocities before the simulation could be run at the final angular velocity in the rotating frame of reference. Additionally, the simulations required small CFL numbers. Pre-iterations on intermediate stages as well as small CFL numbers slow down convergence. Application of the pressure-based solver will be at lesser computational costs and more attractive when this is improved.
- Extend validation of rotor modelling - Wind turbines often operate in non-uniform inflow conditions under off-design conditions. These are more challenging to predict and associated with more uncertainties. The ability of the pressure-based solver in application to rotor modelling will be more complete when non-uniform inflow conditions and off-design conditions are also considered. The results of the simulation of DanAero rotor under a pitch angle of 3.0° can be used as a starting point to simulate sheared inflow.

Bibliography

[1] IEA. Renewables 2022. Analysis and forecast to 2027, 2022.

[2] Haliade-X offshore wind turbine. (accessed: 10.08.2023).

[3] European Wind Energy Association. *Wind Energy - The Facts: A Guide to the Technology, Economics and Future of Wind Power.* Routledge, first edition, 2009.

[4] M.O.L. Hansen, J.N. Sørensen, S. Voutsinas, N. Sørensen, and H.Aa. Madsen. State of the art in wind turbine aerodynamics and aeroelasticity. *Progress in Aerospace Sciences*, 42(4):285–330, 2006.

[5] H. Snel. Review of aerodynamics for wind turbines. *Wind energy*, 6(3):203–211, 2003.

[6] J.N. Sørensen. Aerodynamics of wind turbines: state of the art and future perspectives, 2022. Lecture series 2022-5.

[7] J. Sumner, C.S. Watters, and C. Masson. CFD in wind energy: the virtual, multiscale wind tunnel. *Energies*, 3:989–1013, 2010.

[8] E. Daniele. CFD for wind turbine simulations. In *Handbook of Wind Energy Aerodynamics.* Springer International Publishing, 2022.

[9] H. Glauert. Airplane propellers. In *Aerodynamic Theory*, pages 169–360. Springer, Berlin, 1935.

[10] J.G. Schepers. *Engineering models in wind energy aerodynamics.* PhD thesis, Technische Universiteit Delft, 2012.

[11] J. Katz and A. Plotkin. *Low-Speed Aerodynamics.* Cambridge University Press, second edition, 2001.

[12] M. Drela. XFOIL: an analysis and design system for low Reynolds number airfoils. In *Low Reynolds number aerodynamics*, pages 1–12. Springer, Berlin, 1989.

[13] R.P.J.O.M. van Rooij. Modification of the boundary layer calculation in RFOIL for improved stall prediction, 1996.

[14] E.P.N. Duque, W. Johnson, C.P. van Dam, R. Cortex, and K. Yee. Numerical predictions of wind turbine power and aerodynamic loads for NREL Phase II combined experiment rotor. AIAA/ASME Wind Energy Symposium AIAA 38th Aerospace Sciences Meeting, 2000. Paper 2000-0038.

[15] N.N. Sørensen and M.O.L. Hansen. Rotor performance predictions using a Navier-Stokes method. AIAA/ASME Wind Energy Symposium, 1998. Paper 98-0025.

[16] J. Varela and D. Bercebal. CFD calculations of the flow around a wind turbine nacelle. Technical Report 910, CIEMAT, Spain, 1999.

[17] D. Kwak, C. Kiris, and C.S. Kim. Computational challenges of viscous incompressible flows. *Computers and Fluids*, 34(3):283–299, 2005.

[18] J.H. Ferziger and M. Perić. *Computational Methods for Fluid Dynamics.* Springer, third edition, 2002.

[19] F. Palacios, M.R. Colonno, A.C. Aranake, A. Campos, S.R. Copeland, T.D. Economon, A.K. Lonkar, T.W. Lukaczyk, T.W.R. Taylor, and J.J. Alonso. Stanford University Unstructured (SU2): an open-source integrated computational environment for multi-physics simulation and design. 51st AIAA Aerospace Sciences Meeting including the New Horizons Forum and Aerospace Exposition, 2013. Paper 2013-0287.

[20] T.D. Economon. Simulation and adjoint-based design for variable density incompressible flows with heat transfer. *AIAA Journal*, 58(2):757–769, 2020.

[21] A. Koodly Ravishankara. *Development of a pressure based incompressible flow solver for wind turbine applications*. PhD thesis, University of Twente, 2021.

[22] M.M. Hand, D.A. Simms, L.J. Fingersh, D.W. Jager, J.R. Cotrell, S. Schreck, and S.M. Larwood. Unsteady Aerodynamics Experiment phase VI: wind tunnel test configurations and available data campaigns. Technical Report TP-500-29955, National Renewable Energy Laboratory, 2001.

[23] H. Snel, J.G. Schepers, and B. Montgomerie. The MEXICO project (Model Experiments in Controlled Conditions): the database and first results of data processing and interpretation. *Journal of Physics: Conference Series*, 75:012014, 2007.

[24] K. Boorsma and J. Schepers. New MEXICO experiment, preliminary overview with initial validation. Technical Report ECN-E-14-048, Energy Research Center of the Netherlands, 2014.

[25] H.Aa. Madsen, C. Bak, U.S. Paulsen, M. Gaunaa, P. Fuglsang, J. Romblad, N.A. Olesen, P. Enevoldsen, J. Laursen, and L. Jensen. The DAN-AERO MW experiments. Final report. Technical Report RISO-R-1726(EN), Technical University of Denmark, 2010.

[26] N. Troldborg, C. Bak, H.Aa. Madsen, and W. R. Skrzypinski. Danaero MW final report. Technical Report E-0027, DTU Wind Energy, 2013.

[27] S. Schreck, C. Masson, J. Johansen, N.N. Sørensen, F. Zahle, C. Bak, H.Aa. Madsen, E. Polities, G. Schepers, K. Lindenburg, H. Snel, R.P.J.O.M. van Rooij, E.A. Arens, G.J.W. van Bussel, G.A.M. van Kuik, F. Meng, T. Sant, A. Knauer, G. Moe, X. Munduate, A. González, E. Ferrer, S. Gomez, G. Barakos, and S. Ivanell. IEA wind annex XX: HAWT aerodynamics and models from wind tunnel measurements. Technical Report NREL/TP-500-43508, National Renewable Energy Laboratory, 2008.

[28] J.G. Schepers, K. Boorsma, T. Cho, S. Gomez-Iradi, A.P. Schaffarczyk, A. Jeromin, W.Z. Shen, T. Lutz, K. Meister, B. Stoevesandt, S. Schrek, D. Micallef, R. Pereira, T. Sandt, H.Aa. Madsen, and N. Sørensen. Final report of IEA Task 29 Mexnext (phase 1): analysis of MEXICO wind tunnel measurements. Technical Report ECN-E-12-004, Energy Research Center of the Netherlands, 2012.

[29] J.G. Schepers, K. Boorsma, S. Gomez-Iradi, A.P. Schaffarczyk, H.Aa. Madsen, N.N. Sørensen, W.Z. Shen, T. Lutz, C. Schulz, I. Herraez, and S. Schreck. Final report of IEA Task 29: Mexnext (phase 2). Technical Report ECN-E-14-060, Energy Research Center of the Netherlands, 2014.

[30] K. Boorsma, J.G. Schepers, S. Gomez-Iradi, I. Herraez, T. Lutz, P. Weihing, L. Oggiano, G. Pirrung, H.Aa. Madsen, W.Z. Shen, H. Rahimi, and A.P. Schaffarczyk. Final report of IEA Task 29 Mexnext (phase 3). Technical Report E-18-003, Energy Research Center of the Netherlands, 2018.

[31] J.G. Schepers, K. Boorsma, H.Aa. Madsen, G.R. Pirrung, G. Bangga, G. Guma, T. Lutz, T. Potentier, C. Braud, E. Guilmineau, A. Croce, S. Cacciola, A.P. Schaffarczyk, B.A. Lobo, S. Ivanell, H. Asmuth, F. Bertagnolio, W.Z. Shen N.N. Sørensen, C. Grinderslev, A.M. Forsting, F. Blondel, P. Bozonnet, R. Boisard, K. Yassin, L. Höning, B. Stoevesandt, M. Imiela, L. Greco, C. Testa, F. Magionesi, G. Vijayakumar, S. Ananthan, M.A. Sprague, E. Branlard, J. Jonkman, M. Carrion, S. Parkinson, and E. Cicirello. Final report of IEA Task 29, phase IV: Detailed aerodynamics of wind turbines. Technical report, Energy Research Center of the Netherlands, 2021.

[32] K. Boorsma, G. Schepers, H.Aa. Madsen, G. Pirrung, N. Sørensen, G. Bangga, M. Imiela, C. Grinderslev, A.M. Forsting, W.Z. Shen, A. Croce, S. Cacciola, A.P. Schaffarczyk, B. Lobo, F. Blondel, P. Gilbert, R. Boisart, L. Höning, L. Greco, C. Testa, E. Branlard, J. Jonkman, and G. Vijayakumar. Progress in validation of rotor aerodynamic codes using field data. *Wind Energy Science*, 8(2):211–230, 2023.

[33] A.J. Chorin. A numerical method for solving incompressible viscous flow problems. *Journal of Computational Physics*, 2(1):12–26, 1967.

[34] S.V. Patankar and D.B. Spalding. A calculation procedure for heat, mass and momentum transfer in three-dimensional parabolic flows. *International Journal of Heat and Mass Transfer*, 15(10):1787–1806, 1972.

[35] R.I. Issa. Solution of the implicitly discretised fluid flow equations by operator-splitting. *Journal of Computational Physics*, 62(1):40–65, 1986.

[36] S. B. Pope. *Turbulent flows.* Cambridge University Press, tenth edition, 2013.

[37] H.K. Versteeg and W. Malalasekera. *An Introduction to Computational Fluid Dynamics.* Pearson Education Unlimited, second edition, 2007.

[38] P. Spalart and S. Allmaras. A one-equation turbulence model for aerodynamic flows. In *30th Aerospace Sciences Meeting and Exhibit*, 1992.

[39] F. R. Menter. Two equation eddy-viscosity turbulence models for engineering applications. *AIAA Journal*, 32(8):1598–1605, 1994.

[40] F. Moukalled, L. Mangani, and M. Darwish. *The Finite Volume Method in Computational Fluid Dynamics*, volume 113. Springer, 2016.

[41] B. van Leer. Towards the ultimate conservative difference scheme. V. A second order sequel to Godunov's method. *Journal of Computational Physics*, 32(1):101–136, 1979.

[42] V. Venkatakrishnan. Convergence to steady state solutions of the euler equations on unstructured grids with limiters. *Journal of Computational Physics*, 118(1):120–130, 1995.

[43] G.D. van Albada, B. van Leer, and W.W.Roberts Jr. A comparative study of computational methods in cosmic gas dynamics. *Astronomy and Astrophysics*, 108:76–84, 1982.

[44] Y. Saad and M.H. Schultz. GMRES: A generalized minimal residual algorithm for solving nonsymmetric linear systems. *SIAM Journal on Scientific and Statistical Computing*, 7(3):856–869, 1986.

[45] H.A. van der Vorst. *Iterative Krylov methods for large linear systems.* Cambridge University Press, 2003.

[46] C.M. Rhie and W.L. Chow. Numerical study of the turbulent flow past an airfoil with trailing edge separation. *AIAA Journal*, 21(11):1525–1532, 1983.

[47] J. Donea, A. Huerta, J.-Ph. Ponthot, and A. Rodríguez-Ferran. Arbitrary Lagrangian-Eulerian methods. In *The Encyclopedia of Computation Mechanics.* John Wiley and Sons, 2004.

[48] C. Rumsey. NASA Turbulence Modeling Resource, 2023.

[49] H. Schlichting and K. Gersten. *Boundary-Layer Theory.* Springer-Verlag, ninth edition, 2017.

[50] D.M. Driver and H.L. Seegmiller. Features of reattaching turbulent shear layer in divergent channel flow. *American Institute of Aeronautics and Astronautics Journal*, 23(2):163–171, 1985.

[51] J. D. Anderson. *Fundamentals of Aerodynamics.* McGraw-Hill Education, New York, sixth edition, 2017.

[52] C.L. Ladson. Effects of independent variation of mach and reynolds numbers on the low-speed aerodynamic characteristics of the NACA0012 airfoil section. Technical Report NASA-TM-4074, NASA, 1988.

[53] J. G. Schepers and H. Snel. Model EXperiments in Controlled Conditions. Final report. Technical Report ECN-E–07-042, Energy research Centre of the Netherlands, 2007.

[54] K. Vimalakanthan and K. Boorsma. Baseline mexico rotor CFD simulations with SU2. Technical Report R11648, ECN, 2018.

[55] B. Sanderse. Aerodynamics of wind turbine wakes. Technical Report ECN-E–09-016, Energy Centre of the Netherlands, Wind Energy, 2009.

[56] C. Bak, U.S. Paulsen H.Aa Madsen, M. Gaunaa, P. Fuglsang, J. Romblad, N.A. Olesen, P. Enevoldsen, J. Laursen, and L. Jensen. DAN-AERO MW: Detailed aerodynamic measurements on a full scale MW wind turbine. In *EWEC 2010 Proceedings online*. European Wind Energy Association (EWEA), 2010.

Appendix A

Azimuthal velocity traverses - MEXICO rotor

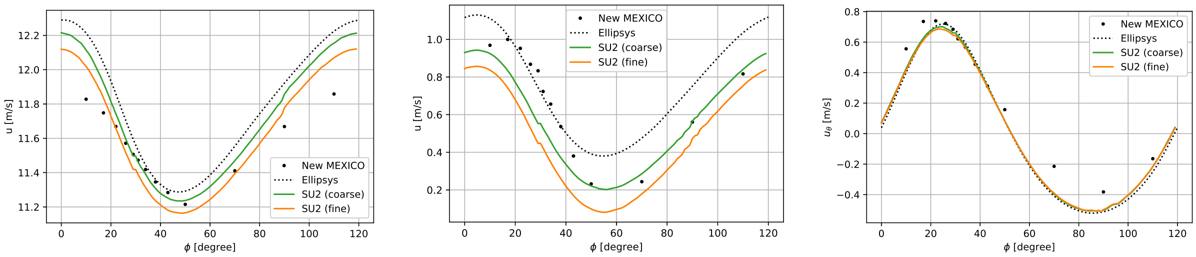

(a) Axial velocity component (b) Radial velocity component (c) Tangential velocity component

Figure A.1: Comparison azimuthal velocity trace at $x = -0.3\,\mathrm{m}$ and $r = 0.25\,\mathrm{m}$

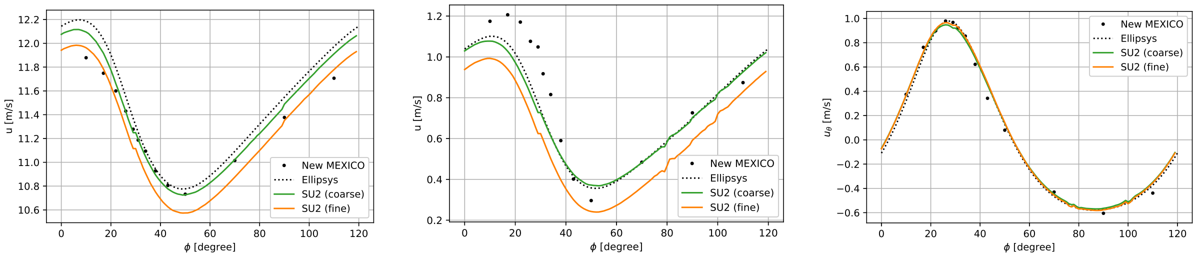

(a) Axial velocity component (b) Radial velocity component (c) Tangential velocity component

Figure A.2: Comparison azimuthal velocity trace at $x = -0.3\,\mathrm{m}$ and $r = 0.35\,\mathrm{m}$

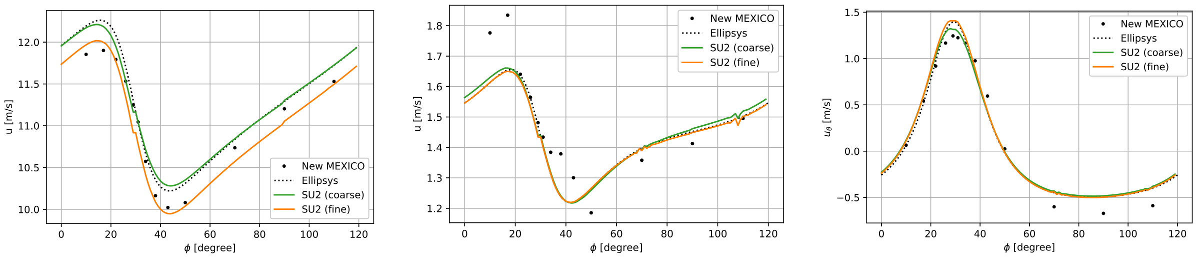

(a) Axial velocity component (b) Radial velocity component (c) Tangential velocity component

Figure A.3: Comparison azimuthal velocity trace at $x = -0.3\,\mathrm{m}$ and $r = 0.60\,\mathrm{m}$

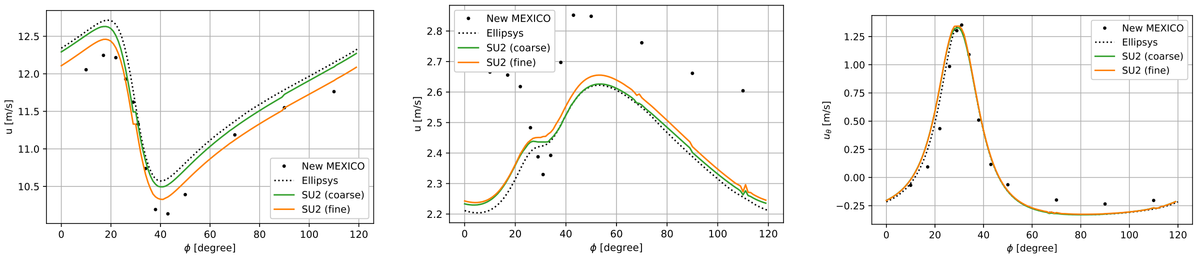

(a) Axial velocity component (b) Radial velocity component (c) Tangential velocity component

Figure A.4: Comparison azimuthal velocity trace at $x = -0.3\,\mathrm{m}$ and $r = 0.82\,\mathrm{m}$

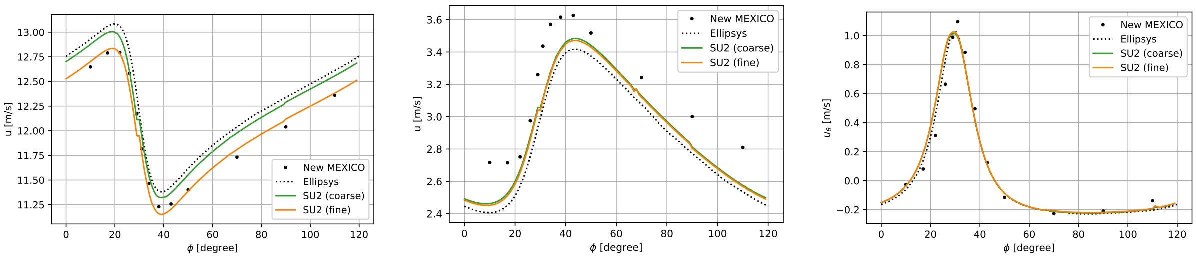

(a) Axial velocity component (b) Radial velocity component (c) Tangential velocity component

Figure A.5: Comparison azimuthal velocity trace at $x = -0.3\,\mathrm{m}$ and $r = 0.92\,\mathrm{m}$

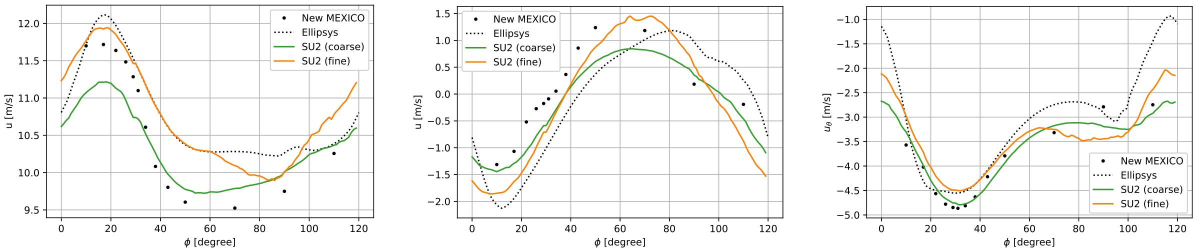

(a) Axial velocity component (b) Radial velocity component (c) Tangential velocity component

Figure A.6: Comparison azimuthal velocity trace at $x = 0.3\,\mathrm{m}$ and $r = 0.25\,\mathrm{m}$

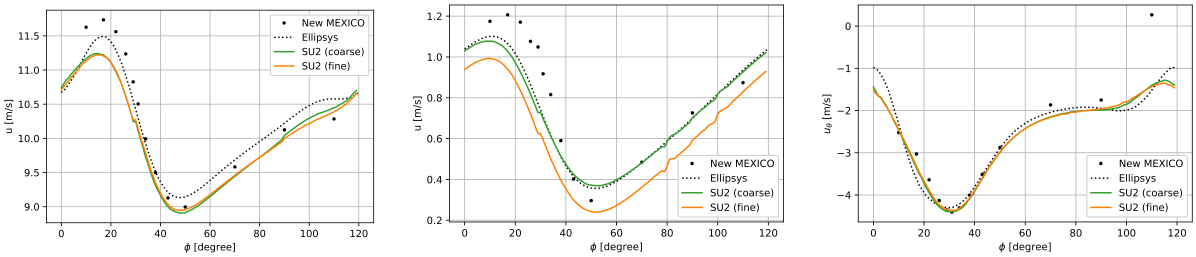

(a) Axial velocity component (b) Radial velocity component (c) Tangential velocity component

Figure A.7: Comparison azimuthal velocity trace at $x = 0.3\,\mathrm{m}$ and $r = 0.35\,\mathrm{m}$

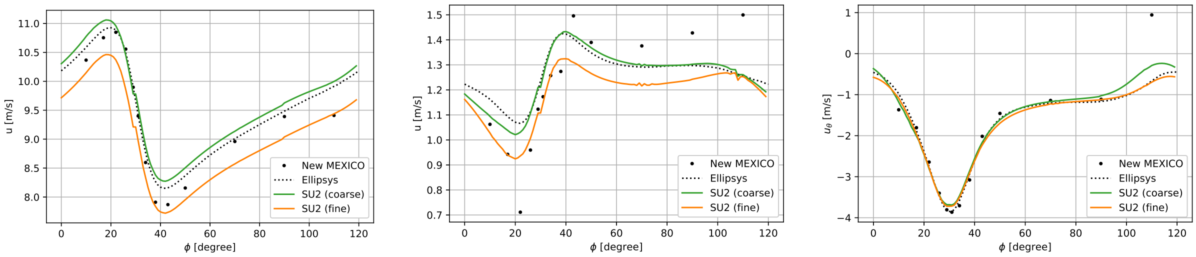

(a) Axial velocity component (b) Radial velocity component (c) Tangential velocity component

Figure A.8: Comparison azimuthal velocity trace at $x = 0.3\,\mathrm{m}$ and $r = 0.60\,\mathrm{m}$

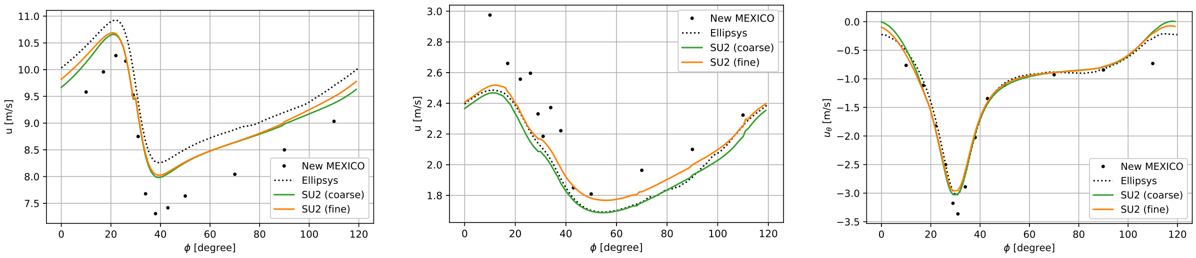

(a) Axial velocity component (b) Radial velocity component (c) Tangential velocity component

Figure A.9: Comparison azimuthal velocity trace at $x = 0.3\,\mathrm{m}$ and $r = 0.82\,\mathrm{m}$

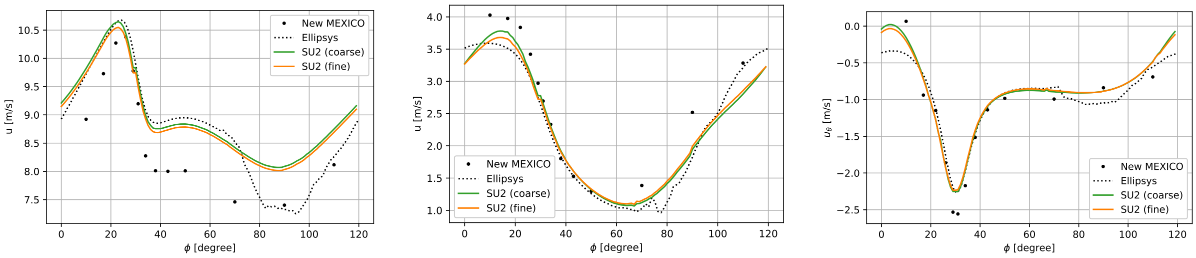

(a) Axial velocity component (b) Radial velocity component (c) Tangential velocity component

Figure A.10: Comparison azimuthal velocity trace at $x = 0.3\,\mathrm{m}$ and $r = 0.92\,\mathrm{m}$